INFLOW GENERATION TECHNIQUE FOR LARGE EDDY SIMULATION OF TURBULENT BOUNDARY LAYERS

By

Elaine Bohr

A Thesis Submitted to the Graduate

Faculty of Rensselaer Polytechnic Institute

in Partial Fulfillment of the

Requirements for the Degree of

DOCTOR OF PHILOSOPHY

Major Subject: Mechanical, Aerospace and Nuclear Engineering

Approved by the
Examining Committee:

____
Dr. Kenneth E. Jansen, Thesis Adviser

____
Dr. Mark S. Shephard, Member

____
Dr. Luciano Castillo, Member

____
Dr. Donald A. Drew, Member

____
Dr. Jean-François Remacle, Member

Rensselaer Polytechnic Institute
Troy, New York

April 2005
(For Graduation May 2005)

INFLOW GENERATION TECHNIQUE FOR LARGE EDDY SIMULATION OF TURBULENT BOUNDARY LAYERS

By

Elaine Bohr

An Abstract of a Thesis Submitted to the Graduate

Faculty of Rensselaer Polytechnic Institute

in Partial Fulfillment of the

Requirements for the Degree of

DOCTOR OF PHILOSOPHY

Major Subject: Mechanical, Aerospace and Nuclear Engineering

The original of the complete thesis is on file
in the Rensselaer Polytechnic Institute Library

Examining Committee:

Dr. Kenneth E. Jansen, Thesis Adviser

Dr. Mark S. Shephard, Member

Dr. Luciano Castillo, Member

Dr. Donald A. Drew, Member

Dr. Jean-François Remacle, Member

Rensselaer Polytechnic Institute
Troy, New York

April 2005
(For Graduation May 2005)

CONTENTS

LIST OF TABLES . . . v

LIST OF FIGURES . . . vi

ACKNOWLEDGEMENT . . . ix

ABSTRACT . . . x

1. INTRODUCTION AND LITERATURE REVIEW . . . 1
   - 1.1 Turbulent Inflow Generation Techniques . . . 2
   - 1.2 Influence of upstream conditions . . . 4
   - 1.3 Overview . . . 7

2. FINITE ELEMENT FORMULATION . . . 8
   - 2.1 Compressible flow formulation . . . 8
   - 2.2 Incompressible flow formulation . . . 12
   - 2.3 Large-Eddy simulation . . . 14
     - 2.3.1 Wall modeling . . . 16

3. SCALED PLANE EXTRACTION BOUNDARY CONDITION . . . 18
   - 3.1 General case . . . 18
     - 3.1.1 Incompressible, zero pressure gradient case . . . 18
     - 3.1.2 Rescaling recycling equations for velocity . . . 20
     - 3.1.3 Pressure and temperature . . . 24
   - 3.2 Lund, Wu and Squires Scaling Law . . . 26
   - 3.3 Alternative Scaling Laws for SPEBC . . . 27
     - 3.3.1 Similarity Analysis for the fluctuations . . . 29
       - 3.3.1.1 Inner layer . . . 33
       - 3.3.1.2 Outer layer . . . 35
     - 3.3.2 Scaling equations . . . 38

4. NUMERICAL IMPLEMENTATION OF SPEBC . . . 41
   - 4.1 Rescaling recycling algorithm . . . 41
   - 4.2 SPEBC for unstructured grids . . . 42
     - 4.2.1 Initialization . . . 43

4.2.2 Rescaling-recycling at each time step 44
4.2.3 Element search 45
4.3 Geometrical considerations for axisymmetrical problems 46
4.4 SPEBC for structured grids 48
4.5 Other considerations 49
4.5.1 Preprocessing for parallel simulations 49
4.5.2 Flow variables averaging in one homogeneous direction for the whole domain 50
4.5.2.1 Preprocessing the whole domain 51
4.5.2.2 Multiprocessor splitting 52
4.5.2.3 Mean flow quantities calculation at each time step . 54
4.5.3 Boundary layer thickness derivative calculation 54
5. RESULTS AND DISCUSSION 56
5.1 Laminar flat plate boundary layer flow 56
5.1.1 The SPEBC for Laminar Flows 57
5.1.2 Verification of the unstructured implementation of the SPEBC 59
5.2 Turbulent flat plate boundary layer flow 62
5.2.1 Boundary and initial conditions 62
5.2.1.1 Initiating the simulations 66
5.2.2 Solution with LWS scaling 67
5.2.2.1 Fluctuation scaling outside the boundary layer thickness 71
5.2.2.2 Mesh topology influence 73
5.2.2.3 Solution with alternative scaling 75
5.2.3 Comparing to experimental data 78
6. CONCLUSION 83
BIBLIOGRAPHY 85

LIST OF TABLES

3.1 Inlet temperature and pressure components computed from the recycle values 25

3.2 Partial derivatives for fluctuations similarity functions for inner layer . . 34

3.3 Partial derivatives for fluctuations similarity functions for outer layer . . 36

3.4 Scaling velocities for LWS scaling and for the scaling based on theory by GC 40

LIST OF FIGURES

3.1 Schematics of the flat plate boundary layer 20

3.2 Weighting function with $\alpha = 4$ and $b = 0.2$ 24

3.3 Fluctuation at $y^+ = 5$ (in inner region) and at a normal plane to the flow 31

3.4 Fluctuation at $y^+ = 120$ (in outer region) and at a normal plane to the flow 32

3.5 u' fluctuation at different y^+ planes and at a normal plane to the flow . 33

4.1 Sample mesh when using SPEBC for an axisymmetric problem 42

4.2 Schematic the axisymmetric domain used to implement axisymmetric SPEBC 46

4.3 Sample structured mesh 48

4.4 Partition mesh for a 5 processor case 49

4.5 Father nodes, sons and averaging lines 50

4.6 Eunuch nodes for each node of the mesh 51

4.7 Father nodes, sons and averaging lines on each processor 53

4.8 Eunuch nodes for each node of the mesh 53

5.1 Laminar flat plate mesh with inflow on left and the interface between the two colors showing the recycle plane. 56

5.2 Schematic of x-component velocity profiles for a laminar flat plate boundary layer 58

5.3 Dimensionless streamwise velocity profile inside the laminar flat plate boundary layer 59

5.4 Streamwise velocity profile for laminar flat plate boundary layer 60

5.5 Dimensionless streamwise velocity profile for laminar flat plate boundary layer as a function of dimensionless normal variable η computed by structured and unstructured simulations 61

5.6 Dimensionless streamwise velocity profile for laminar flat plate boundary layer as a function of dimensionless normal variable η computed by incompressible and compressible simulations 61

5.7 Dimensionless streamwise inflow velocity profile for laminar flat plate boundary layer as a function of dimensionless normal variable η computed by unstructured incompressible simulations for two recycle planes: $x_{rcy} = 0.2035m$ and $x_{rcy} = 0.203m$ 63

5.8 Dimensionless streamwise velocity profile for laminar flat plate boundary layer at $x = 0.2035m$ as a function of dimensionless normal variable η computed by unstructured incompressible simulations for two recycle planes: $x_{rcy} = 0.2035m$ and $x_{rcy} = 0.203m$ 63

5.9 Hexahedral mesh with $100 \times 45 \times 64$ points 64

5.10 Streamwise velocity initial condition using 1/7 power law and random fluctuations 65

5.11 Spalding profile fixed at the inlet for early transient 66

5.12 Temporal evolution of (a) Recycle plane's boundary layer thickness, and (b) Friction velocity at the inlet (upper) and recycle (lower) planes . . . 67

5.13 Streamwise velocity field 68

5.14 Streamwise velocity fluctuations at inlet and recycle planes 68

5.15 Mean streamwise velocity profiles at 10 different x locations in outer variables 69

5.16 Mean streamwise velocity profiles at 10 different x locations in inner variables 70

5.17 Reynolds stresses profiles at 10 different x locations 70

5.18 Normalized streamwise mean velocity with (red) and without (green) fluctuations rescaling in the free stream 72

5.19 Heaviside function 73

5.20 Boundary layer thickness (a) and friction velocity (b) as a function of streamwise location for the whole simulation domain for hexahedral (red curves) and tetrahedral (green curves) meshes 74

5.21 Mean streamwise flow profile obtained on hexahedral and tetrahedral meshes 74

5.22 Comparison of δ, H, u_τ and Re_θ versus Re_x between LWS and alternative scalings 75

5.23 Comparison of mean streamwise flow profile ($\frac{U}{U_\infty}$ vs. η) obtained using LWS and alternative scalings at $Re_\theta = 1800$ and 1900 76

5.24 Comparison of mean streamwise flow profile ($\frac{U_\infty - U}{u_\tau}$ vs. η) obtained using LWS and alternative scalings at $Re_\theta = 1800$ and 1900 76

5.25 Comparison of mean streamwise flow profile in semi log scale (u^+ vs. y^+) obtained using LWS and alternative scalings at $Re_\theta = 1800$ and 1900 77

5.26 Comparison of Reynold stresses obtained using LWS and alternative scalings at $Re_\theta = 1800$ and 1900 77

5.27 Comparing velocity profile in outer variables obtained using LWS and alternative scalings at $Re_\theta = 1900$ to experimental data by Castillo and Johansson [9] at $Re_\theta = 1919$ and 2214, of Smits and Smith [50, 51] at $Re_\theta = 4981$ and of Purtell, Klebanoff and Buckley [44] at $Re_\theta = 1840$. 79

5.28 Comparing velocity profile in inner variables obtained using LWS and alternative scalings at $Re_\theta = 1900$ to experimental data by Castillo and Johansson [9] at $Re_\theta = 1919$ and 2214 and of Smits and Smith [50, 51] at $Re_\theta = 4981$ 80

5.29 Comparing Reynolds stresses profiles obtained using LWS and alternative scalings at $Re_\theta = 1900$ to experimental data by Castillo and Johansson [9] at $Re_\theta = 1919$ and 2214 and of Smits and Smith [50, 51] at $Re_\theta = 4981$ 81

5.30 Comparing velocity profiles from LWS scaling at $Re_\theta = 1900$ and DNS data by Adrian and Tomkins [1, 2] at $Re_\theta = 1015$ 81

ACKNOWLEDGEMENT

I would like to thank, first of all, my advisor, Prof. Jansen for the support he gave me throughout my stay here at RPI. His knowledge of all the different aspects of computational fluid dynamics was a big help to my understanding of the field. His classes on finite element method, CFD and turbulence modeling were the stepping stones for this research and I thank him for the quality of those classes. I was impressed by the availability that prof. Jansen has for all his students. Without it this work would be much more difficult. I also want to thank prof. Jansen for his friendship.

I want to acknowledge the help that I got form Prof. Castillo for developing the alternative scaling. Prof. Shepard, thank you for the finite element class which introduced me to the field of FEM. I am thankful to have Prof. Drew on my committee. And Jean-Francois Remacle, thank you for your help during my graduate years here and in Montreal.

I want to mention all the current members of our research group: Jens, Azat, Michael, Victor, Alisa and past members: Sunitha, Anil, Andres. Thank you all for your help on understanding PHASTA and all the necessary tools. Thank you also for being there whenever I needed it. I also must mention all the SCOREC people without whom this experience would not be the same, to name just a few: Luo, Eunyoung, Andy, Marge.

Finally I need to thank my husband, Christophe Dupré, first for the technical help that I got form him throughout this period as the SCOREC system administrator, and foremost for his unconditional support in all my undertakings and for awesome husband and father he is. I must mention my two darlings: Arthur and Gabriel without whom this experience would have been much quicker and easier, but not as much fun as it was.

ABSTRACT

When simulating turbulent flows using Large-Eddy Simulations (LES) or Direct Numerical Simulations (DNS), imposing correct instantaneous flow quantities at the inflow boundary is a challenge. Indeed, inflow fluctuations need to preserve the turbulent characteristics of the upstream flow that is not simulated. In this thesis, the rescaling recycling method for imposing boundary conditions at the inflow of turbulent boundary layer simulations is developed. The inflow conditions are rendered more physically meaningful by rescaling the instantaneous solution from an internal plane normal to the wall located inside the computational domain using self-similarity of the boundary layer velocity profile at each time step of the simulation. Thus the fluctuations at the inflow incorporate correct turbulent structures. This operation enables a reduction of the needed computational domain.

In addition, the rescaling recycling method was implemented in a finite element software using unstructured meshes to expand its application to curved domains (pipes, contracting or expanding nozzles). The important issue when using unstructured meshes is that the recycle plane from which the solution is rescaled is virtual and as such the solution must first be interpolated on that plane before the method can be applied.

In this thesis, the LES solutions are presented for zero pressure gradient flat plate turbulent boundary layer using two different scaling laws. First the scaling law developed by Lund, Wu and Squires (LWS) is used. An alternative scaling is also developed based on the theory by George and Castillo that incorporates the local Reynolds number dependence. It was found that the alternative scaling gives statistically similar flow profiles to those obtained by the LWS scaling, but the Reynolds number based on momentum thickness was 3% higher. The numerical results were found to be in good agreement with experimental data.

CHAPTER 1
INTRODUCTION AND LITERATURE REVIEW

Turbulence is still one of few unsolved problems in fluid dynamics. Better understanding of this field would benefit manufacturing and other industries, like the automotive and aeronautic industries. Not only physical and mathematical characterization of turbulence is needed, but also its numerical simulation needs to be improved.

Finite Element Methods (FEM) are frequently used in Computational Fluid Dynamics (CFD) to study unsteady and turbulent flows. The simulations of fluid dynamics problems are usually computationally expensive due to the large number of mesh elements since three dimensional calculations are often necessary. Consequently, it is of interest to consider if simplifications and assumptions on the studied flow can produce acceptable results for the finite amount of computational resources at hand.

The most common numerical simulation techniques for CFD are Reynolds-Averaged Navier-Stokes Simulation (RANSS), Direct Numerical Simulation (DNS) and Large-Eddy Simulation (LES). In RANSS the simulation of the mean quantities are calculated and the Reynolds stresses are modeled in terms of various statistical fields (turbulent kinetic energy, dissipation, Reynolds stresses) using different models ($k - \epsilon$ [31], mixing-length, Spalart and Allmaras [52] to name just a few [66]). RANS simulations are computationally relatively inexpensive and widely used over a broad range of Reynolds numbers and complex flows. In RANS simulations only mean quantities need to be imposed at the inflow boundary, but, since so much of the turbulence is "built in" to the model, solutions are only as good as the model used. DNS simulations resolve Navier-Stokes equations on the whole domain directly. The solution obtained by this method is the most accurate, but as all the different turbulent scales are computed, the mesh of the domain must be very fine so that even the smallest scales can be resolved. This method is computationally the most expensive and can only be applied to small, relatively simple domains and it is limited to very low Reynolds numbers. LES was developed to bridge the gap between RANS simulations and DNS. LES is a computation in which the large eddies are computed and the smallest, called subgrid-scale (SGS), eddies are modeled using the Smagorinsky eddy viscosity [49] or the dynamic SGS model [20, 36, 60].

For both DNS and LES computations, the mean boundary conditions need to be complemented by also imposing fluctuations of the computed quantities. Mean quantities can be computed by a RANS simulation (subject to their incumbent modeling error), but imposing physical fluctuations as boundary conditions is a problem in itself. This research focuses on the method of imposing physically meaningful fluctuation boundary conditions at the inlet of a boundary layer simulation.

1.1 Turbulent Inflow Generation Techniques

Different techniques are presented in literature that were used to impose fluctuations on boundaries of simulation domains. As fluctuations are instantaneous quantities, they cannot be approximated by simple equations. Thus when imposing them on the inlet boundary the variation in time must be included, but keeping their time average null.

One way to impose the fluctuations is to extract them from experimental data. Druault *et al.* [13] generate the three-dimensional turbulent inlet conditions through an interface that extracts turbulence information from an experiment using proper orthogonal decomposition and reconstructs the needed time-varying quantities at the inlet mesh grid points.

Another way is the use of hybrid methods that attempt to combine RANSS and LES into one simulation by modifying the RANS Reynolds-stress tensor to incorporate subgrid eddy viscosity solely based on mesh element size to distinguish the RANSS region from the LES [4].

In nature laminar flow will go through a transition region before becoming turbulent. This idea can also be used when simulating a spatially-developing turbulent boundary. By starting far upstream using laminar flow with some disturbances, natural transition to turbulence can occur. This approach was used for simulation of the transition process [45] and has the advantage that no turbulent fluctuations are needed at the inlet. This procedure is not applicable for many turbulent flow simulations because simulating the transition is already costly and coupling it with downstream simulation of turbulence becomes prohibitively expensive.

Instead of simulating the entire transition region, most often the inflow boundary is displaced upstream by a short distance where random fluctuations are superposed over a desired mean velocity profile. The amplitude of the random fluctuations can be constrained to satisfy Reynolds stress tensor. As no information exists for the phase, a lengthy development section is still needed. This method is still widely used to simulate turbulent inflow data. Lee *et al.* [35] used it for direct numerical simulation (DNS) of compressible isotropic turbulence, Rai and Moin [45] for producing isotropic free-stream disturbances in DNS of laminar to turbulent transition of a boundary layer and Le *et al.* [34] extended it to generate anisotropic turbulence for DNS of a backward facing step. A developing section of as much as 20 boundary layer thicknesses was needed to recover the correct skin friction. However, much better results are obtained by using a separate simulation for the inflow generation which is incorporated to the main simulation once the inflow data becomes stationary.

In the work of Lund [38] and Lund and Moin [39] a fully developed boundary layer-like mean profile is obtained using periodic boundary conditions in the streamwise and spanwise direction and vanishing vertical velocity and derivatives in spanwise and streamwise directions at the upper domain boundary to generate the inflow condition for LES of a boundary layer on a concave wall. A development section was still needed because the obtained inflow boundary layer had no mean advection. Spalart [53] developed a method to account for spatial growth in simulations with periodic boundary conditions by adding a source terms to the Navier-Stokes equations [54] arising from a coordinate transformation that minimizes the streamwise inhomogeneity. Lund, Wu and Squires [40] modified the Spalart method [54] by simplifying the approach: only the boundary conditions are transformed as opposed to the entire solution domain.

In section 3.2 the scaling used in Lund, Wu and Squires (LWS) [40] method is explained as it is the scaling most widely used in literature when extracting mean and fluctuations from the interior for application at the inflow and it will be the foundation of the present work. Stolz and Adams [56] use LWS scaling for LES of supersonic boundary layers. In the paper by Segaut *et al.* [47] it is one of several scalings which were used for LES of compressible wall-bounded flows. Kong *et al.* [33] expanded the LWS scaling for temperature when doing a DNS of turbulent thermal boundary layers. In some of these cases two simulations were performed. The first simulation, or pre-simulation, rescales and recycles the flow solution from some plane inside the domain using the LWS method to obtain meaningful turbulent fluctuations at the inflow of the second, main simulation. Once the flow from the first simulation becomes statistically stationary, the solution for the mean flow components and their fluctuations is extracted from the appropriate location and used as the boundary condition on the inlet plane of the second simulation of the studied flow. In these cases it is assumed that the turbulence achieved in the first simulation which contains information about the flow upstream of the simulation domain is the same in the main simulation. In other words, it is assumed that the same upstream conditions are present in both simulations. This assumption is violated when the main simulation has a non zero pressure gradient because the pre-simulation is a simulation of the turbulent boundary layer with zero pressure gradient.

This method of imposing boundary conditions on mean and fluctuating quantities at the inlet plane by extracting the turbulence information from a downstream location will be called rescaling recycling method. In the present research, the rescaling recycling method is implemented without the need of a separate fluctuation generation simulation. Indeed, the inflow data is generated concurrently with the ongoing simulation by sampling the boundary layer at some distance downstream of the flow. At each simulation's time step, this method is used to update the flow solution at the inflow boundary after the Navier-Stokes equations (filtered for LES or not for DNS) were solved inside the domain for the current time step.

1.2 Influence of upstream conditions

LWS scaling was based on single point turbulence models of boundary layers. Single point turbulence assumes that the turbulence is dynamically similar everywhere in the flow if nondimensionalized with local length and time scales. This is called self-preservation of turbulent flows [62]. It is supposed that turbulent flows do not have memory of their origins. The traditional view in the turbulence community is that flows achieve a self-preserving state by becoming asymptotically independent of their initial conditions as described by Townsend in [63]. Upstream conditions influence how the flow is started, but in the far-field, the single point turbulence assumes that the flow is independent of them. So turbulence can be modeled by its local properties.

But over the past three decades the experimental evidence implies that this view of turbulence is oversimplified. There is a wide scatter in experimental results found in literature $\sim \pm 30\%$ [37, 21, 12, 42, 46, 41] that is too large to attribute solely to measurement errors and difference in experimental techniques. So experiments seem not to validate the traditional view where everything collapses together even with different upstream conditions.

Turbulence cannot be scaled by a single length scale. Batchelor [3] argued that high Reynolds number turbulent flows require at least separate scales for energy-containing eddies and for the dissipative scales. Wygnanski *et al.* [67] show that growth of wakes arising from different source conditions are also different because drag sources have finite dimensions. Similarly the source of momentum of real jets have finite dimensions, and also finite rate of mass and energy, so it is difficult to model them as a point source of momentum. Experimentally it was shown that growth of jets arising from different source conditions are also different [22].

Traditionally it was thought that all shear flows of a given class, i.e. boundary layers, wakes, jets, collapse to the same flow profile regardless of their upstream conditions. Lately the research done tends to show that this is not true, but that even if flow profiles still collapse they will collapse to different curves depending on their starting conditions. For example, in [41] the solution of passive scalar for axisymmetric jets was studied by comparing their experimental results to experiments from literature obtained for round jet with different nozzle types. By self-preservation this quantity is independent of the distance in the far-field and asymptotes to horizontal lines. For true self-preservation all experimental results would collapse to the same line as they are all round jets, but this is not the case. Instead, results from same experiments collapse together and each experimental result asymptotes to different horizontal line. This implies that upstream conditions determine to which line the solution will collapse.

The divergence between the theory of self-preservation and experimental results inspired George [16] to develop the self-similarity concept where upstream conditions continue to influence the shear flows even in the far-field. The flows are classified into three categories:

Fully self-preserving flows where self-preservation is present at all orders of the turbulence momentum and Reynolds stress equations and at all scales of motion.

Partially self-preserving flows where the self-preservation is at the level of mean momentum equations only (or up to certain order of scales)

Locally self-preserving flows where the profiles scale with local quantities, but equations of motion do not admit to self-preserving solutions.

This classification leads to two conjectures hypothesized by George [16]. If the equations of motion, boundary and initial conditions governing the flow admit to self-preserving solutions, then the flow will always asymptotically behave in this manner. And if they do not admit to fully self-preserving solutions, the flow will adjust itself as closely as possible to a state of full self-preservation. The second conjecture includes partial and local self-preservation states.

In a subsequent paper [17] the Asymptotic Invariance Principle (AIP) was developed to reconsider the theoretical foundations of the law of the wall and the velocity deficit law of the classical theory as only the law of the wall is derivable using AIP theory. AIP arrives to an alternate velocity deficit equation where the velocity deficit is scaled with U_∞ instead of u_τ [15, 18, 19].

In this work, an alternate scaling equations are proposed in section 3.3. This scaling is based on AIP theory which incorporates the local Reynolds number dependence.

1.3 Overview

The rescaling recycling method is developed to complement the Large-Eddy Simulation software that will be called Parallel Hierarchic Adaptive Stabilized Transient Analysis (PHASTA). PHASTA uses the Streamline Upwind Petrov-Galerkin (SUPG) finite element method. In chapter 2 first the compressible and incompressible finite element equations are presented in sections 2.1 and 2.2 respectively. Section 2.3 explains briefly LES equations that are used in PHASTA.

Chapter 3 focuses on the theory of the rescaling recycling boundary condition. In section 3.1, a general framework is developed to describe the rescaling recycling equations with no specific scaling laws. Next two specific scaling laws are presented: LWS scaling in section 3.2 and the alternate scaling in section 3.3. In this manner, if new scalings are developed, they can easily be incorporated and implemented.

The specific implementation of the rescaling recycling method presented in chapter 4 will be called the Scaled Plane Extraction Boundary Condition or SPEBC for short. First, we explain how the flow solution is rescaled and extracted from downstream to be used as the boundary condition on the inflow in sections 4.1 and 4.2. Then some considerations for axisymmetric implementation are discussed in section 4.3 and the specific case if structured 2D meshes exist at both inlet and recycle planes is explained in section 4.4. Finally other implementational considerations are discussed in section 4.5. Those are parallel implementation (4.5.1), homogeneous averaging in unstructured meshes (4.5.2) and calculation of boundary layer thickness derivatives (4.5.3) needed for the alternative scaling presented in 3.3.

The implementation is validated by the simulation of the laminar flat plate boundary layer in the first section of chapter 5. This chapter also presents results for turbulent flat plate boundary layers simulations using both LWS scaling and the alternate scaling. The zero pressure gradient turbulent flat plate boundary layer solution is compared to experimental data of Castillo and Johansson [9], Smits and Smith [50, 51] and Purtell, Klebanoff and Buckley [44], as well as some DNS results by Adrian and Tomkins [1, 2]. Finally future work is discussed in chapter 6.

CHAPTER 2
FINITE ELEMENT FORMULATION

In this chapter the finite element formulation will be described. As the recycling-rescaling boundary condition can be used for both compressible and incompressible cases the finite element formulation for both cases will be shown.

2.1 Compressible flow formulation

Starting from the compressible Navier-Stokes equations written in conservative form (see Jansen [29, 27] for details):

- Continuity equation:

$$\rho_{,t} + [\rho u_i]_{,i} = 0 \tag{2.1}$$

- Momentum equations:

$$[\rho u_i]_{,t} + [\rho u_i u_j]_{,j} + p_{,i} = \tau_{ij,j} + b_i \tag{2.2}$$

- Energy equation:

$$[\rho e_{tot}]_{,t} + [\rho u_i e_{tot}]_{,i} + [u_i p]_{,i} = [\tau_{ij} u_j]_{,i} + b_j u_j + r \tag{2.3}$$

These equations (2.1 - 2.3) can be written in compact form as follows:

$$\boldsymbol{U}_{,t} + \boldsymbol{F}_{i,i} = \boldsymbol{\mathcal{F}} \tag{2.4}$$

where

$$\boldsymbol{U} = \{U_i\} = \rho \left\{ \begin{array}{c} 1 \\ u_i \\ e_{tot} \end{array} \right\}, \qquad \boldsymbol{F}_i = \underbrace{u_i \boldsymbol{U} + p \left\{ \begin{array}{c} 0 \\ \delta_{ij} \\ u_i \end{array} \right\}}_{\boldsymbol{F}_i^{\text{adv}}} + \underbrace{\left\{ \begin{array}{c} 0 \\ -\tau_{ij} \\ -\tau_{ik}\, u_k + q_i \end{array} \right\}}_{\boldsymbol{F}_i^{\text{diff}}} \tag{2.5}$$

and

$$\tau_{ij} = 2\mu(S_{ij}(\boldsymbol{u}) - \frac{1}{3}S_{kk}(\boldsymbol{u})\delta_{ij}), \qquad S_{ij}(\boldsymbol{u}) = \frac{u_{i,j} + u_{j,i}}{2} \tag{2.6}$$

$$q_i = -\kappa T_{,i}, \qquad e_{\text{tot}} = e + \frac{u_i u_i}{2}, \qquad e = c_v T \tag{2.7}$$

In these equations the variables are: the velocity u_i, the density ρ, the pressure p, the temperature T and the total energy e_{tot}. Finally $\boldsymbol{\mathcal{F}}$ is a body force (or source) vector:

$$\boldsymbol{\mathcal{F}} = \left\{ \begin{array}{c} 0 \\ b_i \\ b_k u_k + r \end{array} \right\} \tag{2.8}$$

$\boldsymbol{U}$ is the vector of conservative variables, as discussed in Hauke and Hughes [24], it is often not the best choice of solution variables, particularly when the flow is nearly incompressible. Instead the pressure-primitive variables (the pressure p, the velocity u_i and the temperature T) are used:

$$\boldsymbol{Y} = \left\{ \begin{array}{c} Y_1 \\ Y_2 \\ Y_3 \\ Y_4 \\ Y_5 \end{array} \right\} = \left\{ \begin{array}{c} p \\ u_1 \\ u_2 \\ u_3 \\ T \end{array} \right\} \tag{2.9}$$

For the specification of the methods that follow, it is helpful to define the quasi-linear operator as

$$\boldsymbol{\mathcal{L}} \equiv \boldsymbol{A}_0 \frac{\partial}{\partial t} + \boldsymbol{A}_i \frac{\partial}{\partial x_i} - \frac{\partial}{\partial x_i}(\boldsymbol{K}_{ij} \frac{\partial}{\partial x_j}) \tag{2.10}$$

Here $\boldsymbol{A}_0 = \boldsymbol{U}_{,\boldsymbol{Y}}$ is the change of variables metric, $\boldsymbol{A}_i = \boldsymbol{F}^{\text{adv}}_{i,\boldsymbol{Y}}$ is the i^{th} Euler Jacobian matrix, and $\boldsymbol{K}_{ij}$ is the diffusivity matrix, defined such that $-\boldsymbol{K}_{ij}\boldsymbol{Y}_{,j} = \boldsymbol{F}^{\text{diff}}_i$. For a complete description of $\boldsymbol{A}_0$,$\boldsymbol{A}_i$ and $\boldsymbol{K}_{ij}$, the reader is referred to [23, 25]. Using this, the equation (2.4) can be written simply as $\boldsymbol{\mathcal{L}}\boldsymbol{Y} = \boldsymbol{\mathcal{F}}$.

To proceed with the finite element discretization of the Navier-Stokes equations (2.4), the finite element approximation spaces must be defined. First, let $\bar{\Omega} \subset$

$\mathbf{R}^3$ represent the closure of the physical spatial domain (i.e. $\Omega \cup \Gamma$ where Γ is the boundary). The boundary is decomposed into portions with natural boundary conditions, Γ_h, and essential boundary conditions, Γ_g, i.e., $\Gamma = \Gamma_g \cup \Gamma_h$. In addition, $H^1(\Omega)$ represents the usual Sobolev space of functions with square-integrable values and derivatives on Ω.

Next, Ω is discretized into n_{el} finite elements, Ω^e. With this, the trial solution space for the semi-discrete formulations is

$$\boldsymbol{\mathcal{V}}_h = \{\boldsymbol{Y} | \boldsymbol{Y}(\cdot, t) \in H^1(\Omega)^m, t \in [0, T], \boldsymbol{Y}|_{x\in\Omega^e} \in P_k(\Omega^e)^m, \boldsymbol{Y}(\cdot, t) = \boldsymbol{g} \text{ on } \Gamma_g\}, \tag{2.11}$$

and the weight function space is

$$\boldsymbol{\mathcal{W}}_h = \{\boldsymbol{W} | \boldsymbol{W}(\cdot, t) \in H^1(\Omega)^m, t \in [0, T], \boldsymbol{W}|_{x\in\Omega^e} \in P_k(\Omega^e)^m, \boldsymbol{W}(\cdot, t) = \mathbf{0} \text{ on } \Gamma_g\}, \tag{2.12}$$

where $P_k(\Omega^e)$, is the space of all polynomials defined on Ω^e, complete to order $k \geq 1$, and m is the number of degrees of freedom ($m = 5$).

To derive the weak form of equation (2.4), the entire equation is dotted with a vector of weight functions, $\boldsymbol{W} \in \boldsymbol{\mathcal{W}}_h$, and integrated over the spatial domain. Integration by parts is then performed on the integral with $\boldsymbol{F}_i$ to move the spatial derivatives onto the weight functions. This process leads to the following problem:

- Find $\boldsymbol{Y} \in \boldsymbol{\mathcal{V}}_h$ such that

$$\begin{aligned} 0 &= \int_\Omega \left(\boldsymbol{W} \cdot \boldsymbol{A}_0 \boldsymbol{Y}_{,t} - \boldsymbol{W}_{,i} \cdot \boldsymbol{F}_i - \boldsymbol{W} \cdot \boldsymbol{\mathcal{F}}\right) d\Omega + \int_\Gamma \boldsymbol{W} \cdot \boldsymbol{F}_i \, n_i \, d\Gamma \\ &+ \sum_{e=1}^{n_{el}} \int_{\Omega^e} \hat{\boldsymbol{\mathcal{L}}}^T \boldsymbol{W} \cdot \boldsymbol{\tau} \left(\boldsymbol{\mathcal{L}} \boldsymbol{Y} - \boldsymbol{\mathcal{F}}\right) d\Omega \end{aligned} \tag{2.13}$$

This integral equation is known as the weak form. The first line of equation (2.13) contains the Galerkin approximation (interior and boundary) and the second line contains the SUPG (Streamline Upwind Petrov Galerkin, see [6] for details) stabilization:

$$\hat{\boldsymbol{\mathcal{L}}} \equiv \boldsymbol{A}_i \frac{\partial}{\partial x_i} \tag{2.14}$$

The stabilization matrix $\boldsymbol{\tau}$ is an important parameter in these methods and is well documented in Shakib [48] and in Franca and Frey [14].

To develop a numerical method, the weight functions ($\boldsymbol{W}$), the solution variable ($\boldsymbol{Y}$), and it's time derivative ($\boldsymbol{Y}_{,t}$) are expanded in terms of basis functions (typically piecewise polynomials). On element level this is:

$$\boldsymbol{W} = \sum_{b=1}^{n_{en}} N_b(\boldsymbol{\xi})\, \boldsymbol{W}_b^e \tag{2.15}$$

$$\boldsymbol{Y} = \sum_{a=1}^{n_{en}} N_a(\boldsymbol{\xi})\, \boldsymbol{Y}_a^e \tag{2.16}$$

$$\boldsymbol{Y}_{,t} = \sum_{a=1}^{n_{en}} N_a(\boldsymbol{\xi})\, \boldsymbol{Y}_{a,t}^e \tag{2.17}$$

$$\boldsymbol{Y}_{,i} = \sum_{a=1}^{n_{en}} N_{a,i}(\boldsymbol{\xi})\, \boldsymbol{Y}_a^e \tag{2.18}$$

where n_{en} is the number of element nodes and $\boldsymbol{\xi}$ is the local coordinate system. With some manipulations and inserting equations (2.15 - 2.18) into equation (2.13), and by noting that $\boldsymbol{W}_b^e$ are arbitrary, equation (2.13) becomes:

$$0 = \boldsymbol{G}_B(\boldsymbol{Y}, \boldsymbol{Y}_{,t}) = \bigwedge_{e=1}^{n_{el}} \boldsymbol{G}_b^e(\boldsymbol{Y}, \boldsymbol{Y}_{,t}) \tag{2.19}$$

where

$$\begin{aligned}\boldsymbol{G}_b^e &= \int_{\square} \left[N_b \left\{\boldsymbol{A}_0 \boldsymbol{Y}_{,t} - \boldsymbol{\mathcal{F}}\right\} - N_{b,i} \boldsymbol{F}_i\right] \boldsymbol{D} d\square \\ &+ \int_{\square} \hat{\boldsymbol{\mathcal{L}}} N_b \boldsymbol{\tau} \left\{\boldsymbol{\mathcal{L}} \boldsymbol{Y} - \boldsymbol{\mathcal{F}}\right\} \boldsymbol{D} d\square + \int_{\square_\Gamma} N_b \boldsymbol{F}_i \boldsymbol{n}_i \boldsymbol{D}_\Gamma d\square_\Gamma\end{aligned} \tag{2.20}$$

The integrals of equation (2.20) are then evaluated using Gauss quadrature resulting in a system of non-linear ordinary differential equations. Finally this system is discretized in time via a generalized-α time integrator (see [28]) resulting in a nonlinear system of algebraic equations. This system is in turn linearized with Newton's method which yields a linear algebraic system of equations to be solved at each

Newton iteration.

$$\underbrace{\boldsymbol{G}_A\left(\overset{n+\alpha_m}{\boldsymbol{Y}^{(i)}_{,t}}, \overset{n+\alpha_f}{\boldsymbol{Y}^{(i)}}\right)}_{\boldsymbol{R}_A} + \underbrace{\sum_{B=1}^{n_{np}} \frac{\partial \boldsymbol{G}_A}{\partial \overset{n+\alpha_f}{\boldsymbol{Y}^{(i)}_B}} \left(\overset{n+\alpha_m}{\boldsymbol{Y}^{(i)}_{,t}}, \overset{n+\alpha_f}{\boldsymbol{Y}^{(i)}}\right)}_{\boldsymbol{M}_{AB}} \Delta \overset{n+\alpha_f}{\boldsymbol{Y}^{(i)}_B} = 0 \tag{2.21}$$

In this equation α_f and α_m are parameters of the generalized-α method. Newton iterations continue until the non-linear residual is satisfied at each time step, after which the method proceeds to the next time step, starting the process over again.

2.2 Incompressible flow formulation

The unsteady incompressible Navier-Stokes equations are:

- Continuity:

$$u_{i,i} = 0 \tag{2.22}$$

- Momentum:

$$\rho(\dot{u}_i + u_j u_{i,j}) = -p_{,i} + \tau_{ij,j} + f_i \tag{2.23}$$

where the stress tensor, τ_{ij}, is the symmetric strain rate tensor as the divergence of the flow is zero (eq. 2.22) multiplied by the viscosity:

$$\tau_{ij} = \mu(u_{i,j} + u_{j,i}) \tag{2.24}$$

To discretize these equations for use in the finite element formulation, the physical spatial domain is represented as in the compressible case. The discrete trial solution and weight spaces for the semi-discrete formulation of the incompressible Navier-

Stokes equations are:

$$\boldsymbol{\mathcal{S}}_h^k = \{\boldsymbol{v} | \boldsymbol{v}(\cdot,t) \in H^1(\Omega)^N, t \in [0,T], \boldsymbol{v}|_{x\in\bar{\Omega}_e} \in P_k(\bar{\Omega}_e)^N, \boldsymbol{v}(\cdot,t) = \boldsymbol{g} \text{ on } \Gamma_g\}, \quad (2.25)$$

$$\boldsymbol{\mathcal{W}}_h^k = \{\boldsymbol{w} | \boldsymbol{w}(\cdot,t) \in H^1(\Omega)^N, t \in [0,T], \boldsymbol{w}|_{x\in\bar{\Omega}_e} \in P_k(\bar{\Omega}_e)^N, \boldsymbol{w}(\cdot,t) = \boldsymbol{0} \text{ on } \Gamma_g\}, \quad (2.26)$$

$$\mathcal{P}_h^k = \{p | p(\cdot,t) \in H^1(\Omega), t \in [0,T], p|_{x\in\bar{\Omega}_e} \in P_k(\bar{\Omega}_e)\} \quad (2.27)$$

where $P_k(\bar{\Omega}_e)$ is the space of all polynomials defined on Ω^e, complete to order $k \geq 1$. The local approximation space, $P_k(\bar{\Omega}_e)$, is same for both the velocity and pressure variables due to the stabilized nature of the formulation. These spaces represent discrete subspaces of the spaces in which the weak form is defined.

The stabilized formulation used in the present work is based on the formulation described by Taylor *et al.* [58]. Given the spaces defined above, the semi-discrete stabilized Galerkin finite element formulation applied to the weak form of (2.23) is:

Find $\boldsymbol{u} \in \boldsymbol{\mathcal{S}}_h^k$ and $p \in \mathcal{P}_h^k$ such that

$$\begin{aligned}
&\int_\Omega \{w_i (\dot{u}_i + u_j u_{i,j} - f_i) + w_{i,j}(-p\delta_{ij} + \tau_{ij}) - q_{,i} u_i\} dx \\
&\quad + \int_{\Gamma_h} \{w_i (p\delta_{in} - \tau_{in}) + q u_n\} ds \\
&+ \sum_{e=1}^{n_{el}} \int_{\bar{\Omega}_e} \{\tau_M (u_j w_{i,j} + q_{,i}) \mathcal{L}_i + \tau_C w_{i,i} u_{j,j}\} dx \\
&+ \sum_{e=1}^{n_{el}} \int_{\bar{\Omega}_e} \{w_i \overset{\Delta}{u}_j u_{i,j} + \bar{\tau} \overset{\Delta}{u}_j w_{i,j} \overset{\Delta}{u}_k u_{i,k}\} dx = 0
\end{aligned} \quad (2.28)$$

for all $\boldsymbol{w} \in \boldsymbol{\mathcal{W}}_h^k$ and $q \in \mathcal{P}_h^k$. The boundary integral term arises from the integration by parts and is only carried out over the portion of the domain with natural boundary conditions. For simplicity, $\mathcal{L}_i$ is used to represent the residual of the i^{th} momentum equation,

$$\mathcal{L}_i = \dot{u}_i + u_j u_{i,j} + p_{,i} - \tau_{ij,j} - f_i \quad (2.29)$$

The third line in the stabilized formulation, (2.28), represents the typical stabilization added to the Galerkin formulation for the incompressible set of equations (e.g. Franca and Frey [14]). The description of the individual terms and the stabilization parameters for continuity and momentum are discussed in detail by Whiting and Jansen [65]. The same reference also provides the remaining flow discretization details.

2.3 Large-Eddy simulation

The rescaling-recycling method is used to develop physically meaningful fluctuations at the inflow of the domain for DNS and LES. In DNS the flow is resolved completely by the numerical method and no turbulence modeling is needed. In LES the large-scale of the turbulent flow, carrying most of the energy, is resolved by the numerical equations and the small-scale unresolved residual motions are modeled using eddy viscosity. The LES equations are obtained from the Navier-Stokes equations by applying a homogeneous spatial filter. Let $G(\boldsymbol{x}, \boldsymbol{y}, \bar{\Delta})$ be the filter kernel, then the filtered velocity is given by

$$\overline{u}_i(\boldsymbol{x}, t) = \int_\Omega G(\boldsymbol{x}, \boldsymbol{y}, \bar{\Delta}) u_i(\boldsymbol{y}, t) d\boldsymbol{y} \tag{2.30}$$

where $\bar{\Delta}$ is the filter width. The total velocity can then be written as a sum of the filtered velocity which is resolved and the residual component:

$$u_i = \overline{u}_i + u_i'' \tag{2.31}$$

The LES equations are obtained by filtering the incompressible Navier-Stokes equations (2.22-2.23):

- Continuity equation

$$\overline{u}_{i,i} = 0 \tag{2.32}$$

- Momentum equations

$$\overline{u}_{i,t} + [\overline{u}_i \overline{u}_j]_{,j} = \frac{-\overline{P}_{,i}}{\rho} + (\overline{\tau}_{ij} - \tau_{ij}^{(d)})_{,j} \tag{2.33}$$

where the residual stress is given by

$$\tau_{ij}^{(r)} = \overline{u_i u_j} - \overline{u}_i \overline{u}_j = \tau_{ij}^{(d)} + \frac{1}{3}\tau_{kk}^{(r)}\delta_{ij} \tag{2.34}$$

and $\overline{P}$ is the modified resolved pressure given by

$$\overline{P} = \overline{p} + \frac{1}{3}\tau_{kk}^{(r)} \tag{2.35}$$

$\tau_{ij}^{(d)}$ is the deviatoric part of the residual stress that is modeled. The simplest and most common model is due to Smagorinsky [49] who related the residual stress tensor $\tau_{ij}^{(d)}$ to the strain rate tensor through an eddy viscosity:

$$\tau_{ij}^{(d)} = -2\nu_T S_{ij} \tag{2.36}$$

where S_{ij} is

$$S_{ij} = \frac{1}{2}(\overline{u}_{i,j} + \overline{u}_{j,i}) \tag{2.37}$$

and ν_T is the eddy viscosity given by

$$\nu_T = C_S \bar{\Delta}^2 \left|S\right| \tag{2.38}$$

where

$$|S| = \sqrt{2S_{ij}S_{ij}} \tag{2.39}$$

C_S is the Smagorinsky constant.

In the LES on finite element topologies, the discretization itself is often the filter, called the grid filter. In this case the filter width $\bar{\Delta}$ is generally estimated as the shape of the grid filter is not known.

Other LES model widely used is the dynamic model developed by Germano *et al.* [20] and Lilly [36] where the C_S parameter is not a constant anymore, but varies in space and time. This is obtained by filtering the LES equations above (2.32 - 2.33) a second time using a test filter. This method still has a parameter that is not completely known. It is the filter width ratio between the two filters. The filter width from the test filter is easily calculable, but the filter width from the primary filter that is the finite element discretization is not known explicitly. This filter width ratio is dynamically calculated if a second test filter is used over the already twice filtered LES equations in the dynamic filter width ratio (DFWR) model developed by [59, 61, 60].

In the recycling-rescaling method developed in the next chapter, the instantaneous velocity is divided into a mean and a fluctuating part as it will be shown in 3.1.1 (eq. 3.1). In the case of LES modeling, the resolved velocity which is the solution to the LES equations (2.32 - 2.33) is considered the instantaneous velocity and as such is divided into a mean and a fluctuating part as follows:

$$\overline{u}_i = U_i + u'_i \tag{2.40}$$

where for the zero pressure gradient turbulent boundary layer is averaged in time and spanwise homogeneous direction (z):

$$U_i = \langle \langle \overline{u}_i \rangle_z \rangle_t \tag{2.41}$$

So the total velocity can be written as:

$$u_i = U_i + u'_i + u''_i \tag{2.42}$$

where u''_i is the modeled residual velocity.

2.3.1 Wall modeling

Wall modeling is used when the viscous sublayer of the boundary layer is not resolved and thus the first point in the interior of the domain is located in the log layer. The wall modeling that is used in this work is the effective viscosity approach in which the local effective viscosity is computed which produces the stress that brings the fluid to rest at the wall satisfying the log law in the mean.

It is assumed that U_i satisfies the Spalding equation [55] from which the friction velocity is calculated as follows. Lets define $U_{\|i}$ to be the flow parallel to the wall:

$$U_{\|i} = U_i - u_i(U_j n_j) \tag{2.43}$$

where n_i are the components of the normal to the wall vector. The speed parallel to the wall is defined as $\left|U_{\|}\right|$. To have both the log law and the law of the wall satisfied $f(\left|U_{\|}\right|, y_n, \nu, u_\tau)$ needs to be minimized where y_n is the distance to the wall and f is the Spalding equation given by:

$$f(\left|U_{\|}\right|, y_n, \nu, u_\tau) = -y^+ + u^+ + e^{-\kappa B}\left[e^{-\kappa u^+} - 1 - \kappa u^+ - \frac{(\kappa u^+)^2}{2} - \frac{(\kappa u^+)^3}{6}\right] \quad (2.44)$$

where $u^+ = \frac{\left|U_{\|}\right|}{u_\tau}$ and $y^+ = \frac{y_n u_\tau}{\nu}$. In this equation only the friction velocity u_τ is unknown. Thus, once u_τ is solved for, the local effective viscosity is calculated as follows:

$$\nu_{eff} = \frac{u_\tau^2 y_n}{\left|u_{\|}\right|} \quad (2.45)$$

In this equation $\left|u_{\|}\right|$, which is calculated similarly to equation (2.43), maintains the spatial inhomogeneity of turbulence.

In the next chapter, the focus will be on the mean U_i and the fluctuating part u_i'. As in DNS method all scale are resolved numerically the instantaneous velocity is the total velocity. So u_i'' does not exists.

CHAPTER 3
SCALED PLANE EXTRACTION BOUNDARY CONDITION

3.1 General case

The core assumption for Scaled Plane Extraction Boundary Condition (SPEBC) is that the boundary layer has the mean velocity profiles for different streamwise locations that collapse to the same curve when using similarity variables. More directly put, the SPEBC is a method of imposing boundary condition at the inflow of the computational domain by rescaling the velocity field at a downstream location and then prescribing the rescaled solution at the inlet plane.

First the method will be developed for incompressible, zero pressure gradient case where only velocity components are rescaled, then in section 3.1.3 the rescaling will be expanded for pressure and temperature so that compressible cases can be studied.

3.1.1 Incompressible, zero pressure gradient case

By imposing statistical homogeneity in one direction, the average velocity field in the stationary turbulent boundary layer is essentially two-dimensional. The mean velocity components, U_i, are averaged in time and in the spanwise direction. Lets define the velocity fluctuation as follows:

$$u_i'(\boldsymbol{x}, t) = u_i(\boldsymbol{x}, t) - U_i(x, y) \tag{3.1}$$

In this equation u_i are instantaneous velocity components and are function of time t and space $\boldsymbol{x} = (x, y, z)^T$; i is the index going from 1 to 3 for the three directions (x, y, z - respectively streamwise, normal and spanwise directions); u_i' are the fluctuations, they are also function of time and space; and as U_i are the mean velocity components, they are only function of x and y. As a consequence of spanwise homogeneity, $W = U_3 = 0$, i.e. there is no mean spanwise velocity component.

The governing equation for the incompressible, zero pressure gradient boundary layer is given in [62] is:

$$U\frac{\partial U}{\partial x} + V\frac{\partial U}{\partial y} = \frac{\partial}{\partial y}\left[-\langle u'v'\rangle + \nu\frac{\partial U}{\partial y}\right] - \left\{\frac{\partial}{\partial x}\left[\langle u'^2\rangle - \langle v'^2\rangle\right]\right\} \tag{3.2}$$

where $U \rightarrow U_\infty$ as $y \rightarrow \infty$ and $U = 0$ as $y = 0$. In equation (3.2), $\langle u'^2\rangle$ and $\langle v'^2\rangle$ are normal Reynolds stresses and $\langle u'v'\rangle$ is the shear Reynolds stress. These quantities are averaged in time and homogeneous direction and come from averaging the Navier-Stokes equations (2.23). The terms in the curly brackets of eq. (3.2) are second order terms and only important when pressure gradient is nonzero. The $\langle v'^2\rangle$ term arises from the substitution of the pressure term in the integral of the y momentum equation [62].

The turbulent boundary layer is governed by two distinct regions: the inner region very close to the wall where the viscous term is dominant and the outer inviscid region with viscous-dominated inner boundary conditions set by the inner layer. The outer region is comprised of most of the boundary layer. Consequently, the following equations and boundary conditions need to be satisfied for the mean velocity:

- for inner layer
$$0 = \frac{\partial}{\partial y}\left[-\langle u'v'\rangle + \nu\frac{\partial U}{\partial y}\right] \tag{3.3}$$
with $U = 0$ at $y = 0$.

- for outer layer
$$U\frac{\partial U}{\partial x} + V\frac{\partial U}{\partial y} = \frac{\partial}{\partial y}\left[-\langle u'v'\rangle\right] \tag{3.4}$$
with $U \rightarrow U_\infty$ as $y \rightarrow \infty$.

Equation (3.3) can be directly integrated to obtain the friction velocity:

$$-\langle u'v'\rangle + \nu\frac{\partial U}{\partial y} = \frac{\tau_w}{\rho} \equiv u_\tau^2 \tag{3.5}$$

This gives rise naturally to the following scaling for the streamwise mean velocity,

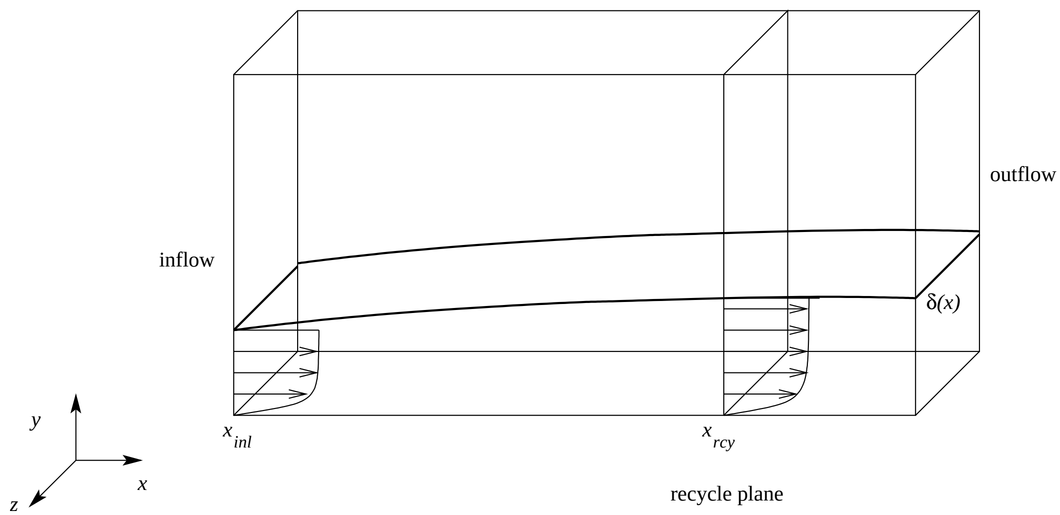

Figure 3.1: Schematics of the flat plate boundary layer

called the law of the wall:

$$\frac{U}{u_\tau} = f_i\left[y^+\right] \tag{3.6}$$

where the wall coordinate, y^+ is given by

$$y^+ = \frac{yu_\tau}{\nu} \tag{3.7}$$

The divison of the turbulent boundary layer into inner and outer layers is used to develop the rescaling recycling equations in the next section.

3.1.2 Rescaling recycling equations for velocity

The SPEBC uses the similarity scaling laws to introduce fluctuation information to the inflow in a consistent manner. The turbulent boundary layer has different similarity solutions for the different layers (inner vs. outer), for the different decomposed parts (mean U_i and fluctuation u_i') and, potentially, for different cartesian components. Lets define them as follow:

$$U^{inner}(x, y^+) = U_{si}(x)f_{1i}(y^+) \tag{3.8}$$

$$U_\infty(x) - U^{outer}(x, \eta) = U_{so}(x)f_{1o}(\eta) \tag{3.9}$$

$$V^{inner}(x, y^+) = V_{si}(x)f_{2i}(y^+) \tag{3.10}$$

$$V^{outer}(x,\eta) = V_{so}(x) f_{2o}(\eta) \tag{3.11}$$

$$(u_i')^{inner}(x,y^+,z,t) = u_{si}(x) f_{3i}(y^+,z,t) \tag{3.12}$$

$$(u_i')^{outer}(x,\eta,z,t) = u_{so}(x) f_{3o}(\eta,z,t) \tag{3.13}$$

where y^+ is given by equation (3.7) and η by:

$$\eta = \frac{y}{\delta(x)} \tag{3.14}$$

In the SPEBC the flow solution from an internal plane normal to the streamwise direction is rescaled using these equations (3.8 - 3.13) and put as an inflow boundary condition. Let that internal plane be known as the recycling plane and denoted with the subscript rcy; the subscript inl will represent the inlet plane. Figure (3.1) shows the schematics of the flat plate boundary layer geometry. The inlet and recycle planes are represented as x_{inl} and x_{rcy} respectively.

As the flow solution at the recycle plane is already computed, U_{rcy}, V_{rcy} and $(u_i')_{rcy}$ are all known. Also the x-coordinate of the inlet and the recycle planes is known. Depending on the scaling laws used, U_{si}, U_{so}, V_{si}, V_{so}, u_{si} and u_{so} are all known functions of x. Thus they are known at, both, the inlet and recycle planes.

From these quantities the streamwise mean velocity at the inlet can be calculated as follows:

- In the inner layer, for a given y^+:

$$U_{rcy}^{inner} = U_{si}(x_{rcy}) f_{1i}(y^+) \tag{3.15}$$

$$U_{inl}^{inner} = U_{si}(x_{inl}) f_{1i}(y^+) \tag{3.16}$$

From equation (3.15) f_{1i} is calculated as:

$$f_{1i}(y^+) = \frac{U_{rcy}^{inner}}{U_{si}(x_{rcy})} \tag{3.17}$$

which is substituted into equation (3.16) and U_{inl}^{inner} is calculated:

$$U_{inl}^{inner} = \frac{U_{si}(x_{inl})}{U_{si}(x_{rcy})} U_{rcy}^{inner} \tag{3.18}$$

- In the outer layer, for a given η:

$$U_\infty(x_{rcy}) - U_{rcy}^{outer} = U_{so}(x_{rcy}) f_{1o}(\eta) \tag{3.19}$$

$$U_\infty(x_{inl}) - U_{inl}^{outer} = U_{so}(x_{inl}) f_{1o}(\eta) \tag{3.20}$$

From equation (3.19) f_{1o} is calculated as:

$$f_{1o}(\eta) = \frac{U_\infty(x_{rcy}) - U_{rcy}^{outer}}{U_{so}(x_{rcy})} \tag{3.21}$$

which is substituted into equation (3.20):

$$U_\infty(x_{inl}) - U_{inl}^{outer} = \frac{U_{so}(x_{inl})}{U_{so}(x_{rcy})} [U_\infty(x_{rcy}) - U_{rcy}^{outer}] \tag{3.22}$$

which gives U_{inl}^{outer}:

$$U_{inl}^{outer} = \frac{U_{si}(x_{inl})}{U_{si}(x_{rcy})} U_{rcy}^{outer} + U_\infty(x_{inl}) - \frac{U_{si}(x_{inl})}{U_{si}(x_{rcy})} U_\infty(x_{rcy}) \tag{3.23}$$

If U_∞ is a constant, equation (3.23) becomes:

$$U_{inl}^{outer} = \frac{U_{si}(x_{inl})}{U_{si}(x_{rcy})} U_{rcy}^{outer} + \left(1 - \frac{U_{si}(x_{inl})}{U_{si}(x_{rcy})}\right) U_\infty \tag{3.24}$$

In the same way the other inlet quantities are also calculated. Therefore, the inlet boundary condition on the velocity field becomes:

$$U_{inl}^{inner} = \frac{U_{si,inl}}{U_{si,rcy}} U_{rcy}^{inner} \tag{3.25}$$

$$U_{inl}^{outer} = \frac{U_{so,inl}}{U_{so,rcy}} U_{rcy}^{outer} + \left(1 - \frac{U_{so,inl}}{U_{so,rcy}}\right) U_\infty \tag{3.26}$$

$$V_{inl}^{inner} = \frac{V_{si,inl}}{V_{si,rcy}} V_{rcy}^{inner} \tag{3.27}$$

$$V_{inl}^{outer} = \frac{V_{so,inl}}{V_{so,rcy}} V_{rcy}^{outer} \tag{3.28}$$

$$(u_i')_{inl}^{inner} = \frac{u_{si,inl}}{u_{si,rcy}} (u_i')_{rcy}^{inner} \tag{3.29}$$

$$(u_i')_{inl}^{outer} = \frac{u_{so,inl}}{u_{so,rcy}} (u_i')_{rcy}^{outer} \tag{3.30}$$

for a given y^+ in the inner region or η in the outer region for the mean flow quantities. For the fluctuations, equation (3.29) is valid for a given y^+, z and t and equation (3.30) is valid for a given η, z and t.

Equations (3.25) through (3.30) give how the solution from the recycle plane is rescaled to obtain the solution at the inflow. For a given inflow point $(x, y, z)_{inl}$ the solution at the recycle plane is taken from two different points, one for the inner region, $(x, y, z)_{rcy}^{inner}$, and one for the outer region, $(x, y, z)_{rcy}^{outer}$. Due to the similarity of the velocity in inner and outer regions, it is set $y_{inl}^+ = y_{rcy}^+$ and $\eta_{inl} = \eta_{rcy}$ in inner and outer regions respectively. Using this, the two recycle points from which the solution is rescaled are:

$$(x, y, z)_{rcy}^{inner} = \left(x_{rcy}, \frac{u_{\tau,inl}}{u_{\tau,rcy}} y_{inl}, z_{inl} \right) \tag{3.31}$$

$$(x, y, z)_{rcy}^{outer} = \left(x_{rcy}, \frac{\delta_{rcy}}{\delta_{inl}} y_{inl}, z_{inl} \right) \tag{3.32}$$

Using equations (3.25, 3.27 and 3.29) evaluated at the point given by equation (3.31) and equations (3.26, 3.28 and 3.30) evaluated at the point given by equation (3.32), the instantaneous velocity at the inlet plane is given by:

$$(u_i)_{inl} = \left[(U_i)_{inl}^{inner} + (u_i')_{inl}^{inner} \right] \{1 - W(\eta_{inl})\} + \left[(U_i)_{inl}^{outer} + (u_i')_{inl}^{outer} \right] W(\eta_{inl}) \tag{3.33}$$

where $W(\eta)$ is the weighting function that blends the solution from the inner layer to the outer layer smoothly.

A good candidate, used in this work, for the weighting function $W(\eta)$ (Fig. 3.2) is given by

$$W(\eta) = \frac{1}{2} \left\{ 1 + \frac{\tanh\left(\frac{\alpha(\eta - b)}{(1-2b)\eta + b} \right)}{\tanh(\alpha)} \right\} \tag{3.34}$$

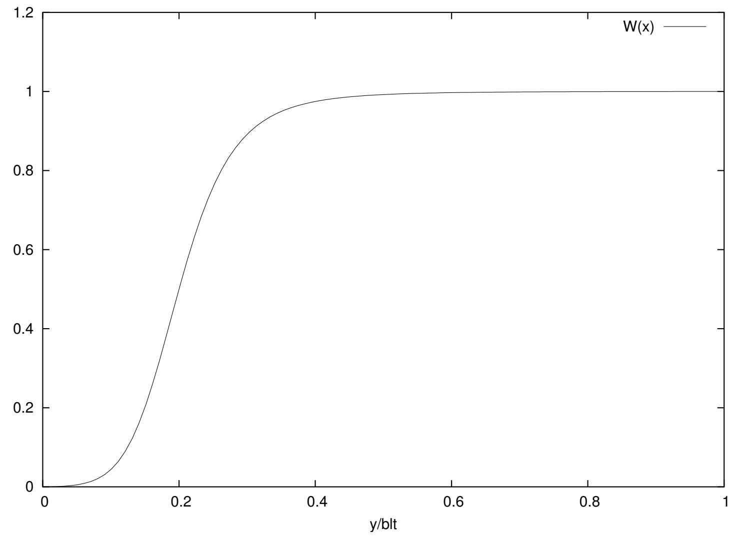

Figure 3.2: Weighting function with $\alpha = 4$ and $b = 0.2$

where $\alpha = 4$ and $b = 0.2$. The parameter b is the center of the overlap region and α is its spread. These two parameters were chosen so that the inner region is small compare to the outer region with a sufficient overlap region.

3.1.3 Pressure and temperature

In the last section, the rescaling-recycling method was described for the velocity variables. The same method can be applied to pressure and temperature. In compressible cases, as pressure is important, it is imposed as a Dirichlet condition. Temperature is a variable in icnompressible flows when temperature variation or heat flux are of interest, and in compressible flows as the energy equation is coupled to the momentum and continuity equations. Therefore, in these cases, temperature is imposed as a Dirichlet condition at the inflow in addition to the velocity and/or pressure.

Temperature and pressure can also be decomposed similarly to equation (3.1) into a mean and a fluctuating part:

$$T'(\boldsymbol{x}, t) = T_{inst}(\boldsymbol{x}, t) + T(x, y) \tag{3.35}$$

$$p'(\boldsymbol{x}, t) = p_{inst}(\boldsymbol{x}, t) + p(x, y) \tag{3.36}$$

		Temperature	Pressure
Inner	Mean	$T_{inl}^{inner} = \gamma_{T_i} T_{rcy}^{inner} + T_{0,inl} - \gamma_{T_i} T_{0,rcy}$	$p_{inl}^{inner} = \gamma_{P_i} p_{rcy}^{inner}$
	Fluctuation	$T_{inl}^{\prime inner} = \gamma_{T_i} T_{rcy}^{\prime inner}$	$p_{inl}^{\prime inner} = \gamma_{P_i} p_{rcy}^{\prime inner}$
Outer	Mean	$T_{inl}^{outer} = \gamma_{T_o} T_{rcy}^{outer} + (1 - \gamma_{T_o}) T_\infty$	$p_{inl}^{outer} = \gamma_{P_o} p_{rcy}^{outer}$
	Fluctuation	$T_{inl}^{\prime outer} = \gamma_{T_o} T_{rcy}^{\prime outer}$	$p_{inl}^{\prime outer} = \gamma_{P_o} p_{rcy}^{\prime outer}$
Scaling	Inner	$\gamma_{T_i} = \frac{T_{si,inl}}{T_{si,rcy}}$	$\gamma_{P_i} = \frac{p_{si,inl}}{p_{si,rcy}}$
	Outer	$\gamma_{T_o} = \frac{T_{so,inl}}{T_{so,rcy}}$	$\gamma_{P_o} = \frac{p_{so,inl}}{p_{so,rcy}}$

Table 3.1: Inlet temperature and pressure components computed from the recycle values

Then, similarity solutions can be written for inner and outer regions for the mean and fluctuating part of temperature:

$$T_0(x) - T^{inner}(x, y^+) = T_{si}(x) f_{Ti}(y^+) \quad (3.37)$$

$$T^{outer}(x, \eta_T) - T_\infty = T_{so}(x) f_{To}(\eta_T) \quad (3.38)$$

$$(T_i')^{inner}(x, y^+, z, t) = T_{si}'(x) f_{Tpi}(y^+, z, t) \quad (3.39)$$

$$(T_i')^{outer}(x, \eta_T, z, t) = T_{so}'(x) f_{Tpo}(\eta_T, z, t) \quad (3.40)$$

In these equations T_0 is the temperature distribution at the wall, T_∞ is the temperature in free stream and $\eta_T = \frac{y}{\delta_T}$ where δ_T is the thermal boundary layer thickness. Pressure is decomposed in the following way:

$$p^{inner}(x, y^+) = P_{si}(x) f_{Pi}(y^+) \quad (3.41)$$

$$p^{outer}(x, \eta) = P_{so}(x) f_{Po}(\eta) \quad (3.42)$$

$$(p_i')^{inner}(x, y^+, z, t) = p_{si}(x) f_{pi}(y^+, z, t) \quad (3.43)$$

$$(p_i')^{outer}(x, \eta, z, t) = p_{so}(x) f_{po}(\eta, z, t) \quad (3.44)$$

Table 3.1 gives the equations for calculating the inner and outer temperature and pressure mean and fluctuating parts at the inlet from the temperature and pressure solutions at the recycle plane.

3.2 Lund, Wu and Squires Scaling Law

Most of current methods in literature are based on the model proposed by Lund, Wu and Squires (LWS) [40], where the scaling laws are based on the self-preservation hypothesis of Townsend [63]: according to which *the flow will forget its origins and can be modeled by its local properties.* This procedure considers the friction velocity, u_τ, as a unique scaling parameter for the inner and outer quantities using the law of the wall as defined by equation (3.6) in the inner portion of the boundary layer and the defect law in the outer portion. The defect law equation states:

$$\frac{U_\infty - U}{u_\tau} = -\frac{1}{\kappa}\ln(\eta) + A \tag{3.45}$$

The nondimensional variables used are defined by (3.7) for the inner layer and by (3.14) for the outer region. For the law of the wall, the friction velocity is defined as follows:

$$u_\tau = \sqrt{\nu\left(\frac{\partial u}{\partial y}\right)_{wall}} \tag{3.46}$$

With these laws the similarity functions $U_{si}, U_{so}, V_{si}, V_{so}, u_{si}$ and u_{so} are defined in the following manner:

$$U_{si} = U_{so} = u_{si} = u_{so} = u_\tau \tag{3.47}$$

$$V_{si} = V_{so} = U_\infty \tag{3.48}$$

The instantaneous velocity at the inflow can then be calculated using equation (3.33) where the mean velocities and the fluctuations at the inlet plane are related to those of the recycle plane as follows:

$$U_{inl}^{inner} = \gamma U_{rcy}\left(y|_{y^+_{inl}}\right) \tag{3.49}$$

$$U_{inl}^{outer} = \gamma U_{rcy}\left(y|_{\eta_{inl}}\right) + (1-\gamma)\,U_\infty \tag{3.50}$$

$$V_{inl}^{inner} = V_{rcy}\left(y|_{y^+_{inl}}\right) \tag{3.51}$$

$$V_{inl}^{outer} = V_{rcy}\left(y|_{\eta_{inl}}\right) \tag{3.52}$$

$$(u_i')_{inl}^{inner} = \gamma\,(u_i')_{rcy}^{inner}\left(y|_{y^+_{inl}}, z_{inl}, t_n\right) \tag{3.53}$$

$$(u_i')_{inl}^{outer} = \gamma\,(u_i')_{rcy}^{outer}\left(y|_{\eta_{inl}}, z_{inl}, t_n\right) \tag{3.54}$$

where

$$\gamma = \frac{u_{\tau,inl}}{u_{\tau,rcy}} \tag{3.55}$$

and t_n is the current, instantaneous time at which the rescaling is performed.

For the scaling both u_τ and δ need to be known at the inflow and the recycle plane. At the recycle plane those quantities can be determined from the mean velocity profile, but for the inlet plane they need to be specified. In reality only δ_{inl} needs to be specified as $u_{\tau,inl}$ can be obtained by:

$$u_{\tau,inl} = u_{\tau,rcy} \left(\frac{\theta_{rcy}}{\theta_{inl}} \right)^{1/8} \tag{3.56}$$

where θ is the momentum thickness given by [62]:

$$\theta = \int_0^\infty \frac{U}{U_\infty} \left(1 - \frac{U}{U_\infty} \right) dy \tag{3.57}$$

The empirical relation (3.56) can be derived from the standard power law approximations $C_f \sim Re_x^{-1/n}$ and $\frac{\theta}{x} \sim Re_x^{-1/n}$ with $n = 5$ [40, 64, 43].

θ_{rcy} and θ_{inl} are calculated using equation (3.57) by approximating the integral with a sum over the turbulent boundary layer. The friction velocity, $u_{\tau,rcy}$, is calculated by equation (3.46) if it is the wall resolved case or using the Spalding law [55] if it is the wall modeled case (see section 2.3.1 for wall model).

3.3 Alternative Scaling Laws for SPEBC

The alternative scaling that is proposed here is based on the asymptotic invariance principle devised by George and Castillo [18] and it is derived in collaboration with Dr. Castillo and his student Jorge Bailon-Cuba. The asymptotic invariance principle seeks full similarity solutions of the inner and outer equations separately. It starts with the following forms of the solutions sought in the limit as $Re \to \infty$:

- for inner region:

$$U = U_{si}(x) f_{i\infty}(y^+; *) \tag{3.58}$$

$$- < uv > = R_{si_{uv}} r_{i\infty}(y^+; *) \tag{3.59}$$

$$y^+ \equiv \frac{y}{\varphi(x)} \tag{3.60}$$

- for outer region:

$$U - U_\infty = U_{so}(x) f_{o\infty}(\eta; *) \tag{3.61}$$

$$- < uv > = R_{so_{uv}}(x) r_{o\infty}(\eta; *) \tag{3.62}$$

$$\eta \equiv \frac{y}{\delta(x)} \tag{3.63}$$

In these equations, *, represent any possible dependence on the upstream conditions. $U_{si}, f_i, R_{si_{uv}}, r_i, \varphi(x), U_{si}, f_o, R_{so_{uv}}$ and r_o need to be determined by incorporating the equations (3.58 - 3.63) into equations (3.3) and (3.4) and then arranging them with terms of same x-dependence separately. This yields for the outer region:

$$\left[\frac{U_\infty}{U_{so}} \frac{\delta}{U_{so}} \frac{dU_{so}}{dx}\right] f_{o\infty} + \left[\frac{\delta}{U_{so}} \frac{dU_{so}}{dx}\right] {f_{o\infty}}^2 - \left[\frac{U_\infty}{U_{so}} \frac{d\delta}{dx}\right] \eta \frac{df_{o\infty}}{d\eta}$$
$$- \left\{\frac{d\delta}{dx} + \left[\frac{\delta}{U_{so}} \frac{dU_{so}}{dx}\right]\right\} \frac{df_{o\infty}}{d\eta} \int_0^\eta f_{o\infty}(\xi) d\xi = \left[\frac{R_{so_{uv}}}{{U_{so}}^2}\right] \frac{dr_{o\infty}}{d\eta} \tag{3.64}$$

Equilibrium similarity solutions exist only if all the square bracketed terms have the same x-dependence and are independent of the similarity coordinate, η. Thus, the bracketed terms must remain proportional to each other as the flow develops in the streamwise direction.

$$\frac{U_\infty}{U_{so}} \frac{\delta}{U_{so}} \frac{dU_{so}}{dx} \sim \frac{\delta}{U_{so}} \frac{dU_{so}}{dx} \sim \frac{U_\infty}{U_{so}} \frac{d\delta}{dx} \sim \frac{d\delta}{dx} \sim \frac{R_{so_{uv}}}{U_{so}^2} \tag{3.65}$$

Therefore, full similarity for the outer flow is possible only if

$$U_{so} \sim U_\infty \tag{3.66}$$

$$R_{so_{uv}} \sim U_\infty^2 \frac{d\delta}{dx} \tag{3.67}$$

$$V_{so} \sim U_\infty \frac{d\delta}{dx} \tag{3.68}$$

Equation (3.66) is obtained from comparing terms 1 and 2 or 3 and 4 of equation (3.65) and equation (3.68) is obtained from equation (3.66) in addition to terms 4 and 5 of equation (3.65).

Similarly for inner region, the full similarity is obtained when the following scalings are used:

$$U_{si} \sim u_\tau \quad (3.69)$$

$$R_{si_{uv}} \sim u_\tau^2 \quad (3.70)$$

$$V_{si} \sim u_\tau \quad (3.71)$$

$$\varphi = \frac{\nu}{u_\tau} \quad (3.72)$$

If substituting equation (3.69) into (3.58) the law of the wall (eq. 3.6) is obtained, but the velocity deficit law (eq. 3.45) is not obtained when equation (3.66) is substituted into (3.61).

It needs to be noted that the full similarity shown in equations (3.58 - 3.72) is only obtained in the limit of infinite Reynolds number [7, 8, 15, 18, 19, 10] and that no scaling law can work perfectly at finite Reynolds numbers without taking into account the upstream condition. These papers show good agreement of this theory with experimental data.

3.3.1 Similarity Analysis for the fluctuations

The rescaling-recycling method in addition to the scales from mean inner and outer velocity components needs also scales for fluctuations. Therefore, the theory by Castillo and George [18] must also be applied to fluctuations.

Starting from the momentum equation of the instantaneous flow:

$$u_{i,t} + u_j u_{i,j} = \frac{-1}{\rho} p_{,i} + \nu u_{i,jj} \quad (3.73)$$

and subtracting the momentum equation for the mean flow:

$$U_{i,t} + U_j U_{i,j} = \frac{-1}{\rho} P_{,i} + \nu U_{i,jj} - \langle u_i' u_j' \rangle_{,j} \quad (3.74)$$

the following equation for the fluctuation component u'_i is obtained:

$$u'_{i,t} + u'_j u'_{i,j} = \frac{-1}{\rho} p'_{,i} - u'_j U_{i,j} + \nu u'_{i,jj} + \langle u'_i u'_j \rangle_{,j} - (u'_i u'_j)_{,j} \tag{3.75}$$

Thus expanding equation (3.75), the three momentum equations for each of the fluctuation components are:

- for u'

$$\begin{aligned} \frac{\partial u'}{\partial t} + U\frac{\partial u'}{\partial x} + V\frac{\partial u'}{\partial y} = \frac{-1}{\rho}\frac{\partial p'}{\partial x} - u'\frac{\partial U}{\partial x} - v'\frac{\partial U}{\partial y} + \nu\left(\frac{\partial^2 u'}{\partial x^2} + \frac{\partial^2 u'}{\partial y^2} + \frac{\partial^2 u'}{\partial z^2}\right) \\ + \frac{\partial \langle u'^2 \rangle}{\partial x} + \frac{\partial \langle u'v' \rangle}{\partial y} - \frac{\partial u'^2}{\partial x} - \frac{\partial u'v'}{\partial y} - \frac{\partial u'w'}{\partial z} \end{aligned} \tag{3.76}$$

- for v'

$$\begin{aligned} \frac{\partial v'}{\partial t} + U\frac{\partial v'}{\partial x} + V\frac{\partial v'}{\partial y} = \frac{-1}{\rho}\frac{\partial p'}{\partial y} - u'\frac{\partial V}{\partial x} - v'\frac{\partial V}{\partial y} + \nu\left(\frac{\partial^2 v'}{\partial x^2} + \frac{\partial^2 v'}{\partial y^2} + \frac{\partial^2 v'}{\partial z^2}\right) \\ + \frac{\partial \langle u'v' \rangle}{\partial x} + \frac{\partial \langle v'^2 \rangle}{\partial y} - \frac{\partial u'v'}{\partial x} - \frac{\partial v'^2}{\partial y} - \frac{\partial v'w'}{\partial z} \end{aligned} \tag{3.77}$$

- for w'

$$\begin{aligned} \frac{\partial w'}{\partial t} + U\frac{\partial w'}{\partial x} + V\frac{\partial w'}{\partial y} = \frac{-1}{\rho}\frac{\partial p'}{\partial z} + \nu\left(\frac{\partial^2 w'}{\partial x^2} + \frac{\partial^2 w'}{\partial y^2} + \frac{\partial^2 w'}{\partial z^2}\right) \\ + \frac{\partial \langle u'w' \rangle}{\partial x} + \frac{\partial \langle v'w' \rangle}{\partial y} - \frac{\partial u'w'}{\partial x} - \frac{\partial v'w'}{\partial y} - \frac{\partial w'^2}{\partial z} \end{aligned} \tag{3.78}$$

The magnitude of the fluctuations is considered of same order for all 3 components $u' \sim v' \sim w'$ in a turbulent boundary layer which can be seen by the numerical results shown in Figures 3.3 - 3.5. These results, presented in section 5.2, illustrate the assumptions for inner and outer regions on fluctuations and their gradients. Figure 3.3 shows the velocity fluctuation in the inner layer at $y^+ = 5$ and Figure 3.4 in the outer layer at $y^+ = 120$. The normal plane in these two figures shows the fluctuation change in the boundary layer as we move from the flat plate to the freestream. It is clear that the three fluctuation components are of same order

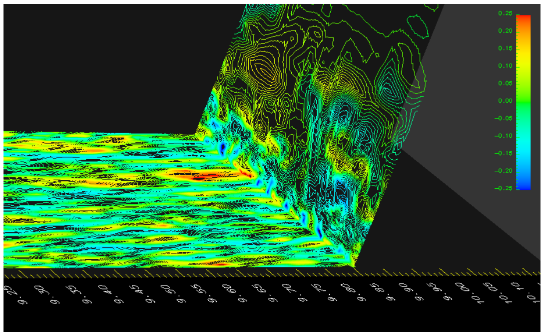

(a) u'

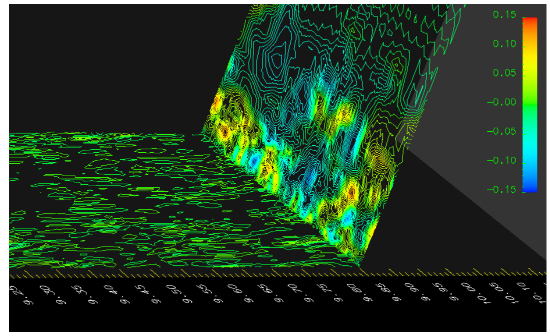

(b) v'

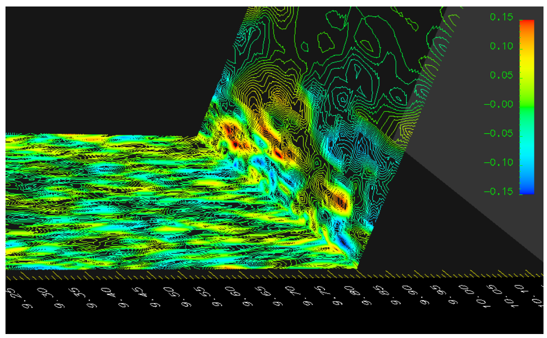

(c) w'

Figure 3.3: Fluctuation at $y^+ = 5$ (in inner region) and at a normal plane to the flow

of magnitude. Since the streamwise length scale is larger than the boundary layer thickness $\delta \ll L$, it follows that for the mean quantities:

$$\frac{\partial}{\partial x} \ll \frac{\partial}{\partial y}$$

With this assumption, equations (3.76)-(3.78) can be rewritten for turbulent boundary layers:

- for u'

$$\frac{\partial u'}{\partial t} + U\frac{\partial u'}{\partial x} + V\frac{\partial u'}{\partial y} = \frac{-1}{\rho}\frac{\partial p'}{\partial x} - v'\frac{\partial U}{\partial y} + \nu\left(\frac{\partial^2 u'}{\partial x^2} + \frac{\partial^2 u'}{\partial y^2} + \frac{\partial^2 u'}{\partial z^2}\right) + \frac{\partial \langle u'v' \rangle}{\partial y} - \frac{\partial u'^2}{\partial x} - \frac{\partial u'v'}{\partial y} - \frac{\partial u'w'}{\partial z} \quad (3.79)$$

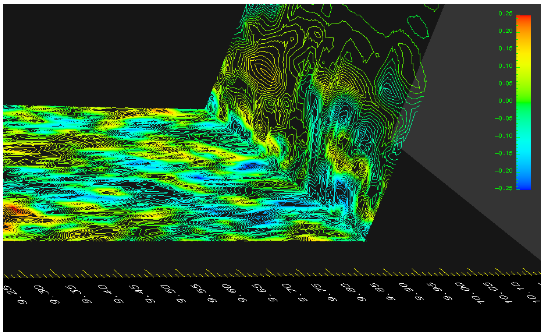

(a) u'

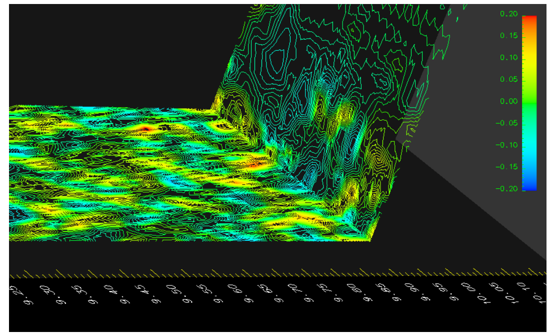

(b) v'

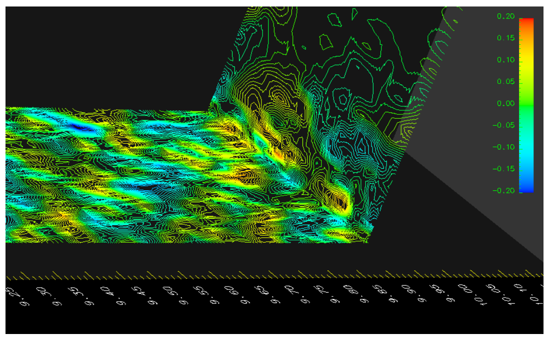

(c) w'

Figure 3.4: Fluctuation at $y^+ = 120$ (in outer region) and at a normal plane to the flow

- for v'

$$\frac{\partial v'}{\partial t} + U\frac{\partial v'}{\partial x} + V\frac{\partial v'}{\partial y} = \frac{-1}{\rho}\frac{\partial p'}{\partial y} - v'\frac{\partial V}{\partial y} + \nu\left(\frac{\partial^2 v'}{\partial x^2} + \frac{\partial^2 v'}{\partial y^2} + \frac{\partial^2 v'}{\partial z^2}\right) + \frac{\partial \langle v'^2 \rangle}{\partial y} - \frac{\partial u'v'}{\partial x} - \frac{\partial v'^2}{\partial y} - \frac{\partial v'w'}{\partial z} \quad (3.80)$$

- for w'

$$\frac{\partial w'}{\partial t} + U\frac{\partial w'}{\partial x} + V\frac{\partial w'}{\partial y} = \frac{-1}{\rho}\frac{\partial p'}{\partial z} + \nu\left(\frac{\partial^2 w'}{\partial x^2} + \frac{\partial^2 w'}{\partial y^2} + \frac{\partial^2 w'}{\partial z^2}\right) + \frac{\partial \langle v'w' \rangle}{\partial y} - \frac{\partial u'w'}{\partial x} - \frac{\partial v'w'}{\partial y} - \frac{\partial w'^2}{\partial z} \quad (3.81)$$

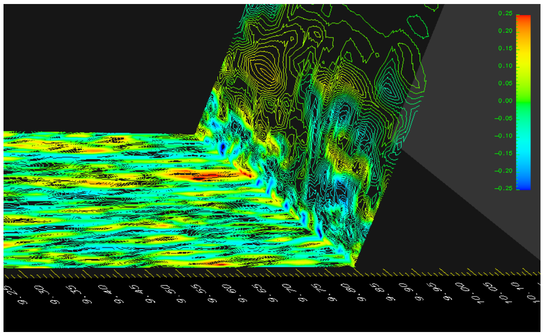

(a) $y^+ = 5$

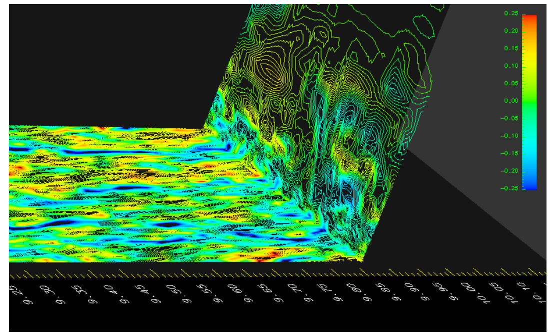

(b) $y^+ = 30$

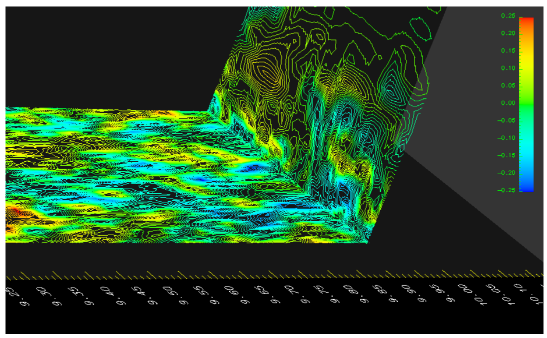

(c) $y^+ = 120$

Figure 3.5: u' fluctuation at different y^+ planes and at a normal plane to the flow

3.3.1.1 Inner layer

Looking at Figure 3.5 which shows u' at three different locations inside the boundary layer, i.e. $y^+ = 5$, 30 and 120, it is seen that in the inner layer the gradient in the streamwise direction is smaller than in the other two directions. Indeed the cigarlike structures can be seen in 3.5(a) and 3.5(b), but not in 3.5(c). When calculating the gradients in these regions we can conclude that $\frac{\partial u'}{\partial x} << \frac{\partial u'}{\partial y}$ and $\frac{\partial u'}{\partial y} \sim \frac{\partial u'}{\partial z}$. This assumption cannot be made in the outer region as all three gradient components are of the same order. When looking at v' and w' same conclusion can be drawn. Also, in the inner layer the left-hand side of equations (3.79) - (3.81) can be neglected, thus equations (3.79) - (3.81) can be rewritten as:

$$\frac{\partial u'}{\partial t} = \frac{-1}{\rho}\frac{\partial p'}{\partial x} - v'\frac{\partial U}{\partial y} + \nu\left(\frac{\partial^2 u'}{\partial y^2} + \frac{\partial^2 u'}{\partial z^2}\right) + \frac{\partial \langle u'v' \rangle}{\partial y} - \frac{\partial u'v'}{\partial y} - \frac{\partial u'w'}{\partial z} \quad (3.82)$$

$$\frac{\partial v'}{\partial t} = \frac{-1}{\rho}\frac{\partial p'}{\partial y} - v'\frac{\partial V}{\partial y} + \nu\left(\frac{\partial^2 v'}{\partial y^2} + \frac{\partial^2 v'}{\partial z^2}\right) + \frac{\partial \langle v'^2 \rangle}{\partial y} - \frac{\partial v'^2}{\partial y} - \frac{\partial v'w'}{\partial z} \quad (3.83)$$

	$\frac{\partial}{\partial t}$	$\frac{\partial}{\partial y}$	$\frac{\partial}{\partial z}$
u'	$\frac{u_{si}}{\tau_i}\frac{\partial f_{ui}}{\partial T_i}$	$\frac{u_{si}u_\tau}{\nu}\frac{\partial f_{ui}}{\partial y^+}$	$\frac{u_{si}}{\varphi(x)}\frac{\partial f_{ui}}{\partial z^+}$
v'	$\frac{v_{si}}{\tau_i}\frac{\partial f_{vi}}{\partial T_i}$	$\frac{v_{si}u_\tau}{\nu}\frac{\partial f_{vi}}{\partial y^+}$	$\frac{v_{si}}{\varphi(x)}\frac{\partial f_{vi}}{\partial z^+}$
w'	$\frac{w_{si}}{\tau_i}\frac{\partial f_{wi}}{\partial T_i}$	$\frac{w_{si}u_\tau}{\nu}\frac{\partial f_{wi}}{\partial y^+}$	$\frac{w_{si}}{\varphi(x)}\frac{\partial f_{wi}}{\partial z^+}$

Table 3.2: Partial derivatives for fluctuations similarity functions for inner layer

$$\frac{\partial w'}{\partial t} = \frac{-1}{\rho}\frac{\partial p'}{\partial z} + \nu\left(\frac{\partial^2 w'}{\partial y^2} + \frac{\partial^2 w'}{\partial z^2}\right) + \frac{\partial\langle v'w'\rangle}{\partial y} - \frac{\partial v'w'}{\partial y} - \frac{\partial w'^2}{\partial z} \tag{3.84}$$

The solutions sought in the inner layer for the fluctuations are of the form:

$$u'(x,y,z,t) = u_{si}(x)f_{ui}(y^+,z^+,T_i,*) \tag{3.85}$$

$$v'(x,y,z,t) = v_{si}(x)f_{vi}(y^+,z^+,T_i,*) \tag{3.86}$$

$$w'(x,y,z,t) = w_{si}(x)f_{wi}(y^+,z^+,T_i,*) \tag{3.87}$$

where y^+ is given by equation (3.7) and * incorporates all the upstream conditions. In equations (3.85) - (3.87), u_{si}, v_{si}, w_{si} are the unknown needed for the rescaling-recycling boundary condition. The normalized spanwise variable is given by

$$z^+ = \frac{z}{\varphi(x)} \tag{3.88}$$

where $\varphi(x)$ is the spanwise length scale. T_i is the nondimensional time: $T_i = \frac{t}{\tau_i}$. To substitute equations (3.85) - (3.87) into equations (3.82) - (3.84), the first partial derivatives needed are given by Table 3.2. Thus the following equations are obtained:

- for u'

$$\begin{aligned}\frac{u_{si}}{\tau_i}\frac{\partial f_{ui}}{\partial T_i} &= \frac{-1}{\rho}\frac{\partial p'}{\partial x} - v_{si}f_{vi}\frac{u_\tau^2}{\nu}\frac{df_{1i}}{dy^+} + \frac{u_{si}u_\tau^2}{\nu}\frac{\partial^2 f_{ui}}{\partial {y^+}^2} + \frac{u_{si}\nu}{\varphi^2}\frac{\partial^2 f_{ui}}{\partial {z^+}^2} + \frac{u_\tau^3}{\nu}\frac{dr_{si_{uv}}}{dy^+} \\ &- u_{si}v_{si}\frac{u_\tau}{\nu}\left(f_{vi}\frac{\partial f_{ui}}{\partial y^+} + f_{ui}\frac{\partial f_{vi}}{\partial y^+}\right) - \frac{u_{si}w_{si}}{\varphi}\left(f_{wi}\frac{\partial f_{ui}}{\partial z^+} + f_{ui}\frac{\partial f_{wi}}{\partial z^+}\right)\end{aligned} \tag{3.89}$$

- for v'

$$\frac{v_{si}}{\tau_i}\frac{\partial f_{vi}}{\partial T_i} = \frac{-1}{\rho}\frac{\partial p'}{\partial y} - v_{si} f_{vi}\frac{u_\tau^2}{\nu}\frac{df_{2i}}{dy^+} + \frac{v_{si}u_\tau^2}{\nu}\frac{\partial^2 f_{vi}}{\partial {y^+}^2} + \frac{v_{si}\nu}{\varphi^2}\frac{\partial^2 f_{vi}}{\partial {z^+}^2} + \frac{u_\tau^3}{\nu}\frac{dr_{si_{v^2}}}{dy^+}$$
$$- \frac{v_{si}^2 u_\tau}{\nu} 2 f_{vi}\frac{\partial f_{vi}}{\partial y^+} - \frac{v_{si}w_{si}}{\varphi}\left(f_{wi}\frac{\partial f_{vi}}{\partial z^+} + f_{vi}\frac{\partial f_{wi}}{\partial z^+}\right) \quad (3.90)$$

- for w'

$$\frac{w_{si}}{\tau_i}\frac{\partial f_{wi}}{\partial T_i} = \frac{-1}{\rho}\frac{\partial p'}{\partial z} + \frac{w_{si}u_\tau^2}{\nu}\frac{\partial^2 f_{wi}}{\partial {y^+}^2} + \frac{u_\tau^3}{\nu}\frac{dr_{si_{vw}}}{dy^+}$$
$$- v_{si}w_{si}\frac{u_\tau}{\nu}\left(f_{vi}\frac{\partial f_{wi}}{\partial y^+} + f_{ui}\frac{\partial f_{vi}}{\partial y^+}\right) - \frac{w_{si}^2}{\varphi} 2 f_{wi}\frac{\partial f_{wi}}{\partial z^+} \quad (3.91)$$

For similarity solution the following terms must have the same x-dependence (pressure terms were omitted):

$$\frac{u_{si}}{\tau_i} \sim \frac{v_{si}u_\tau^2}{\nu} \sim \frac{u_{si}u_\tau^2}{\nu} \sim \frac{u_{si}\nu}{\varphi^2} \sim \frac{u_\tau^3}{\nu} \sim \frac{u_{si}v_{si}u_\tau}{\nu} \sim \frac{u_{si}w_{si}}{\varphi} \quad (3.92)$$
$$\frac{v_{si}}{\tau_i} \sim \frac{v_{si}u_\tau^2}{\nu} \sim \frac{u_\tau^3}{\nu} \sim \frac{v_{si}\nu}{\varphi^2} \sim \frac{v_{si}^2 u_\tau}{\nu} \sim \frac{v_{si}w_{si}}{\varphi} \quad (3.93)$$
$$\frac{w_{si}}{\tau_i} \sim \frac{w_{si}u_\tau^2}{\nu} \sim \frac{u_\tau^3}{\nu} \sim \frac{v_{si}w_{si}u_\tau}{\nu} \sim \frac{w_{si}^2}{\varphi} \quad (3.94)$$

which gives the following fluctuation scale for inner layer:

$$u_{si} \sim v_{si} \sim w_{si} \sim u_\tau \quad (3.95)$$

and $\varphi(x) = \frac{\nu}{u_\tau}$ which gives the same inner spanwise length scale as the normal length scale. It is also found that the inner characteristic time scale is given by $\tau_i = \frac{\nu}{u_\tau^2}$.

3.3.1.2 Outer layer

The viscous stress can be neglected as the outer layer is essentially inviscid. Therefore, the following equations for the fluctuations in the outer region are ob-

	$\frac{\partial}{\partial t}$	$\frac{\partial}{\partial x}$	$\frac{\partial}{\partial y}$	$\frac{\partial}{\partial z}$
u'	$\frac{u_{so}}{\tau_o}\frac{\partial f_{uo}}{\partial T_o}$	$\frac{du_{so}}{dx}f_{uo} - \frac{u_{so}}{\delta}\frac{d\delta}{dx}\eta\frac{\partial f_{uo}}{\partial \eta} - \frac{u_{so}}{\phi}\frac{d\phi}{dx}\eta\frac{\partial f_{uo}}{\partial \eta_z}$	$\frac{u_{so}}{\delta}\frac{\partial f_{uo}}{\partial \eta}$	$\frac{u_{so}}{\phi}\frac{\partial f_{uo}}{\partial \eta_z}$
v'	$\frac{v_{so}}{\tau_o}\frac{\partial f_{vo}}{\partial T_o}$	$\frac{dv_{so}}{dx}f_{vo} - \frac{v_{so}}{\delta}\frac{d\delta}{dx}\eta\frac{\partial f_{vo}}{\partial \eta} - \frac{v_{so}}{\phi}\frac{d\phi}{dx}\eta\frac{\partial f_{vo}}{\partial \eta_z}$	$\frac{v_{so}}{\delta}\frac{\partial f_{vo}}{\partial \eta}$	$\frac{v_{so}}{\phi}\frac{\partial f_{vo}}{\partial \eta_z}$
w'	$\frac{w_{so}}{\tau_o}\frac{\partial f_{wo}}{\partial T_o}$	$\frac{dw_{so}}{dx}f_{wo} - \frac{w_{so}}{\delta}\frac{d\delta}{dx}\eta\frac{\partial f_{wo}}{\partial \eta} - \frac{w_{so}}{\phi}\frac{d\phi}{dx}\eta\frac{\partial f_{wo}}{\partial \eta_z}$	$\frac{w_{so}}{\delta}\frac{\partial f_{wo}}{\partial \eta}$	$\frac{w_{so}}{\phi}\frac{\partial f_{wo}}{\partial \eta_z}$

Table 3.3: Partial derivatives for fluctuations similarity functions for outer layer

tained from equations (3.79) - (3.81):

$$\frac{\partial u'}{\partial t} + U\frac{\partial u'}{\partial x} + V\frac{\partial u'}{\partial y} = -\frac{1}{\rho}\frac{\partial p'}{\partial x} - v'\frac{\partial U}{\partial y} + \frac{\partial\langle u'v'\rangle}{\partial y} - \frac{\partial u'^2}{\partial x} - \frac{\partial u'v'}{\partial y} - \frac{\partial u'w'}{\partial z} \quad (3.96)$$

$$\frac{\partial v'}{\partial t} + U\frac{\partial v'}{\partial x} + V\frac{\partial v'}{\partial y} = \frac{-1}{\rho}\frac{\partial p'}{\partial y} - v'\frac{\partial V}{\partial y} + \frac{\partial\langle v'^2\rangle}{\partial y} - \frac{\partial u'v'}{\partial x} - \frac{\partial v'^2}{\partial y} - \frac{\partial v'w'}{\partial z} \quad (3.97)$$

$$\frac{\partial w'}{\partial t} + U\frac{\partial w'}{\partial x} + V\frac{\partial w'}{\partial y} = \frac{-1}{\rho}\frac{\partial p'}{\partial z} + \frac{\partial\langle v'w'\rangle}{\partial y} - \frac{\partial u'w'}{\partial x} - \frac{\partial v'w'}{\partial y} - \frac{\partial w'^2}{\partial z} \quad (3.98)$$

The solutions sought in the outer layer for the fluctuations are of the form:

$$u'(x,y,z,t) = u_{so}(x)f_{uo}(\eta,\eta_z,T_o,*) \quad (3.99)$$

$$v'(x,y,z,t) = v_{so}(x)f_{vo}(\eta,\eta_z,T_o,*) \quad (3.100)$$

$$w'(x,y,z,t) = w_{so}(x)f_{wo}(\eta,\eta_z,T_o,*) \quad (3.101)$$

where η is given by equation (3.14) and * represents the upstream dependency. The nondimensional outer spanwise variable is given by:

$$\eta_z = \frac{z}{\phi(x)} \quad (3.102)$$

and $T_o = \frac{t}{\tau_o}$ is the nondimensional time. To substitute equations (3.99) - (3.101) into equations (3.96) - (3.98), the first partial derivatives needed are given by Table 3.3. Thus the following equations are obtained:

- for u'

$$\frac{u_{so}}{\tau_o}\frac{\partial f_{uo}}{\partial T} + U_\infty(1+f_{1o})\left(\frac{du_{so}}{dx}f_{uo} - \frac{u_{so}}{\delta}\frac{d\delta}{dx}\eta\frac{\partial f_{uo}}{\partial \eta} - \frac{u_{so}}{\phi}\frac{d\phi}{dx}\eta_z\frac{\partial f_{uo}}{\partial \eta_z}\right)$$
$$+ U_\infty\frac{d\delta}{dx}f_{2o}\frac{u_{so}}{\delta}\frac{\partial f_{uo}}{\partial \eta} = \frac{-1}{\rho}\frac{\partial p'}{\partial x} - v_{so}f_{vo}\frac{U_\infty}{\delta}\frac{df_{1o}}{d\eta} + \frac{U_\infty^2}{\delta}\frac{d\delta}{dx}\frac{dr_{so_{uv}}}{d\eta}$$
$$- 2u_{so}f_{uo}\left(\frac{du_{so}}{dx}f_{uo} - \frac{u_{so}}{\delta}\frac{d\delta}{dx}\eta\frac{\partial f_{uo}}{\partial \eta} - \frac{u_{so}}{\phi}\frac{d\phi}{dx}\eta_z\frac{\partial f_{uo}}{\partial \eta_z}\right)$$
$$- v_{so}\frac{u_{so}}{\delta}\left(f_{vo}\frac{\partial f_{uo}}{\partial \eta} + f_{uo}\frac{\partial f_{vo}}{\partial \eta}\right) - w_{so}\frac{u_{so}}{\phi}\left(f_{wo}\frac{\partial f_{uo}}{\partial \eta_z} + f_{uo}\frac{\partial f_{wo}}{\partial \eta_z}\right) \quad (3.103)$$

- for v'

$$\frac{v_{so}}{\tau_o}\frac{\partial f_{vo}}{\partial T} + U_\infty(1+f_{1o})\left(\frac{dv_{so}}{dx}f_{vo} - \frac{v_{so}}{\delta}\frac{d\delta}{dx}\eta\frac{\partial f_{vo}}{\partial \eta} - \frac{v_{so}}{\phi}\frac{d\phi}{dx}\eta_z\frac{\partial f_{vo}}{\partial \eta_z}\right)$$
$$+ U_\infty\frac{d\delta}{dx}f_{2o}\frac{v_{so}}{\delta}\frac{\partial f_{vo}}{\partial \eta} = \frac{-1}{\rho}\frac{\partial p'}{\partial y} - v_{so}f_{vo}\frac{U_\infty}{\delta}\frac{d\delta}{dx}\frac{df_{2o}}{d\eta} + \frac{R_{so_{v2}}}{\delta}\frac{dr_{so_{v2}}}{d\eta}$$
$$- v_{so}f_{vo}\left(\frac{du_{so}}{dx}f_{uo} - \frac{u_{so}}{\delta}\frac{d\delta}{dx}\eta\frac{\partial f_{uo}}{\partial \eta} - \frac{u_{so}}{\phi}\frac{d\phi}{dx}\eta_z\frac{\partial f_{uo}}{\partial \eta_z}\right)$$
$$- u_{so}f_{uo}\left(\frac{dv_{so}}{dx}f_{vo} - \frac{v_{so}}{\delta}\frac{d\delta}{dx}\eta\frac{\partial f_{vo}}{\partial \eta} - \frac{v_{so}}{\phi}\frac{d\phi}{dx}\eta_z\frac{\partial f_{vo}}{\partial \eta_z}\right)$$
$$- \frac{v_{so}^2}{\delta}2f_{vo}\frac{\partial f_{vo}}{\partial \eta} - w_{so}\frac{v_{so}}{\phi}\left(f_{wo}\frac{\partial f_{vo}}{\partial \eta_z} + f_{vo}\frac{\partial f_{wo}}{\partial \eta_z}\right) \quad (3.104)$$

- for w'

$$\frac{w_{so}}{\tau_o}\frac{\partial f_{wo}}{\partial T} + U_\infty(1+f_{1o})\left(\frac{dw_{so}}{dx}f_{wo} - \frac{w_{so}}{\delta}\frac{d\delta}{dx}\eta\frac{\partial f_{wo}}{\partial \eta} - \frac{w_{so}}{\phi}\frac{d\phi}{dx}\eta_z\frac{\partial f_{wo}}{\partial \eta_z}\right)$$
$$+ U_\infty\frac{d\delta}{dx}f_{2o}\frac{w_{so}}{\delta}\frac{\partial f_{wo}}{\partial \eta} = \frac{-1}{\rho}\frac{\partial p'}{\partial z} + \frac{R_{so_{vw}}}{\delta}\frac{dr_{so_{vw}}}{d\eta}$$
$$- w_{so}f_{wo}\left(\frac{du_{so}}{dx}f_{uo} - \frac{u_{so}}{\delta}\frac{d\delta}{dx}\eta\frac{\partial f_{uo}}{\partial \eta} - \frac{u_{so}}{\phi}\frac{d\phi}{dx}\eta_z\frac{\partial f_{uo}}{\partial \eta_z}\right)$$
$$- u_{so}f_{so}\left(\frac{dw_{so}}{dx}f_{wo} - \frac{w_{so}}{\delta}\frac{d\delta}{dx}\eta\frac{\partial f_{wo}}{\partial \eta} - \frac{w_{so}}{\phi}\frac{d\phi}{dx}\eta_z\frac{\partial f_{wo}}{\partial \eta_z}\right)$$
$$- v_{so}\frac{w_{so}}{\delta}\left(f_{vo}\frac{\partial f_{wo}}{\partial \eta} + f_{wo}\frac{\partial f_{vo}}{\partial \eta}\right) - \frac{w_{so}^2}{\delta}2f_{wo}\frac{\partial f_{wo}}{\partial \eta} \quad (3.105)$$

For the similarity solution, the following terms must have the same x-dependence (transient and pressure terms were omitted):

$$\frac{u_{so}}{\tau_o} \sim U_\infty \frac{du_{so}}{dx} \sim \frac{U_\infty u_{so}}{\delta}\frac{d\delta}{dx} \sim \frac{U_\infty u_{so}}{\phi}\frac{d\phi}{dx} \sim \frac{v_{so}U_\infty}{\delta} \sim \frac{U_\infty^2}{\delta}\frac{d\delta}{dx} \sim u_{so}\frac{du_{so}}{dx} \sim \frac{u_{so}^2}{\delta}\frac{d\delta}{dx} \sim \frac{u_{so}^2}{\phi}\frac{d\phi}{dx} \sim \frac{u_{so}v_{so}}{\delta} \sim \frac{u_{so}w_{so}}{\phi} \quad (3.106)$$

$$\frac{v_{so}}{\tau_o} \sim U_\infty \frac{dv_{so}}{dx} \sim \frac{U_\infty v_{so}}{\delta}\frac{d\delta}{dx} \sim \frac{U_\infty v_{so}}{\phi}\frac{d\phi}{dx} \sim \frac{R_{so_{v2}}}{\delta} \sim u_{so}\frac{dv_{so}}{dx} \sim \frac{u_{so}v_{so}}{\delta}\frac{d\delta}{dx} \sim \frac{u_{so}v_{so}}{\phi}\frac{d\phi}{dx} \sim v_{so}\frac{du_{so}}{dx} \sim \frac{v_{so}^2}{\delta} \sim \frac{v_{so}w_{so}}{\phi} \quad (3.107)$$

$$\frac{w_{so}}{\tau_o} \sim U_\infty \frac{dw_{so}}{dx} \sim \frac{U_\infty w_{so}}{\delta}\frac{d\delta}{dx} \sim \frac{U_\infty w_{so}}{\phi}\frac{d\phi}{dx} \sim \frac{R_{so_{vw}}}{\delta} \sim u_{so}\frac{dw_{so}}{dx} \sim \frac{u_{so}w_{so}}{\delta}\frac{d\delta}{dx} \sim \frac{u_{so}w_{so}}{\phi}\frac{d\phi}{dx} \sim w_{so}\frac{du_{so}}{dx} \sim \frac{v_{so}w_{so}}{\delta} \sim \frac{w_{so}^2}{\phi} \quad (3.108)$$

which gives the following fluctuation scale for outer layer:

$$u_{so} \sim U_\infty \quad (3.109)$$

$$v_{so} \sim U_\infty \frac{d\delta}{dx} \quad (3.110)$$

$$w_{so} \sim U_\infty \frac{d\delta}{dx} \quad (3.111)$$

The outer spanwise length scale is the boundary layer thickness, i.e. $\phi = \delta$ and the outer characteristic time scale τ_o is given by:

$$\frac{1}{\tau_o} \sim \frac{U_\infty}{\delta}\frac{d\delta}{dx} \quad (3.112)$$

3.3.2 Scaling equations

Table 3.4 recapitulates the inner and outer scalings for both methods: LWS and the one proposed here. With these similarity scalings the instantaneous velocity at the inlet plane can be calculated by equation (3.33) where the different velocity components are calculated by the following equations:

$$U_{inl}^{inner} = \gamma U_{rcy}\left(y|_{y_{inl}^{+}}\right) \quad (3.113)$$

$$U_{inl}^{outer} = U_{rcy}\left(y|_{\eta_{inl}}\right) \quad (3.114)$$

$$V_{inl}^{inner} = \gamma V_{rcy}\left(y|_{y_{inl}^{+}}\right) \quad (3.115)$$

$$V_{inl}^{outer} = \beta V_{rcy}\left(y|_{\eta_{inl}}\right) \quad (3.116)$$

$$(u_i')_{inl}^{inner} = \gamma\,(u_i')_{rcy}^{inner}\left(y|_{y_{inl}^{+}}, z_{inl}, t_n\right) \quad (3.117)$$

$$(u')_{inl}^{outer} = (u')_{rcy}^{outer}\left(y|_{\eta_{inl}}, z_{inl}, t_n\right) \quad (3.118)$$

$$(v')_{inl}^{outer} = \beta\,(v')_{rcy}^{outer}\left(y|_{\eta_{inl}}, z_{inl}, t_n\right) \quad (3.119)$$

$$(w')_{inl}^{outer} = \beta\,(w')_{rcy}^{outer}\left(y|_{\eta_{inl}}, z_{inl}, t_n\right) \quad (3.120)$$

where γ is given by equation (3.55) and

$$\beta = \frac{\left(\frac{d\delta}{dx}\right)_{inl}}{\left(\frac{d\delta}{dx}\right)_{rcy}} \quad (3.121)$$

In the implementation of the alternative scaling, the spanwise coordinate for the fluctuations was not rescaled as in that direction, the reference location does not exist. Therefore, the recycle points where the solution is extracted are located at the same z coordinate as the inlet point of interest instead of having $z_{inl}^{+} = z_{rcy}^{+}$ and $\eta_{z,inl} = \eta_{z,rcy}$ in inner and outer regions respectively. Thus, in equation (3.117) z is used instead of z^{+} and in equations (3.118-3.120) it is used instead of η_z. Also in these four equations, the time is not rescaled as the rescaling-recycling is done instantaneously at each time step.

In LWS, the relation (eq. 3.56) between the friction velocities at both, the recycle and the inlet, planes is based on the power law. In this alternate scaling, the friction velocity is calculated using the following relation:

$$\frac{u_\tau}{U_\infty} = \frac{C_{o_\infty}}{C_{i_\infty}} {\delta^{+}}^{-\gamma_\infty} \exp\left[\frac{A}{(\ln \delta^{+})^{\alpha}}\right] \quad (3.122)$$

from George and Castillo [18]. In this equation $C_{o_\infty} = 0.897$, $C_{i_\infty} = 55$, $\gamma_\infty = 0.0362$, $A = 2.9$ and $\alpha = 0.46$; $\delta^{+} = \frac{u_\tau \delta}{\nu}$. Thus γ needed for equations (3.113) - (3.120) is

		Inner		Outer	
		LWS	Alt.	LWS	Alt.
Mean	U	u_τ	u_τ	U_∞	U_∞
	V	U_∞			$U_\infty \frac{d\delta}{dx}$
Fluctuation	u'	u_τ	u_τ	U_∞	U_∞
	v'				$U_\infty \frac{d\delta}{dx}$
	w'				$U_\infty \frac{d\delta}{dx}$

Table 3.4: Scaling velocities for LWS scaling and for the scaling based on theory by GC

given by:

$$\gamma = \frac{u_{\tau,inl}}{u_{\tau,rcy}} = \left(\frac{\delta^+_{inl}}{\delta^+_{rcy}}\right)^{-\gamma_\infty} \exp\left[\frac{A}{\left(\ln \delta^+_{inl}\right)^\alpha} - \frac{A}{\left(\ln \delta^+_{rcy}\right)^\alpha}\right] \tag{3.123}$$

This equation incorporates the local Reynolds number dependence through δ^+.

CHAPTER 4
NUMERICAL IMPLEMENTATION OF SPEBC

In this chapter, first the rescaling recycling algorithm will be presented for implementing in conjunction with a finite element method. Then specific details of the implementation for unstructured versus structured meshes, as well as axisymmetric cases will be presented. Finally, issues relevant to parallel implementation will be discussed including the calculation of the averaged velocity on the unstructured domain and the boundary layer thickness derivative needed for the alternative scaling law. The specific implementation of the rescaling recycling method used in this work will be called the Scaled Plane Extraction Boundary Condition or SPEBC for short.

4.1 Rescaling recycling algorithm

The rescaling recycling boundary condition is used to impose physically meaningful fluctuations at the inflow of a turbulent boundary layer DNS or LES simulation where the Navier Stockes equations (DNS: 2.1 - 2.3; LES: 2.32 - 2.33) are solved using a finite element method. Given a finite element mesh domain, the algorithm describing the SPEBC is:

1. Find inlet mesh nodes.

2. Locate recycle plane.

3. Locate elements cut by the recycle plane.

4. Locate points from which the solution will be averaged in homogeneous direction.

These four steps are done once at the beginning of the simulation.

Each time boundary conditions are imposed on the flow field, which is generally once per time step, the following operations need to be done:

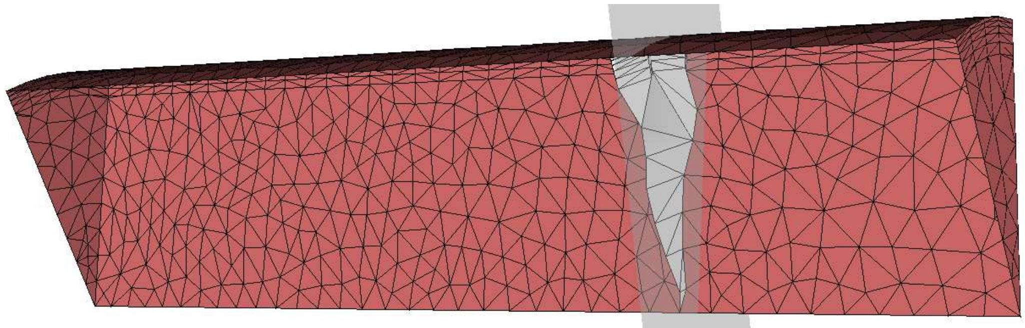

Figure 4.1: Sample mesh when using SPEBC for an axisymmetric problem

1. Calculate averaged field at recycle and inlet planes from the points determined at the beginning of the simulation in step 4.

2. Compute δ_{rcy}, $u_{\tau,rcy}$ and $u_{\tau,inl}$ and other flow parameters needed for the scaling used from the averaged velocity calculated in step 1.

3. Compute the fluctuation field at recycle plane.

4. Locate the points in the recycle plane that are "similarity-mapped" points from the actual inflow points (for both inner and outer layer scalings).

5. Interpolate mean and fluctuating solution at these points.

6. Rescale solution from the recycle plane using appropriate scales.

7. Prescribe solution at the inlet plane.

4.2 SPEBC for unstructured grids

Figure 4.1 shows a sample unstructured mesh with tetrahedral elements that is used to simulate boundary layer flows with the SPEBC. The inlet plane is located at the left of the figure. The recycle plane is shown by the shaded plane cutting the mesh. This is the virtual plane from which the velocity field will be extracted and rescaled to the inlet plane. The recycle plane is virtual as it does not have mesh vertices on which the solution is solved. To find the solution at the virtual recycle plane, first the elements that are cut by this plane need to be located as the solution on vertices of these elements will be used to extract the solution on the virtual plane.

In the next sections, the algorithm from 4.1 will be described in details. First, the initialization which is the set of operations that are done just once at the beginning of the simulation is presented, then the actual rescaling recycling done at each time step is explained.

4.2.1 Initialization

First all inlet nodes need to be found. These are the nodes on which the solution is sought. Then the normal to the inlet plane is calculated by taking the cross product of any two vectors formed by the first three vertices of an element lying on the inflow. This element is found by looping over boundary elements. Let denote the normal vector by its coordinates: x_{nrml}, y_{nrml} and z_{nrml}. From these quantities the equation of the plane is calculated by:

$$x_{nrml}x + y_{nrml}y + z_{nrml}z = a \tag{4.1}$$

Then the equation of the recycle plane is found by translating the inlet plane.

Next the blocking of the elements cut by the virtual recycle plane is performed using the following algorithm:

```
loop over all elements
   loop over the element's vertices
      calculate on which side of the recycle plane the vertex lies
   end loop over vertices
   if vertices of this element lie on both sides of the recycle plane
      store that element
   endif
end loop over elements
```

To properly apply SPEBC, it is needed to divide the instantaneous velocity at the recycle plane into a mean and a fluctuating part (eq. 3.1). As the recycle plane is virtual it does not have mesh vertices where the velocity solution is known. Thus, points on the virtual plane are needed to interpolate instantaneous velocity and to calculate the mean velocity components.

As the mean is calculated in time and space (spanwise or azimuthal averaging), first, points that will be used for spatial averaging need to be determined. The points where the mean velocity will be stored at each time step are called *fathers*. Fathers are virtual points located on one edge of the virtual plane. Typically, we will have more points in the boundary layer than in the free stream with more points closer to the wall surface as the mean velocity varies more in the boundary layer than outside. One way to determine these points is to use the normal coordinate from the inlet points that are located on one edge of the boundary that is normal to the flow. For each father, a predetermined number of points at the same normal coordinate spanning the whole spanwise or azimuthal domain are needed to average the velocity in the homogeneous direction. These points will be called *sons*. The solution from each son will be added to the father to calculate the spatial average that will be stored at this father. For all fathers and sons, the element from the virtual plane where the corresponding point lies is found and stored as well as its local coordinates.

The procedure described here is done once at the beginning of the simulation. Then at each time step the rescaling must be done.

4.2.2 Rescaling-recycling at each time step

The main SPEBC routine that generates the inflow velocity from a recycle plane for a boundary layer needs the nodal coordinates and the solution.

First the mean velocity field is calculated on the recycle plane. The solution field at all fathers and sons is interpolated from the solution field on the elements cutting the virtual plane. Then for each father, the averaged velocity field is calculated from its sons. As the mean field is also averaged in time, the spatial averaged field, $\langle \boldsymbol{Y} \rangle_z$, just calculated is added to a running time average from the previous time step using the following equation:

$$\langle \langle \boldsymbol{Y} \rangle_z \rangle_t^{n+1} = \frac{1}{\Delta_t} \langle \boldsymbol{Y} \rangle_z + \left(1 - \frac{1}{\Delta_t} \right) \langle \langle \boldsymbol{Y} \rangle_z \rangle_t^n \tag{4.2}$$

where $\langle\langle \boldsymbol{Y} \rangle_z \rangle_t^n$ is the mean field averaged in time and space at the previous time step and Δ_t is the window size for time averaging.

Once the mean velocity field of the virtual plane is known it is straightforward (though difficult to make numerically precise) to find the boundary layer thickness by locating the normal coordinate where the streamwise mean velocity reaches the free stream speed (minus ϵ, a small number). The boundary layer thickness at the inflow is fixed for the whole duration of the simulation. The other quantities needed are the momentum thickness (eq. 3.57), the friction velocity (eq. 3.46) and the boundary layer thickness derivative. The calculation for this last quantity is shown in section 4.5.3. Next for each vertex of the elements cutting the recycle plane, the mean velocity and the fluctuations are calculated. Then starting from the coordinates of the inlet points the corresponding coordinates are found on the recycle plane using equations (3.31-3.32). This is the point from which the velocity is rescaled using equations (3.49-3.54) for LWS rescaling and equations (3.113-3.120) for the alternative scaling by extracting the mean and fluctuating quantities from the solution at this point's corresponding element and local coordinates, and finally updating the solution at the corresponding inlet node.

4.2.3 Element search

The routine that searches in which element a given point lies takes as input the array of Cartesian coordinates, the connectivity array for elements that are cut by the virtual plane and the coordinates of the point of interest. It returns the element and the local coordinates of the given point. For background in the determination of the local coordinates from a given Cartesian point see pages 109-184 of [26].

The search method used here is a fast projection algorithm [30] where the domain of search (here the elements cut by the virtual plane) is divided into buckets. Buckets are structured rectangular domains that span the entire search domain. First the bucket containing the desired point is found quickly using the structured grid created by the buckets, thus reducing the search domain on the unstructured mesh to only the elements that are in the found bucket.

For the Cartesian domain the homogeneous direction is spanwise to the flow,

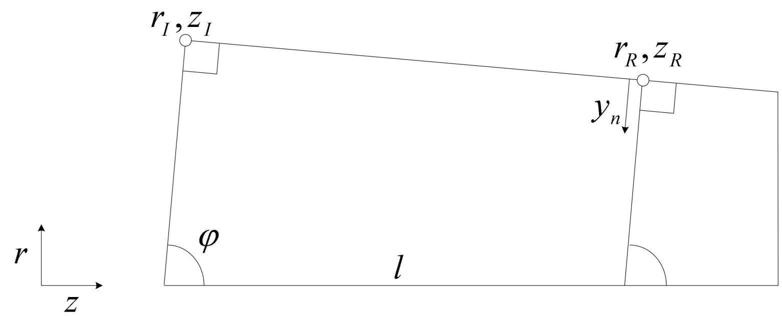

Figure 4.2: Schematic the axisymmetric domain used to implement axisymmetric SPEBC

but in the axisymmetric case the averaging is done azimuthally (e.g. at constant r and z). The next section will present the changes that arise from this added complexity.

4.3 Geometrical considerations for axisymmetrical problems

In this section, the specific case of axisymmetric domain is presented. When studying pipe or contracting nozzle flows the domain is axsisymmetric. Figure 4.2 shows the two-dimensional schematic of a contracting nozzle from the axis of symmetry to the contracting inner radius. The two important planes are shown: the inflow boundary and the internal recycle plane. These two planes are parallel, but they are not necessarily perpendicular to the axis of symmetry. In this case, the streamwise direction is denoted by z. As both planes are known, both the inner radius and the z location at the wall of the two planes are also known quantities (r_I and z_I for the inlet plane and r_R and z_R for the recycle plane). By convention, it was used $r = \sqrt{x^2 + y^2}$. As discussed in the previous section (4.2.1), the normal vector components to the inlet plane can be found. Thus the equations of the inflow and recycle planes are found using equation (4.1):

$$x_{nrml} r_I \cos\theta + y_{nrml} r_I \sin\theta + z_{nrml} z_I = a_I \tag{4.3}$$

$$x_{nrml} r_R \cos\theta + y_{nrml} r_R \sin\theta + z_{nrml} z_R = a_R \tag{4.4}$$

The angle between the two parallel planes and the axis of symmetry can be found by the following equation:

$$\tan\varphi = \frac{r_I}{z_I - \frac{a_I}{z_{nrml}}} \tag{4.5}$$

The similarity variables defined by equations (3.7) for y^+ and (3.14) for η need to be calculated with the off wall coordinate y_n instead of y. The off wall coordinate y_n is defined as follows:

$$y_n = \frac{r_w - r}{\sin\varphi} \tag{4.6}$$

where r_w is the inner radius of the nozzle at some plane parallel to the inflow boundary; for example, for the inlet plane $r_w = r_I$ and for the recycle plane $r_w = r_R$.

To calculate the velocity at the inlet plane for a point with r_{inl}, θ_{inl} and z_{inl} coordinates, first the off wall variable needs to be found using equation (4.6):

$$y_{n,inl} = \frac{r_I - r_{inl}}{\sin\varphi} \tag{4.7}$$

Using the appropriate scaling, the off wall coordinate at the recycle plane, $y_{n,rcy}$ can be found using equation (3.31 - 3.32) where y is replaced by y_n, from which the coordinate of the point on the recycle plane from which the solution is rescaled can be calculated:

$$r_{rcy} = r_R - y_{n,rcy}\sin\varphi \tag{4.8}$$

$$\theta_{rcy} = \theta_{inl} \tag{4.9}$$

$$z_{rcy} = \frac{a_R}{z_{nrml}} - r_{rcy}\left(\frac{x_{nrml}}{z_{nrml}}\cos\theta_{rcy} + \frac{y_{nrml}}{z_{nrml}}\sin\theta_{rcy}\right) \tag{4.10}$$

As the implementation uses the Cartesian coordinate system, this point is located at:

$$x_{rcy} = r_{rcy}\cos\theta_{rcy} \tag{4.11}$$

$$y_{rcy} = r_{rcy}\sin\theta_{rcy} \tag{4.12}$$

$$z_{rcy} = z_{rcy} \tag{4.13}$$

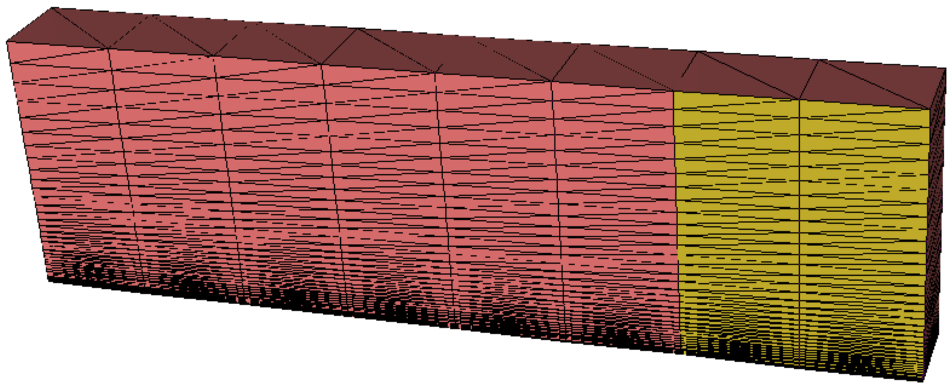

Figure 4.3: Sample structured mesh

4.4 SPEBC for structured grids

In the case of simple domains, it is common to employ structured meshes. Figure 4.3 shows a sample structured mesh. The recycle plane is situated at the interface between the red and yellow regions. In this case, both inlet and recycle planes have 2D structured meshes attached to it. In this section, the particular implementation that uses structured and 2D properties of the domain mesh will be presented, as this implementation is more accurate for this special case. Indeed, the solution is not interpolated at the recycle plane for the spatial averaging as the solution already exists.

Once the recycle plane is located, the father points used for spanwise averaging are mesh nodes located on one boundary edge with constant z (spanwise coordinate). As the 2D mesh is structured all the sons for a given father have the same z coordinate. Thus the spatial averaging calculation is straightforward as the solution is already known at each point of interest.

Furthermore, the mean and fluctuating flow quantities only need to be interpolated in the direction normal to the flow (y). In this case, we do not need to do element searching, but only simple 1D interpolations in y.

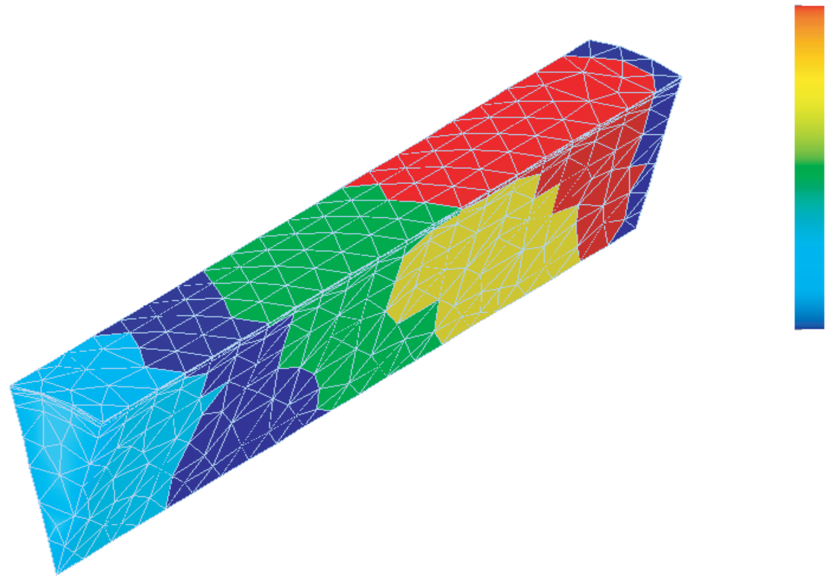

Figure 4.4: Partition mesh for a 5 processor case

4.5 Other considerations

4.5.1 Preprocessing for parallel simulations

As the domain of simulation is more and more complex and typical fluid dynamics meshes have several hundred thousand elements, the simulations are run on multiprocessor machines. This is also true for the current implementation of the SPEBC. To facilitate the SPEBC calculations the inlet elements and the elements that are cut by the virtual recycle plane are kept on the master processor. As such, the preprocessing software was modified to keep the elements that are cutting the virtual plane on the same processor as the inflow elements. Figure (4.4) shows the mesh partition used in a 5 processor simulation. The inflow is located at the right side of the domain. The master processor is shown in dark blue and it can be seen that the inflow elements and the elements cutting the recycle plane are located on it.

To do the proper mesh partition, the similar procedure as described in section 4.2.1 is used. Once the equation of the virtual plane is known, the elements that are cutting this virtual plane are found. To keep a balanced partition mesh, the

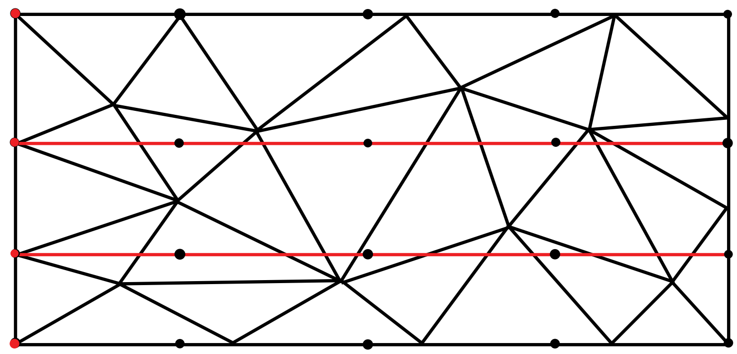

Figure 4.5: Father nodes, sons and averaging lines

number of elements on the master partition needs to be similar to the number of the elements on the other partitions even if this partition needs at least to contain both elements of the inlet plane and those cutting the virtual plane.

4.5.2 Flow variables averaging in one homogeneous direction for the whole domain

The homogeneous averaging, essential to rescaling recycling method, is also used for turbulence statistics computation. In isotropic turbulence, the homogeneous averaging is done in all three directions. In fully developed channel flow, the homogeneous averaging is done in two directions, i.e. streamwise and spanwise. For boundary layer flows, the homogeneity is in the spanwise direction. In this section only this last case will be discussed, but extending it to averaging in more spatial directions is straightforward. Thus the mean quantities are calculated by adding the averaging of the instantaneous quantities in the spanwise direction to the temporal average. In this section, the implementation of the homogeneous averaging for unstructured meshes will be presented.

Let `velbar` contain the mean quantities averaged in time and in the spanwise direction at the previous time step. The averaging using structured meshes is performed by averaging along lines in the homogeneous direction using mesh vertices that are located on these lines. The implementation for unstructured averaging is done by expanding on this procedure.

First the mesh points used for storing the averaged field need to be determined.

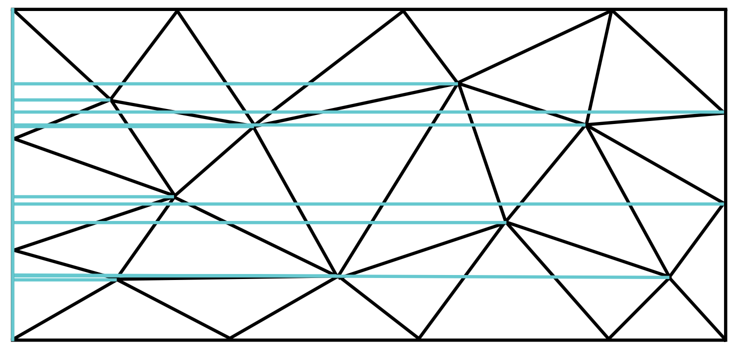

Figure 4.6: Eunuch nodes for each node of the mesh

For one homogeneous direction, these points called fathers are located on one of the two model faces that are perpendicular to the homogeneous direction. On the Figure 4.5 they are represented by the red dots. So for each of these points a predetermined number of points will be used to calculate the average in space. These new points called sons are located on imaginary lines in the homogeneous direction. On Figure 4.5 they are represented by the black dots.

Once the averaged field is calculated on each father, to compute the values of this field for a given mesh node, the field needs to be interpolated. For each node, first its projection on the averaging plane needs to be determined (see fig. 4.6). Then it is used for interpolation of the averaged field. The projection points are called *eunuchs* to differentiate them from the fathers.

In the next section the data structures needed for this procedure are presented, then they are extended for mesh partition in section 4.5.2.2.

4.5.2.1 Preprocessing the whole domain

In the arrays presented below, the notation is: the name of the array followed by, in parentheses, the size of each dimension.

`iavr(nfath):` global node number for each father.

`shpSons(nfath, nsons, nenl):` global shape functions evaluated at sons location for each virtual son for a given father.

`globSon(nfath, nsons, nenl)`: global node numbers attached to the corresponding shape function from `shpSons` for each virtual son for a given father.

`shpEunuchs(numnp, nenlb)`: global shape functions for a point located on the model face containing fathers (on Figure 4.6 this face is represented by the vertical blue line) which corresponds to each mesh vertex. For each vertex the horizontal blue line on Figure 4.6 connects the vertex point to his eunuch point.

`globEunuch(numnp, nenlb)`: global node numbers attached to the corresponding shape function from `shpEunuchs`.

In these array:

`nfath` is the number of fathers in the mesh which are located on one of the model faces that are perpendicular to the homogeneous direction.

`nsons` is the number of sons for each father. These points together with the corresponding father are used for averaging the desired quantities in the homogeneous direction. The son nodes are virtual nodes, they can coincide with a mesh vertex, but usually are not. On Figure 4.5 the red line represent the averaging lines for each father.

`nenl` is the number of nodes per element. For now the mean quantities are calculated using only linear shape functions.

`numnp` is the number of vertices in the mesh.

`nenlb` is the number of nodes per face of a boundary element.

4.5.2.2 Multiprocessor splitting

Figures 4.7 and 4.8 represent the case where we have two processors represented in two different colors.

In a multiprocessor case, the father nodes are generally on different processors. Also for each father the son nodes can also be on different processors (see fig. 4.7).

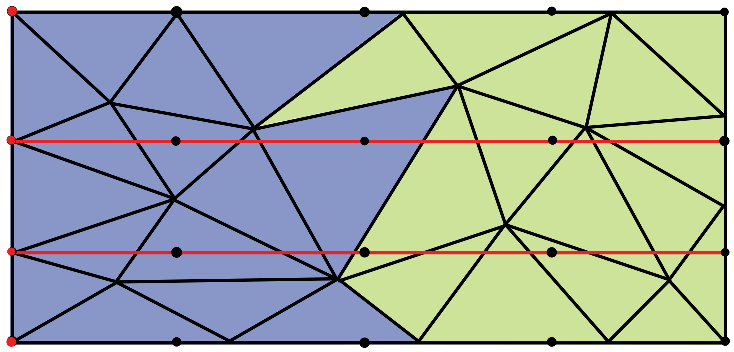

Figure 4.7: Father nodes, sons and averaging lines on each processor

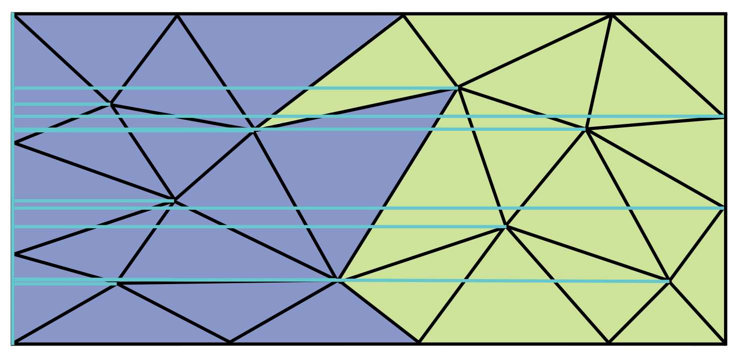

Figure 4.8: Eunuch nodes for each node of the mesh

And for most of the mesh vertices the corresponding eunuch is located on a different processor (see fig. 4.8). The following arrays are needed:

`fathproc(nfath):` processor number for each father.

`iavr(nfath):` global node number on given processor for each father.

`shpSons(nfath, nsons, nenl):` global shape functions evaluated at sons location for each virtual son on the given processor for a given father. If for a given father there are no sons on this processor put zeros.

`globSon(nfath, nsons, nenl):` global node numbers attached to the corresponding shape function from `shpSons` for each virtual son on the given processor for a given father. If for a given father there are no sons on this processor put zeros.

`shpEunuchs(numnp, nenlb)`: global shape functions for a point located on the model face containing fathers which corresponds to each mesh vertex on the master processor only.

`globEunuch(numnp, nenlb)`: global node numbers attached to the corresponding shape function from `shpEunuchs`.

`nfath` is the number of fathers in the mesh.

`nsons` is the number of sons for each father on a given processor.

`numnp` is the number of vertices on the master processor.

`nenlb` is the number of nodes per face of a boundary element.

4.5.2.3 Mean flow quantities calculation at each time step

These data structures are used to calculate `velbar` at each time step using the following procedure. First the mean values are calculated for each father.

$$\mathtt{velbarF}(\mathtt{fath}) = \frac{1}{\mathtt{nsons}} \sum_{i=1}^{\mathtt{nsons}} \sum_{j=1}^{\mathtt{nenl}} \mathtt{shpSons}\left(\mathtt{fath}, i, j\right) \cdot \boldsymbol{Y}\left(\mathtt{globSon}\left(\mathtt{fath}, i, j\right)\right) \tag{4.14}$$

where `velbarF` is the averaged field for each father, thus spanning through `nfath`.

Next the averaged field needs to be stored at each vertex of the mesh. This structure will be called `velbar` and is spanning through the total number of vertices in the mesh, `numnp`. It is calculated by the following equation:

$$\mathtt{velbar}(\mathtt{node}) = \sum_{i=1}^{\mathtt{nenlb}} \mathtt{shpEunuchs}\left(\mathtt{node}, i\right) \cdot \mathtt{velbarF}\left(\mathtt{iavr}\left(\mathtt{globEunuch}\left(\mathtt{node}, i\right)\right)\right) \tag{4.15}$$

4.5.3 Boundary layer thickness derivative calculation

Special emphasis is given to the calculation of the boundary layer thickness derivative, $\frac{d\delta}{dx}$, needed for eq. (3.121). The boundary layer thickness, δ, is the value of y coordinate where the mean streamwise velocity is 99% of the freestream velocity for a given x location from the averaged velocity field.

The boundary layer thickness derivative is calculated by assuming that δ varies linearly in an element and by doing a Taylor expansion around the x location where the derivative is needed, i.e. the recycle plane and the inlet plane. For a structured mesh with constant spacing in x direction, Δx, the inflow boundary layer thickness derivative is evaluated as follows:

$$\left(\frac{d\delta}{dx}\right)_{x=x_{inl}} = \frac{2}{\Delta x}\delta_{inl+1} - \frac{1}{2\Delta x}\delta_{inl+2} - \frac{3}{2\Delta x}\delta_{inl} \tag{4.16}$$

where δ_{inl+1} and δ_{inl+2} are the boundary layer thicknesses at the two x location following the inflow for the given mesh.

For the recycle plane, the boundary layer thickness derivative is obtained by:

$$\left(\frac{d\delta}{dx}\right)_{x=x_{rcy}} = \frac{1}{2\Delta x}\left(\delta_{rcy+1} - \delta_{rcy-1}\right) \tag{4.17}$$

where δ_{rcy-1} and δ_{rcy+1} are the boundary layer thicknesses at the x location respectively preceding and following the recycle plane for the given mesh.

CHAPTER 5
RESULTS AND DISCUSSION

Before studying turbulent flows that are 3D and transient, and therefore expensive, the unstructured grid implementation of the SPEBC boundary condition was carried out on laminar flow. In section 5.1.1, a brief description of the scaling required is given. In section 5.2, the results from the turbulent boundary layer with zero pressure gradient simulations are presented using the Lund, Wu and Squires and the alternative scalings which are then compared to experimental results.

5.1 Laminar flat plate boundary layer flow

To implement and test the SPEBC, the simple case of laminar boundary layer over a flat plate was studied. The simulation was performed on a structured mesh (fig. 5.1) of 1728 tetrahedral elements (9 by 37 by 2 nodes). In the y-direction, the mesh is finer close to the wall (plate) and coarser away from it; the element's height grows similarly to the boundary layer growth. Only one layer of elements exists in the z-direction. The boundary conditions for this simulation were:

- the bottom surface is a solid wall and therefore a no-slip condition and fixed

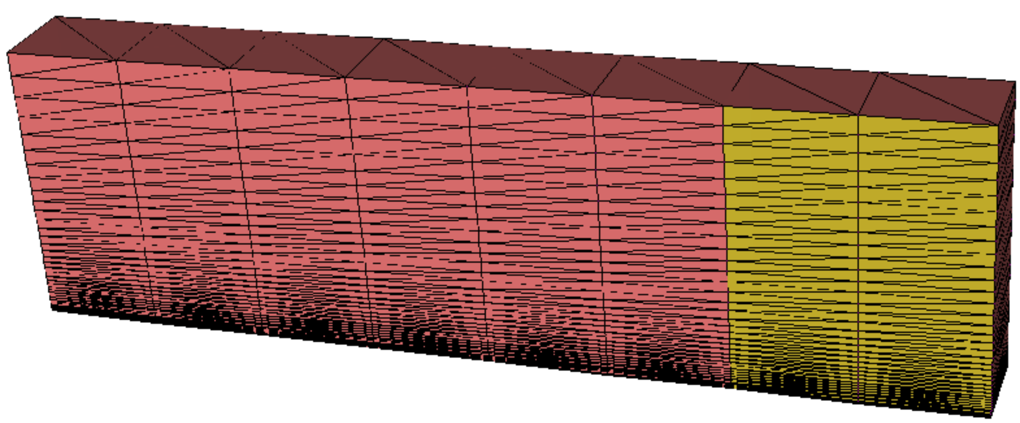

Figure 5.1: Laminar flat plate mesh with inflow on left and the interface between the two colors showing the recycle plane.

temperature (nondimensional temperature $T = 0.0625$) was applied. The temperature is needed when PHASTA is run in compressible mode;

- on the inflow only the SPEBC was set;
- on the side surfaces there was no z-component of velocity to simulate a 2D simulation on this 3D mesh;
- on the top surface and the outflow, an ambient pressure was applied (Dirichlet with a value of $P_\infty = 18.0212$ for the compressible code and Neumann with a value of $P_\infty = 0$ for the incompressible code).

As part of the SPEBC boundary condition, the inlet boundary layer thickness was maintained at $\delta_{inl} = 0.0074m$ and the recycle plane was located $0.0555m$ (or 7.5 boundary layer thicknesses) downstream from the inflow. As the problem is stationary, at each time step the solution converges closer to the stationary state. The initial condition on velocity was the following streamwise profile which gives the 1/3 law inside the boundary layer and unity outside:

$$u = \min\left(1.0, \left(\frac{y}{\delta}\right)^{1/3}\right) \tag{5.1}$$

In y and z directions the velocity was null. The initial pressure and temperature have been kept constant to the values given above.

In this section it will be shown that the unstructured implementation gives as good a solution as the structured implementation.

5.1.1 The SPEBC for Laminar Flows

Analytically, an approximate solution for the flat plate boundary layer was found by Blasius using a similarity solution [5]. Starting from incompressible boundary layer equations:

$$u\frac{\partial u}{\partial x} + v\frac{\partial u}{\partial y} = \nu\frac{\partial^2 u}{\partial y^2} \tag{5.2}$$

$$\frac{\partial u}{\partial x} + \frac{\partial v}{\partial y} = 0 \tag{5.3}$$

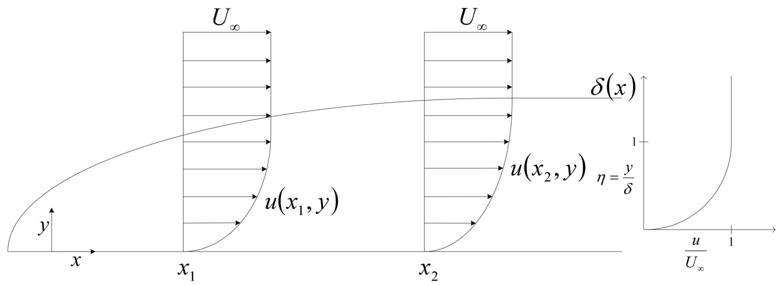

Figure 5.2: Schematic of x-component velocity profiles for a laminar flat plate boundary layer

with the boundary conditions $u(x, 0) = v(x, 0)$ and $u(x, \infty) = U_\infty$. Using the following similarity variable:

$$\eta = \frac{y}{\delta} \tag{5.4}$$

$$\delta(x) = \sqrt{\frac{2\nu x}{U_\infty}} \tag{5.5}$$

and the x-direction velocity of the following form:

$$u = U_\infty f'(\eta) \tag{5.6}$$

the boundary layer equations (5.2)-(5.3) become what is known as Blasius equation:

$$f''' + f f'' = 0 \tag{5.7}$$

with its boundary conditions: $f(0) = f'(0)$ and $f'(\infty) = 1$. Figure (5.2) represent the schematic of the boundary layer on a flat plate with the x-component velocity profiles at two different locations as well as the collapsed profile of the x-component dimensionless velocity as a function of the similarity variable, η.

In the SPEBC using the Blasius approximation, the solution at the inlet plane can be extracted from the recycle plane by the following equation:

$$u_{inl}(y) = u_{rcy}\left(\frac{\delta_{inl}}{\delta_{rcy}} y\right) \tag{5.8}$$

where u_{inl} is the solution inside the boundary layer of inlet plane, u_{rcy} is the known

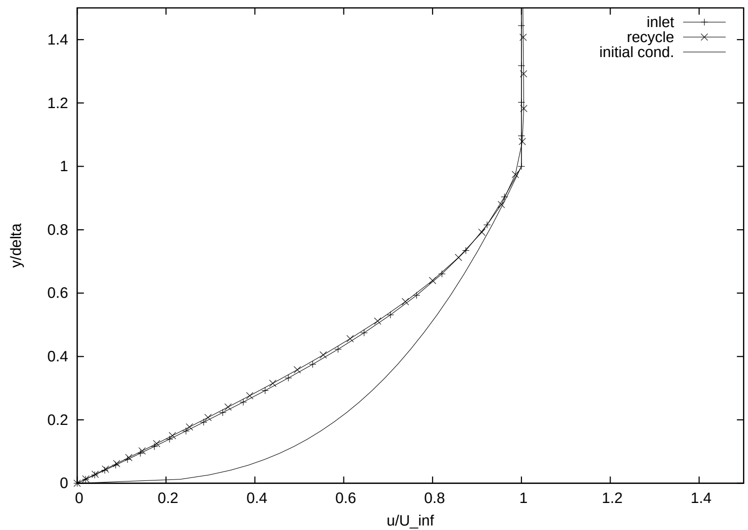

Figure 5.3: Dimensionless streamwise velocity profile inside the laminar flat plate boundary layer

solution at some position inside the boundary layer at the recycle plane, and δ_{inl} and δ_{rcy} are the boundary layer thicknesses at the inlet and recycle positions respectively.

For each point $(x, y, z)_{inl}$ of the inflow plane the solution is computed from the solution extracted at the following corresponding point on the virtual plane:

$$(x, y, z)_{rcy} = (x_{rcy}, \frac{\delta_{inl}}{\delta_{rcy}} y_{inl}, z_{inl}) \tag{5.9}$$

by interpolating the solution from the neighboring nodal points' solutions. In the structured simulation the neighboring points are all located on the two-dimensional model plane that is used for recycling. In the unstructured case the recycle plane is virtual, so the neighboring mesh points are not necessarily located on a 2D plane.

5.1.2 Verification of the unstructured implementation of the SPEBC

Figure (5.3) shows the streamwise velocity solution obtained by the unstructured simulation for this laminar flat plate boundary layer. The solution was obtained after 500 time steps with a $\Delta t = 0.02$. Also shown is the initial condition on streamwise velocity which is the 1/3 law. The initial residual on the solution was 10^{-7} and the solution converged at the end of the simulation to 10^{-11}.

Figure (5.4) shows the streamwise velocity profile at the end of the simulation.

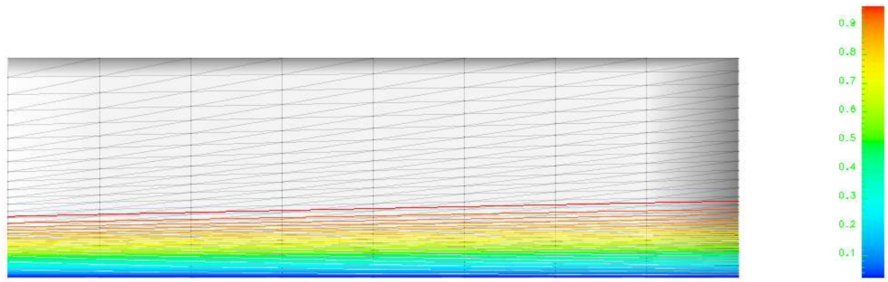

Figure 5.4: Streamwise velocity profile for laminar flat plate boundary layer

The velocity is zero at the wall and equal to one outside the boundary layer. The boundary layer is laminar as there is no fluctuations in the streamwise component of the velocity shown.

The solution obtained by the unstructured simulation of the laminar flat plate boundary layer was compared to the solution obtained from the same mesh but with the structured implementation of the SPEBC which needs the same number of points on the inflow and recycle planes. Figure (5.5) shows the solutions at both inflow and recycle planes for both simulations. Both simulations give same streamwise velocity profiles. Inside the boundary layer the structured implementation gives a solution that is a bit lower than the unstructured implementation's solution as seen in the insert of figure (5.5). This difference is due to the fact that the interpolation is not done at the same location. In the structured case the velocity solution is interpolated from the known data (velocity solution on the recycle plane) and in the unstructured case the interpolation is done when calculating the averaged velocity field.

The next verification that was done was that the solution obtained using the compressible code is the same as the solution obtained by the incompressible code. As the compressible code can also solve the incompressible problem the necessary modifications were done to the boundary and initial conditions and to the input file. The figure (5.6) shows the streamwise velocity solution obtained by both compressible and incompressible code for the unstructured implementation. The same mesh was used in both cases. It can be seen that the solutions obtained by both simula-

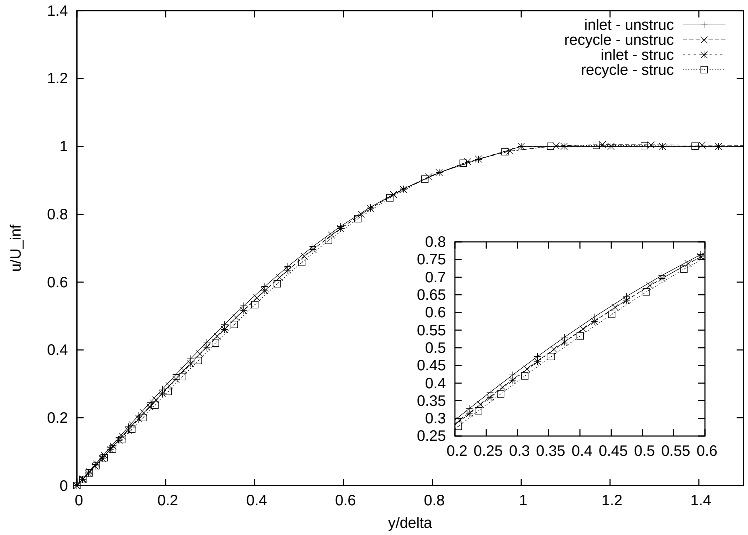

Figure 5.5: Dimensionless streamwise velocity profile for laminar flat plate boundary layer as a function of dimensionless normal variable η computed by structured and unstructured simulations

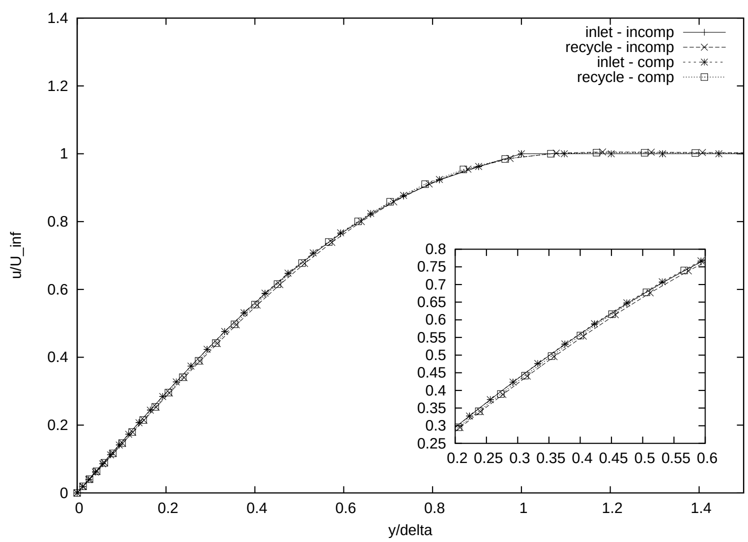

Figure 5.6: Dimensionless streamwise velocity profile for laminar flat plate boundary layer as a function of dimensionless normal variable η computed by incompressible and compressible simulations

tions coincide; the velocity profiles at inflow and recycle planes collapse as expected. In the insert of figure (5.6), small variations in the solution inside the boundary layer are shown which are due to the different solvers used in these two cases, but the variations are smaller than between the solutions shown in the previous figure (Fig. 5.5) when comparing the structured and unstructured implementations.

The main goal of the unstructured implementation of the SPEBC is the capability to use any virtual plane as the recycle plane. So in the next two figures (5.7 and 5.8) the solutions from simulations using two virtual planes are compared. Both simulations were done using the unstructured implementation in the incompressible code. In the first case the virtual plane is the existing 2D model plane located at $x_{rcy} = 0.2035m$ and in the second simulation the recycle plane was moved a bit forward ($x_{rcy} = 0.203m$). In this second case the recycle plane is truly virtual, but the two plane are located close enough to have nearly the same solutions.

Figure (5.7) shows the streamwise velocity profile at the inlet for the two simulations. The profiles nearly collapse together. Only in the insert, can a discrepancy be seen. As the recycle plane is not the same in the two cases, the inlet profiles which are calculated from the recycle planes do not completely collapse. Figure (5.8) shows the streamwise velocity profiles at $x = 0.2035m$ which is the recycle plane only in one case. Here the collapse is even more complete than for the inlet plane, as it should be.

With this simple problem, several aspects of the unstructured implementation of the SPEBC was verified by comparing the solution obtained to the solution from the structured implementation. Also both incompressible and compressible codes were tested.

5.2 Turbulent flat plate boundary layer flow

5.2.1 Boundary and initial conditions

For the simulation of the turbulent boundary layer over a flat plate with zero pressure gradient the domain size chosen is $10\delta_{inl}$, $3\delta_{inl}$ and $\frac{\pi}{2}\delta_{inl}$ in the streamwise, normal and spanwise directions respectively. The distance $3\delta_{inl}$ in the direction normal to the wall is enough outside the boundary layer such that the flow variables

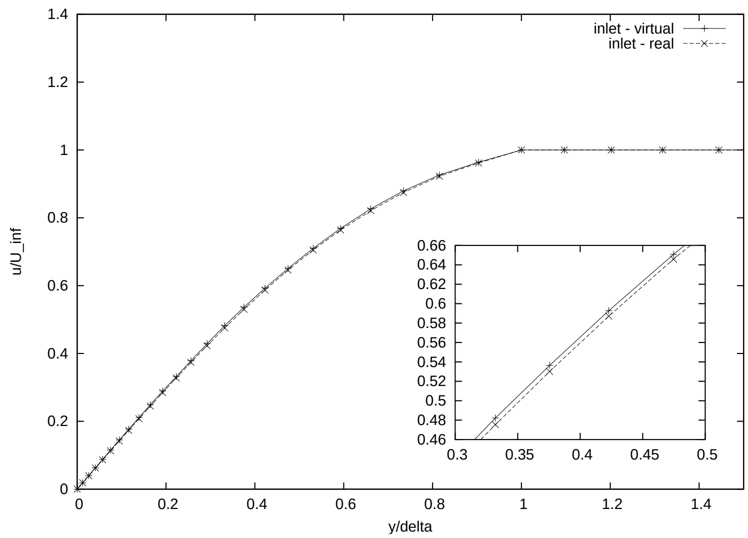

Figure 5.7: Dimensionless streamwise inflow velocity profile for laminar flat plate boundary layer as a function of dimensionless normal variable η computed by unstructured incompressible simulations for two recycle planes: $x_{rcy} = 0.2035m$ and $x_{rcy} = 0.203m$

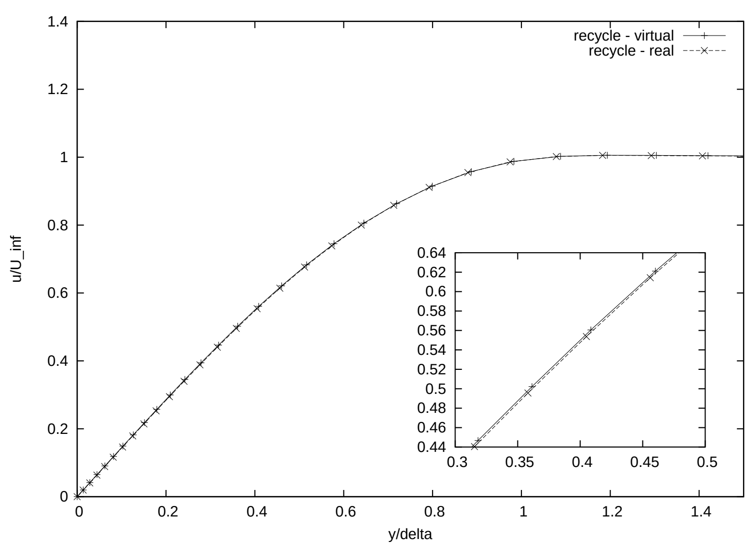

Figure 5.8: Dimensionless streamwise velocity profile for laminar flat plate boundary layer at $x = 0.2035m$ as a function of dimensionless normal variable η computed by unstructured incompressible simulations for two recycle planes: $x_{rcy} = 0.2035m$ and $x_{rcy} = 0.203m$

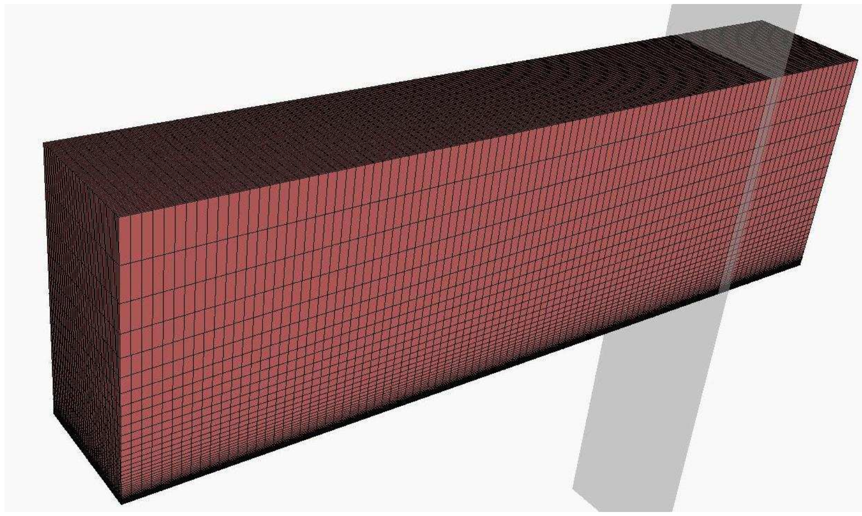

Figure 5.9: Hexahedral mesh with 100 $\times$ 45 $\times$ 64 points

in the free stream are independent of the turbulence from the boundary layer at the top boundary of the domain; $10\delta_{inl}$ in the streamwise direction is chosen as it is sufficient distance between the inlet and the outlet to have a good sized region in the computational domain to study the turbulence statistics without numerical interference from the inlet or the outlet; and $\frac{\pi}{2}\delta_{inl}$ in the spanwise direction assures that the two-points turbulence statistics are decorrelated between the two sides as periodic boundary conditions are imposed in this direction to simulate an infinite flat plate in the spanwise direction, so the mean flow is two-dimensional.

This domain was meshed using linear hexahedral elements with 100, 45 and 64 points in the streamwise, normal and spanwise directions respectively, which gives a structured mesh of 274428 elements shown in Figure 5.9. In the normal direction the mesh is finer at the wall and grows with the boundary layer (fig. 5.9). The first point of the wall is located in the viscous sublayer with $\Delta y^+ = 1$. The element spacing in streamwise direction is $\Delta x^+ = 65$ and in spanwise direction is $\Delta z^+ = 15$. In the figure the recycle plane is also shown at $7\delta_{inl}$ from the inlet. This distance was chosen because it is sufficiently far from the inlet for the two-points correlation tensor to be decorrelated between these two locations.

and no mass flux. At the outflow and the top surface the natural pressure was set to zero. The SPEBC is imposed at the inflow with the boundary layer thickness at the inlet $\delta_{inl} = 0.21m$.

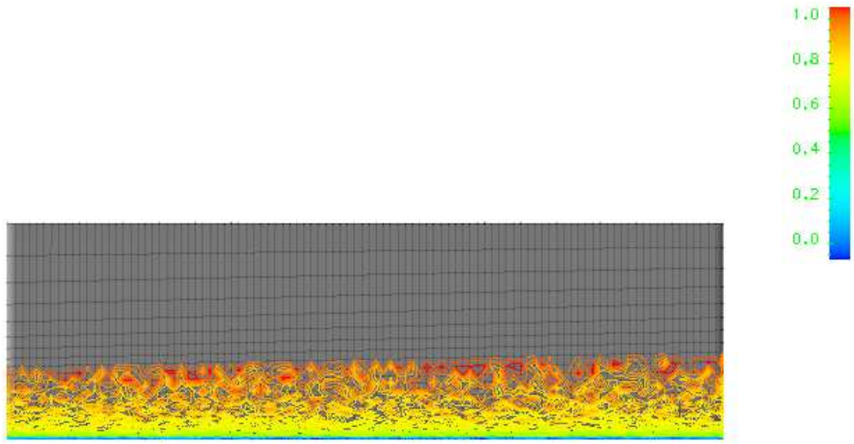

Figure 5.10: Streamwise velocity initial condition using 1/7 power law and random fluctuations

For the initial condition, a varying streamwise velocity is input using the following functions:

$$u(x,y) = \begin{cases} 1 & y > f(x) \\ \min(g(x,y), h(x,y)) + \chi & y < f(x) \end{cases} \tag{5.10}$$

where $f(x)$, $g(x,y)$, $h(x,y)$ and χ are given by

$$\begin{aligned} f(x) &= 0.365x^{0.8}\nu^{0.2} && (5.11) \\ g(x,y) &= \left[\frac{y}{f(x)}\right]^{1/7} && (5.12) \\ h(x,y) &= \frac{0.0288}{\nu} y \left(\frac{x}{\nu}\right)^{0.2} && (5.13) \\ \chi &= 0.2\,(0.5 - \text{random}(t)) && (5.14) \end{aligned}$$

In these equations ν is the kinematic viscosity, $\nu = 1.48 \cdot 10^{-5} \frac{m^2}{s}$. Figure 5.10 shows this initial conditions where the fluctuations are random numbers.

All the simulations in this section have a time step size of $\Delta t = 1.0 \cdot 10^{-2} s$ which is approximatively $\frac{\delta_{inl}/U_{\infty}}{20}$ and $CFL = \frac{\Delta t U_{\infty}}{\Delta x}$ of 0.5. This problem was simulated using incompressible LES.

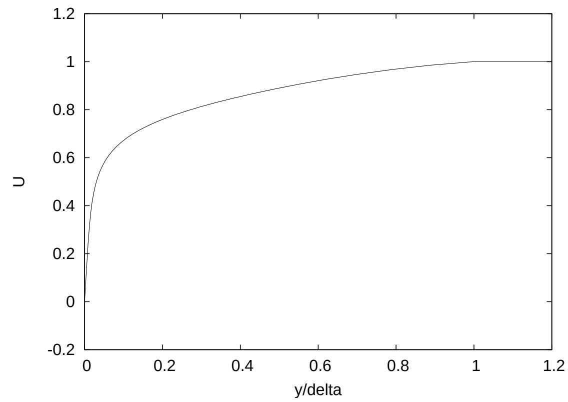

Figure 5.11: Spalding profile fixed at the inlet for early transient

5.2.1.1 Initiating the simulations

If the simulation is run using only the initial conditions described above, the physical fluctuations would not be easily obtained as both the mean and fluctuations are rescaled at the inlet. There is nothing to drive the flow. To remedy that, a given mean profile is fixed at the inlet which helps sustain the turbulent flow through the transient and to achieve fluctuations that correctly represent the boundary layer. Once the flow characteristics (boundary layer thickness, momentum thickness, friction velocity) are stabilized the simulation is transitioned to a case where the mean profile at the inlet is also recycled (e.g., the SPEBC boundary condition is fully applied). The profile that was used in our case is shown in the Figure 5.11 and it is calculated from the Spalding equation [55]:

$$y^+ = u^+ + e^{-\kappa B}\left[e^{-\kappa u^+} - 1 - \kappa u^+ - \frac{(\kappa u^+)^2}{2} - \frac{(\kappa u^+)^3}{6}\right] \tag{5.15}$$

to which the following wake function was added [11]:

$$u^+ = \frac{1}{\kappa}\ln(y^+) + B + A\sin^2\left(\frac{\pi}{2}\eta\right) \tag{5.16}$$

where $\kappa = 0.4$, $B = 5.5$ and $A = 2.5$.

Figure 5.12 show the temporal variation of the boundary layer thickness at the recycle plane and the friction velocity, respectively. On Figure 5.12(b) the upper curve is the friction velocity at inlet plane and the other is at the recycle plane.

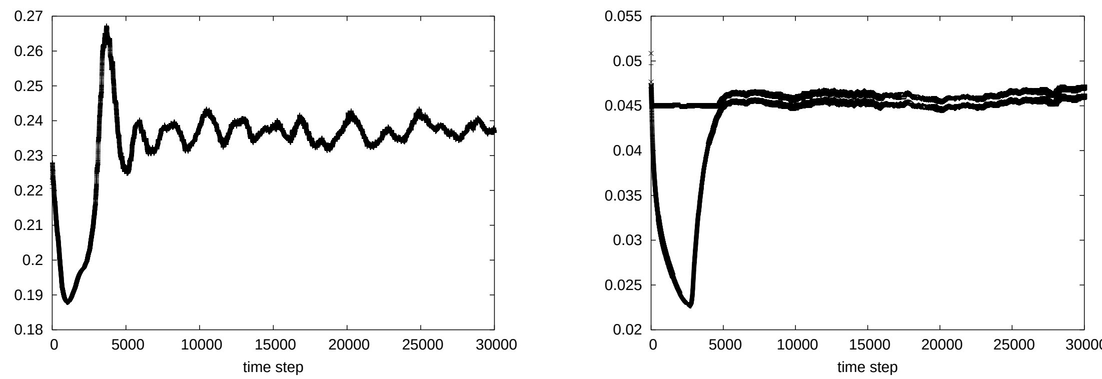

(a) δ_{rcy} (b) u_τ

Figure 5.12: Temporal evolution of (a) Recycle plane's boundary layer thickness, and (b) Friction velocity at the inlet (upper) and recycle (lower) planes

During the early transient to speed up the process of developing good turbulence, the friction velocity was fixed to $u_{\tau,inl} = 0.0456\frac{m}{s}$.

The Spalding inlet profile is kept fixed for the first 4000 time steps and then gently transitioned to recycling the inlet until 5000 time steps, at which point the simulation does not depend on user inputed profile. A statistically stabilized flow is attained after 24 domain flow-throughs. In the next section the results will be presented that are obtained from this simulation where the turbulence statistics were calculated over 20000 time steps (from 10000 to 30000 time steps) which runs for $t = 950\frac{\delta_{inl}}{U_\infty}$.

5.2.2 Solution with LWS scaling

Figure 5.13 shows the instantaneous streamwise velocity field at the end of the simulation. The stretched vortices in the streamwise direction can clearly be seen that are expected in turbulent boundary layers with a steep velocity gradient in the direction normal to the wall. The streamwise fluctuations are shown in Figure 5.14 at the inflow and recycle planes. It can be seen that the same fluctuation structures are present on the both planes as the fluctuation on the inflow is rescaled from the other plane.

The mean streamwise velocity profiles are shown in Figure 5.15 in outer vari-

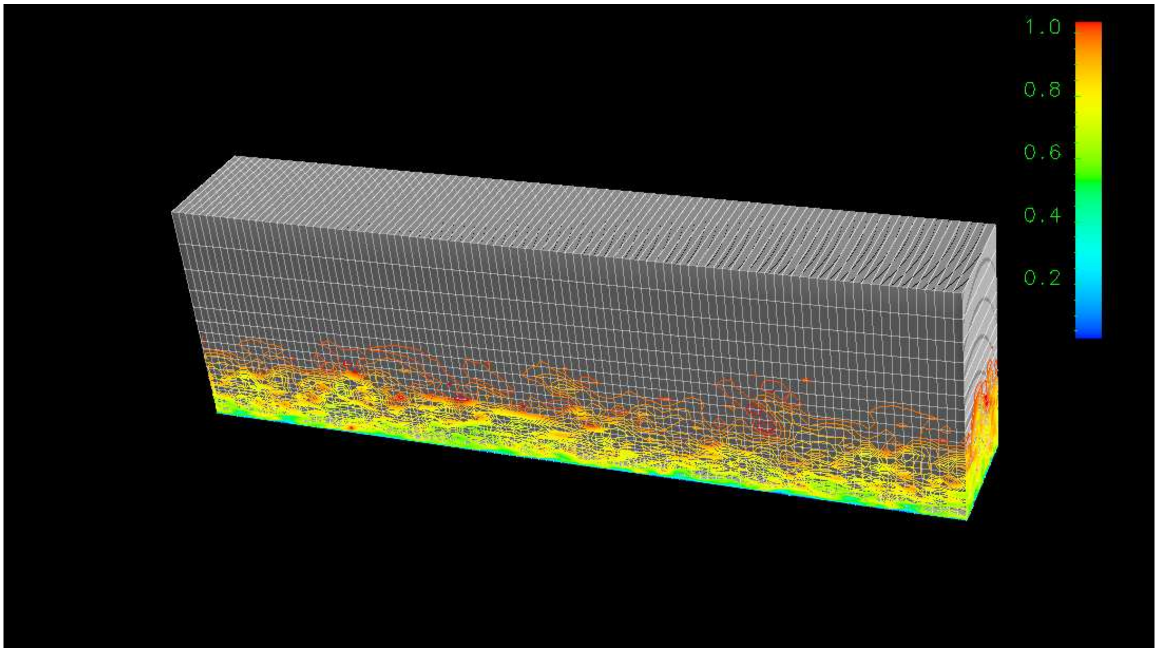

Figure 5.13: Streamwise velocity field

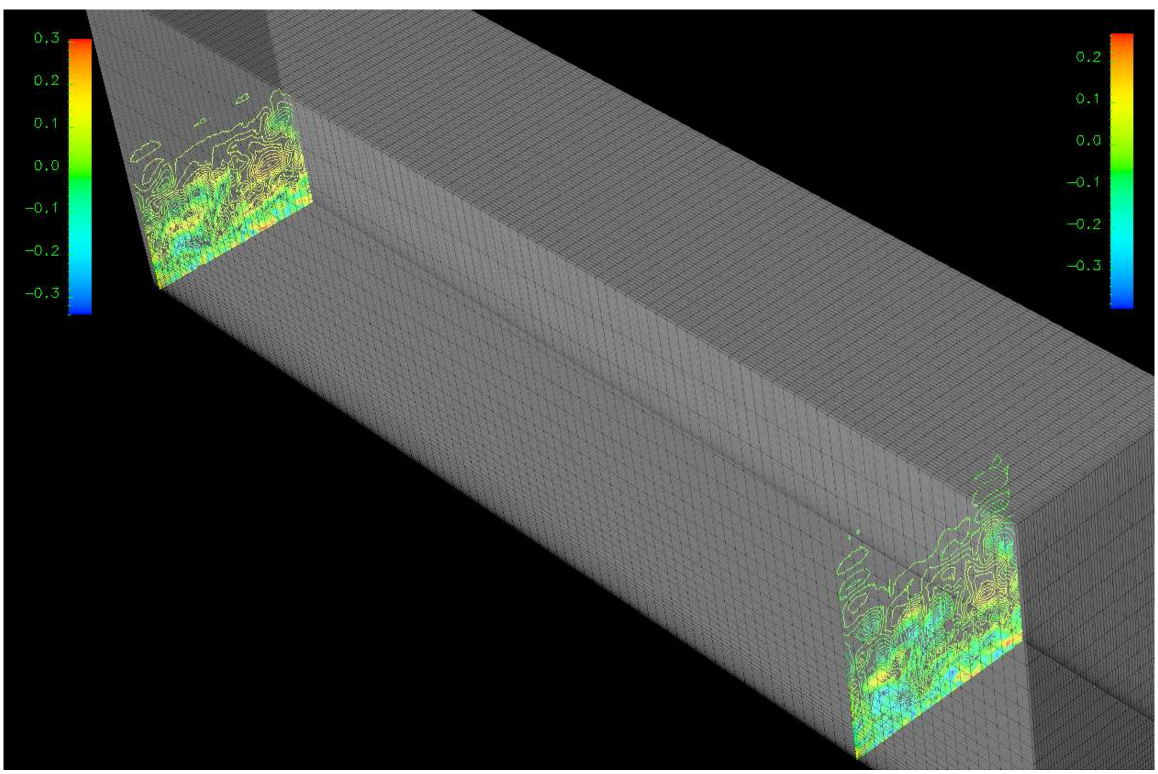

Figure 5.14: Streamwise velocity fluctuations at inlet and recycle planes

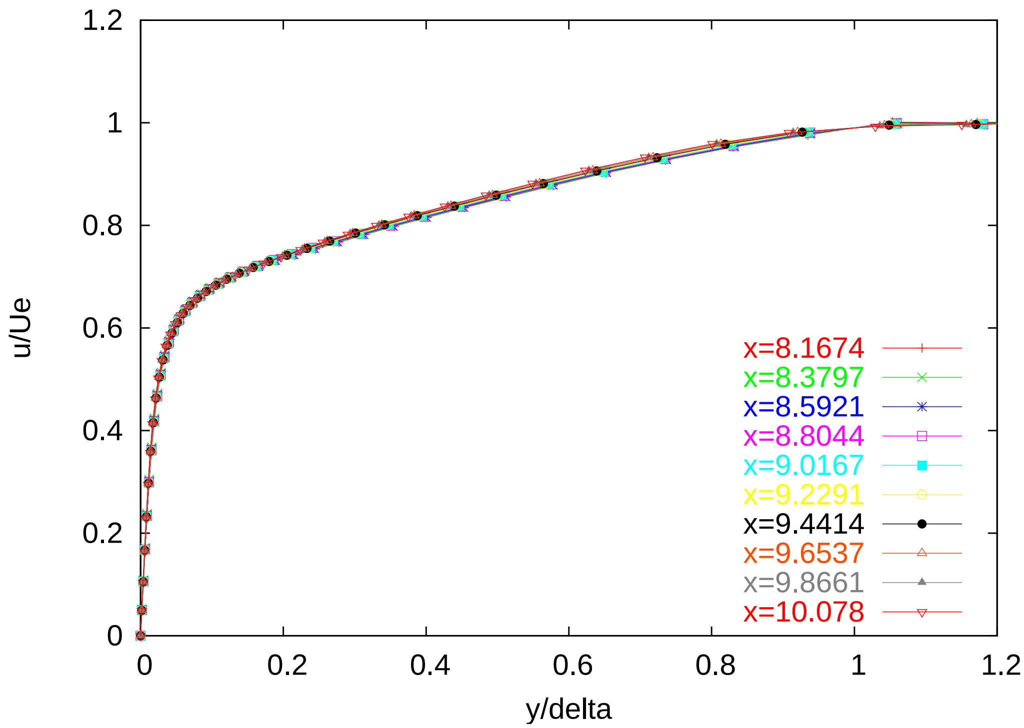

Figure 5.15: Mean streamwise velocity profiles at 10 different x locations in outer variables

ables and in Figure 5.16 in inner variables at 10 different streamwise locations. It can be seen on Figure 5.15 that all the profiles collapse together to the same curve when using outer region scaling ($\frac{U}{U_\infty}$ vs. η) which is expected from the turbulent boundary layer theory. Figure 5.16 shows the same velocities using the inner region scaling: u^+ as a function of y^+ in a semi log scale. From the classical turbulent boundary layer theory, in the viscous sublayer the velocity profile is linear, i.e. $u^+ = y^+$ and in the outer layer it is logarithmic:

$$u^+ = \frac{1}{\kappa} \ln y^+ + B \tag{5.17}$$

with $\kappa = 0.41$ and $B = 5.0$. We see that the profiles follow these two functions appropriately. In this figure, the wake region is apparent when the velocity profile rises slightly from the line representing equation (5.17).

Figure 5.17 shows the Reynolds stress tensor components, u_{rms}, v_{rms} and w_{rms} and $\overline{u'v'}$ normalized by the local friction velocity, u_τ. The root-mean square is

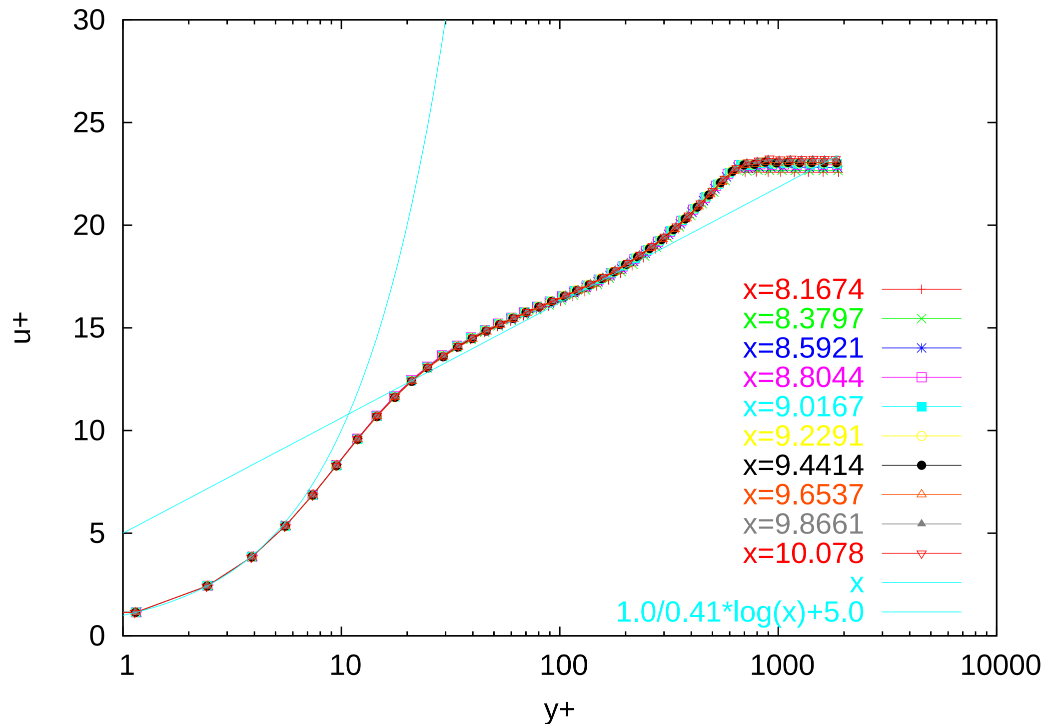

Figure 5.16: Mean streamwise velocity profiles at 10 different x locations in inner variables

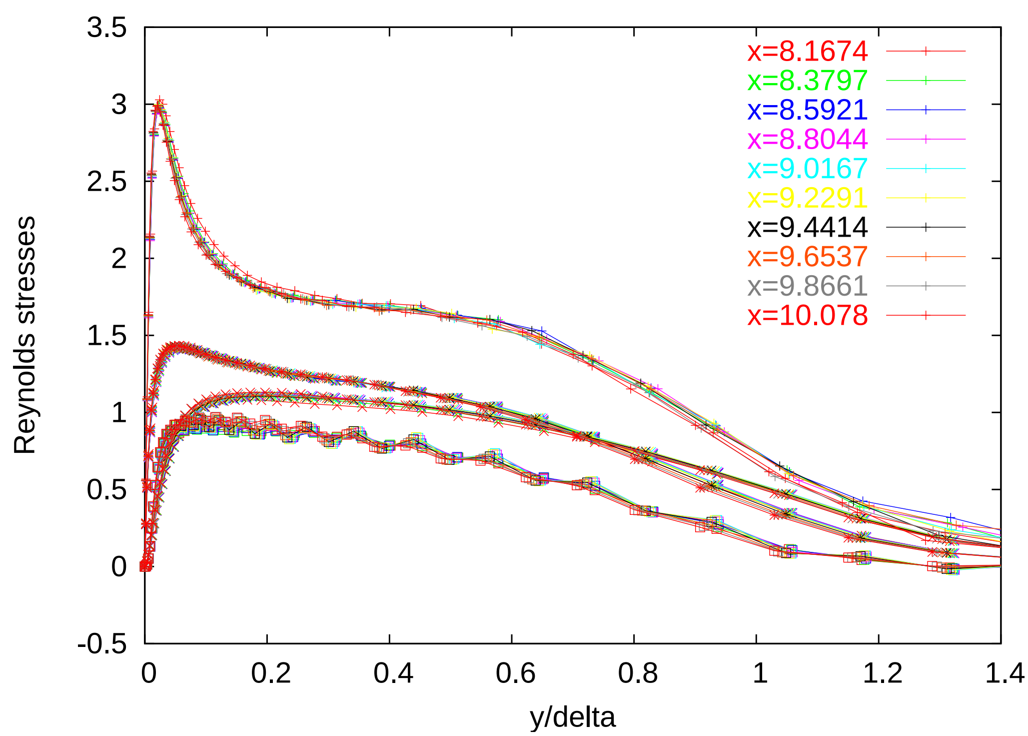

Figure 5.17: Reynolds stresses profiles at 10 different x locations

defined as follows:

$$u_{rms} = \sqrt{\overline{u'^2}} \tag{5.18}$$

As expected from turbulent boundary layer theory, the fluctuations are largest in the inner layer and the streamwise component contains the most turbulence as it is less influenced by the presence of the wall. The v_{rms} is the least turbulent of normal stresses and the peek turbulence is achieved further from the wall. The three normal components of the Reynolds stress tensor do not vanish in the free stream due to the intermittency of the turbulent boundary layer, but the shear stress does which means that the flow is more isotropic in the wake region.

On Figure 5.17, the Reynolds shear stress profile is oscillating about its expected value which means that the simulation did not completely converge yet as the shear stress is the last to converge.

In the next section, the need for correctly including the turbulent boundary layer intermittency in the simulation is discussed. In section 5.2.2.2 the solution obtained using the hexahedral mesh is compared to the solution obtained with the tetrahedral mesh. Finally, in section 5.2.2.3 the solutions obtained with Lund, Wu and Squires and the alternative scalings are compared.

5.2.2.1 Fluctuation scaling outside the boundary layer thickness

As the fluctuation scalings are used only in the boundary layer, if nothing is done outside there is a sharp change in the fluctuations if they are to vanish in the free stream flow. This sharp interface is shown in the Figure 5.18: the green profiles have a sharp change in the slope of the streamwise mean velocity at $\eta = 1$ (see the insert).

In the rescaling recycling method the boundary layer thickness at the inflow is kept fixed. This value is the statistical mean of δ, but instantaneously the turbulent boundary layer fluctuates a lot. The free stream laminar flow dips fractally inside the turbulent boundary layer. This is the intermittency of the turbulent boundary layer. From the data of Klebanoff [32, 64] it was found that the intermittency factor, which is the ratio of the instantaneous boundary layer thickness to the mean boundary layer thickness, varies from 0.4 to 1.2. The instantaneous boundary layer

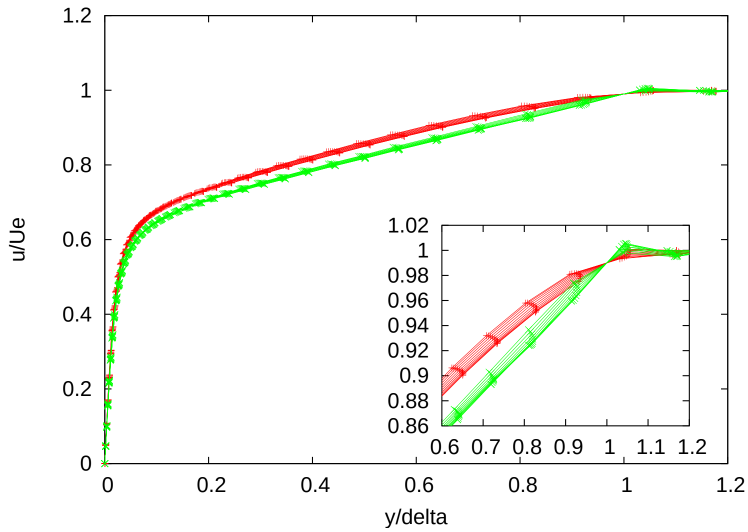

Figure 5.18: Normalized streamwise mean velocity with (red) and without (green) fluctuations rescaling in the free stream

variation is captured in the simulation by the fluctuations. Even if the fluctuations are only cropped at the inflow when rescaled, the sharp interface is propagated through the flow.

To smoothly transition the mean velocity from inside the boundary layer to the free stream flow, the fluctuation must be rescaled even outside of the boundary layer, but keeping the rescaling of the fluctuations outside of the boundary layer up to the top boundary of the domain makes the simulation unstable. The fluctuation at the inflow boundary is let to vanish smoothly outside of the turbulent boundary layer using the smooth Heaviside function defined as [57] (see Figure 5.19):

$$H_\epsilon(\phi) = \begin{cases} 1 & \text{if } \phi < -\epsilon, \\ \frac{1}{2}\left[1 - \frac{\phi}{\epsilon} - \frac{1}{\pi} sin(\frac{\pi\phi}{\epsilon})\right] & \text{if } |\phi| \leq \epsilon, \\ 0 & \text{if } \phi > \epsilon. \end{cases} \tag{5.19}$$

where $\phi = y - 1.2\delta_{inl} - \epsilon$ is the distance outside the boundary layer. With this smoothing function, the fluctuation is rescaled completely to $1.2\delta_{inl}$ then smoothly transitioned to zero over a region of 2ϵ where ϵ is chosen such that it spans 2 or 3 elements in the normal direction (in this simulation $\epsilon = \frac{\delta_{inl}}{4}$). In Figure 5.18, the

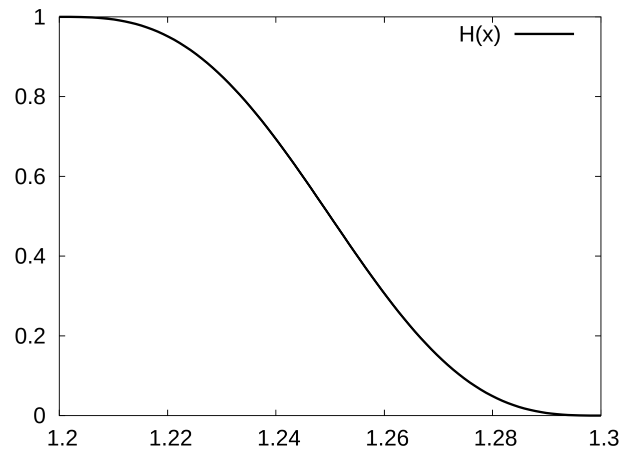

Figure 5.19: Heaviside function

streamwise velocity profiles for the simulation using the Heaviside function is shown in red. When the fluctuation is also rescaled outside of the boundary layer, the velocity profile is more rounded in the outer region of the boundary layer than the green profile.

5.2.2.2 Mesh topology influence

The hexahedral mesh was divided into a tetrahedral mesh with same number of vertices by dividing each hexahedral element into six tetrahedral elements.

On Figure 5.20, the boundary layer thickness and the friction velocity obtained on both meshes are shown as functions of streamwise location. The boundary layer thickness for the hex mesh varies mostly linearly in the computational domain, but that obtained from the tet mesh starts curving up, but then asymptotes with the same slope as that from the hex mesh. Both curves start from the same location as the inflow boundary layer was fixed.

On Figure 5.20(b), the friction velocity is shown where the curve marked theory is given by the equation:

$$\frac{u_\tau}{U_\infty} = \sqrt{\frac{1}{2} \cdot \frac{0.058}{Re_x^{1/5}}} \tag{5.20}$$

This is the power law given by Prandtl in 1927 [43] which the Lund, Wu and Squire scaling uses for calculating the friction velocity from the momentum thickness. Both

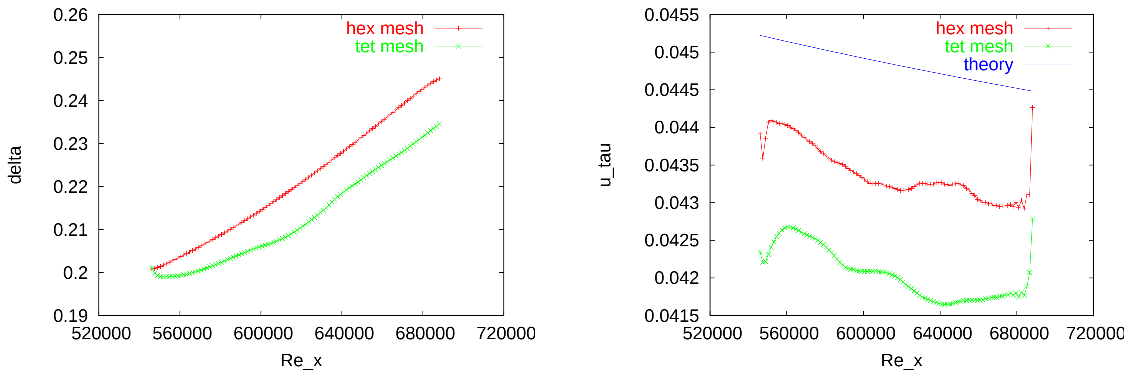

(a) Boundary layer thickness (b) Friction velocity

Figure 5.20: Boundary layer thickness (a) and friction velocity (b) as a function of streamwise location for the whole simulation domain for hexahedral (red curves) and tetrahedral (green curves) meshes

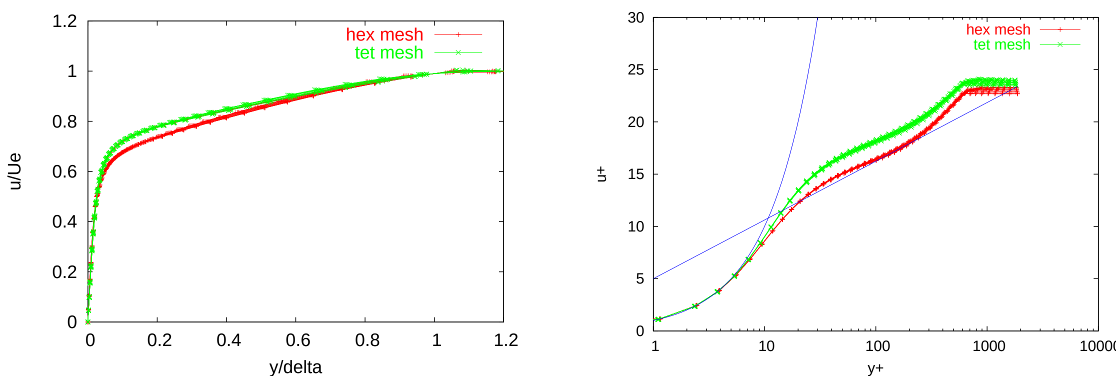

(a) $\frac{U}{U_\infty}$ vs. η (b) u^+ vs. y^+

Figure 5.21: Mean streamwise flow profile obtained on hexahedral and tetrahedral meshes

friction velocity curves have the same slope as equation (5.20), but the friction velocity from the tetrahedral mesh is 3% lower than that from the hexahedral mesh. The friction velocity is calculated by equation (3.46) using the slope of the velocity at the wall as the first point of the wall is inside the viscous sublayer. The friction velocity curves have jumps at the inflow and outflow locations where the friction velocity is incorrect due to the numerical errors in the stress computation (post-processing) from these two locations.

Figure 5.21 shows the mean streamwise velocity profiles in inner (5.21(b))

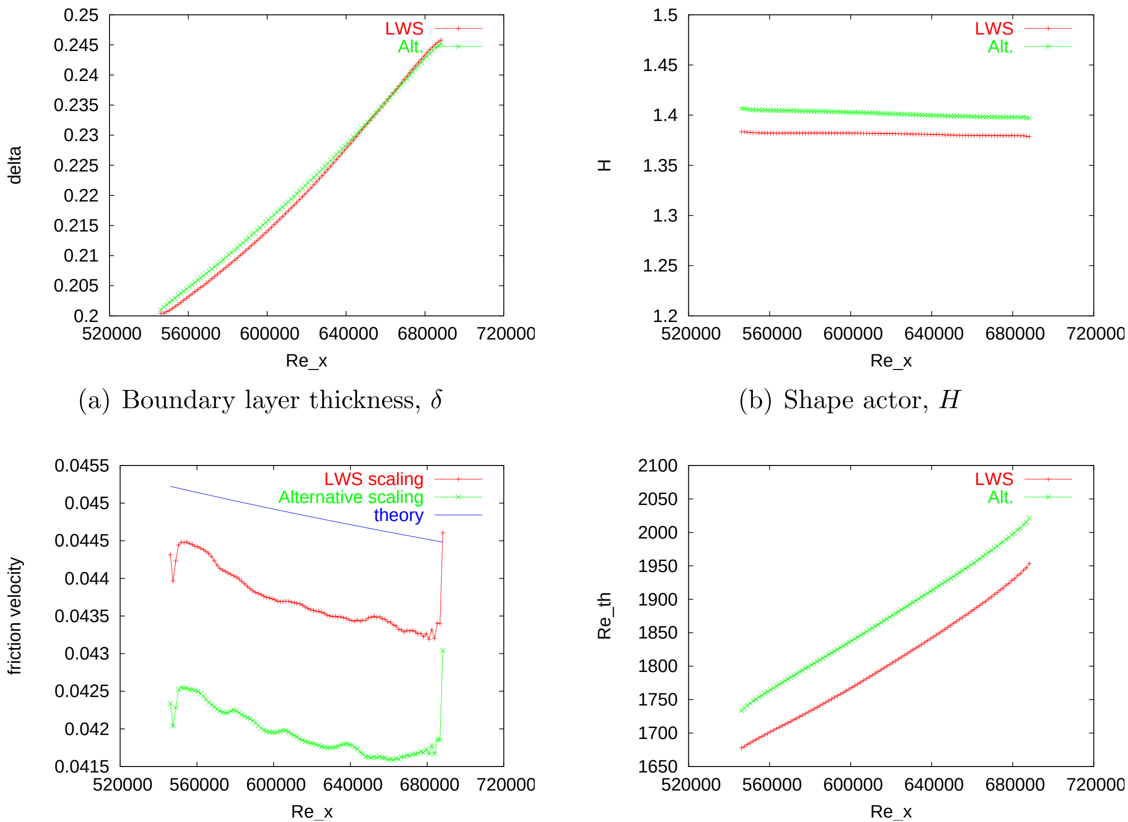

(a) Boundary layer thickness, δ

(b) Shape actor, H

(c) Friction velocity, u_τ

(d) Reynolds number, Re_θ

Figure 5.22: Comparison of δ, H, u_τ and Re_θ versus Re_x between LWS and alternative scalings

and outer (5.21(a)) variables for both meshes. On both figures, the velocity profile obtained on the tetrahedral mesh is over predicted in the outer region which comes from the fact that the friction velocity is underestimated using tetrahedral meshes. The tetrahedral mesh does not resolve completely the whole boundary layer as it is seen in Figure 5.21(b). For this example, the hexahedral mesh has better convergence than the tetrahedral mesh.

5.2.2.3 Solution with alternative scaling

In Figures 5.22 - 5.26, the results obtained by using the Lund, Wu and Squires scaling are compared to those obtained by using the alternative scaling in the rescaling recycling method. Figure 5.22(a) shows the boundary layer thickness as a function of the streamwise location. The boundary layer thickness varies quasi linearly

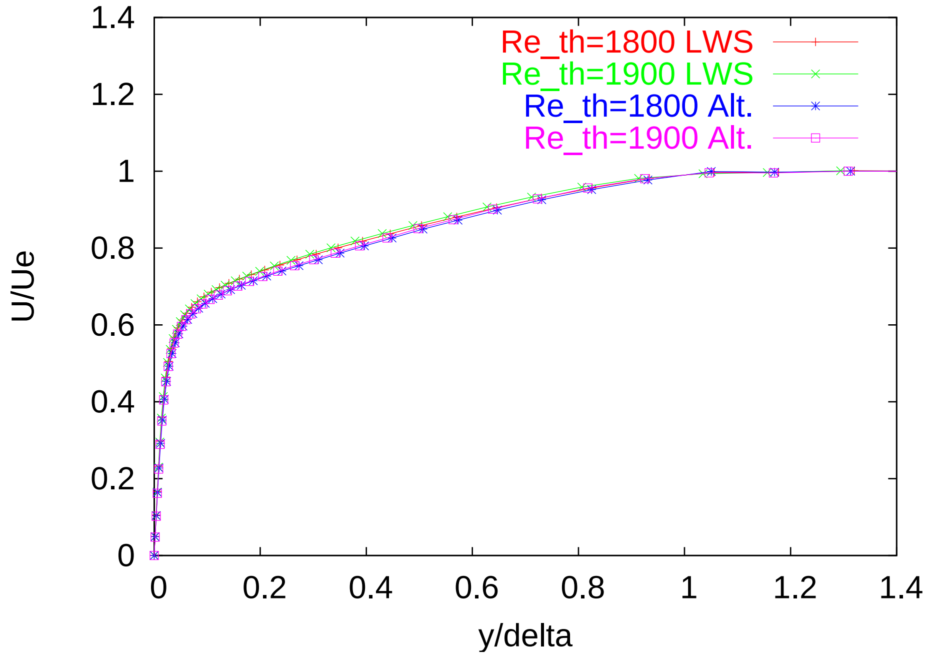

Figure 5.23: Comparison of mean streamwise flow profile ($\frac{U}{U_\infty}$ vs. η) obtained using LWS and alternative scalings at $Re_\theta = 1800$ and 1900

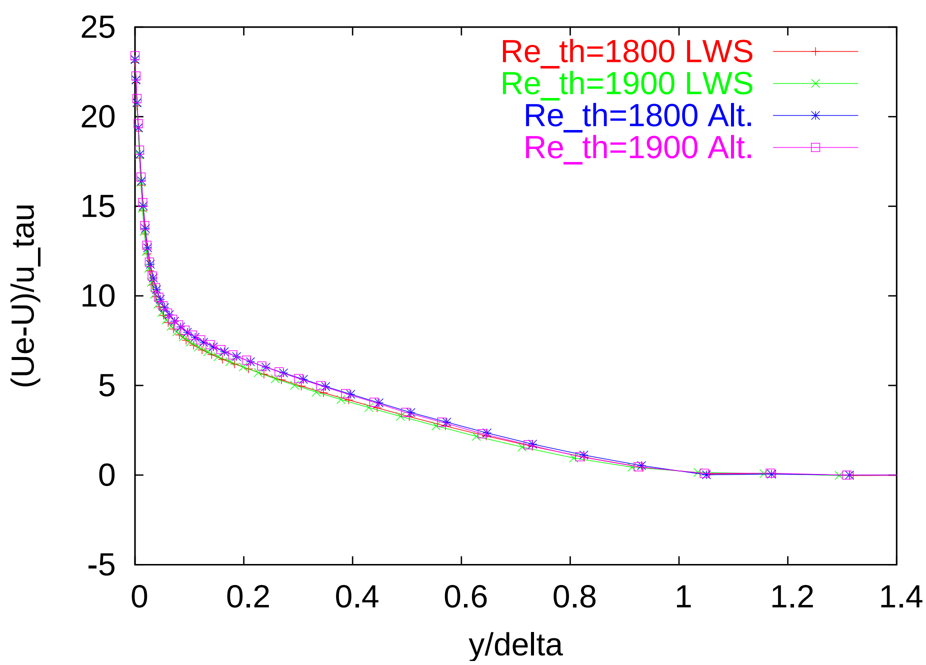

Figure 5.24: Comparison of mean streamwise flow profile ($\frac{U_\infty - U}{u_\tau}$ vs. η) obtained using LWS and alternative scalings at $Re_\theta = 1800$ and 1900

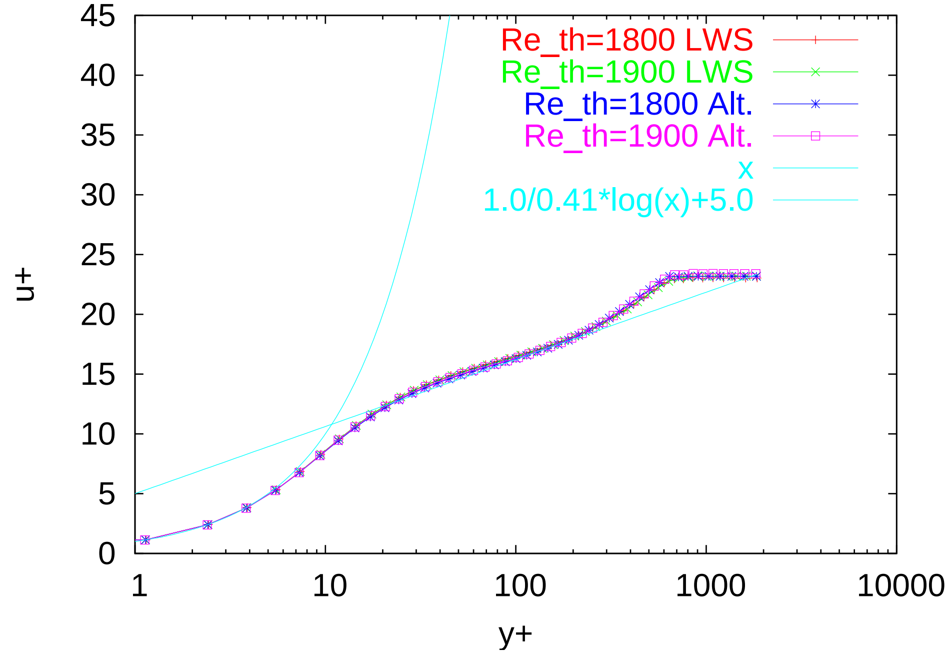

Figure 5.25: Comparison of mean streamwise flow profile in semi log scale (u^+ vs. y^+) obtained using LWS and alternative scalings at $Re_\theta = 1800$ and 1900

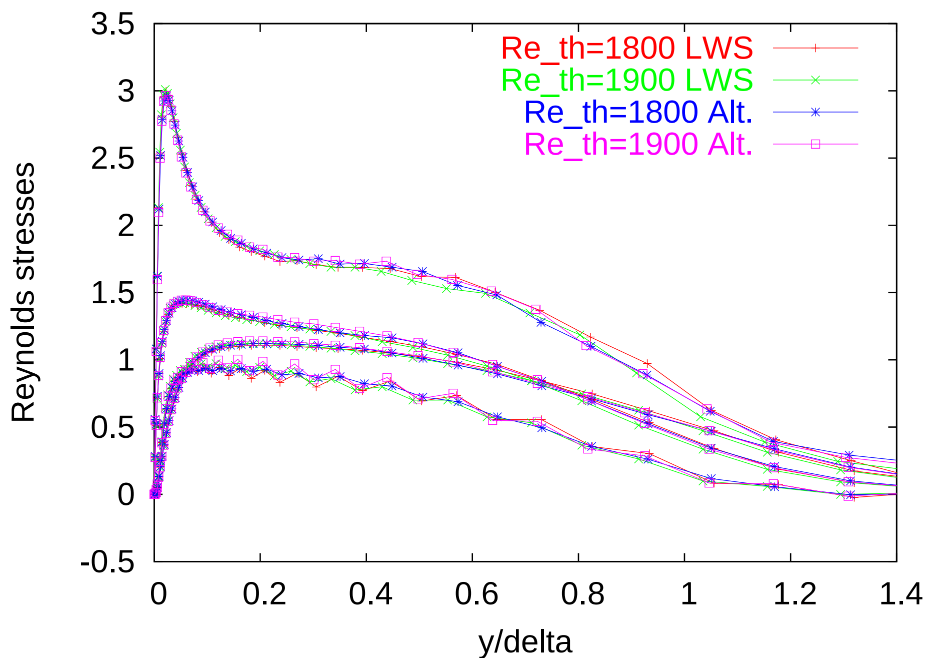

Figure 5.26: Comparison of Reynold stresses obtained using LWS and alternative scalings at $Re_\theta = 1800$ and 1900

in both cases. The boundary layer curves coincide together in the second part of the domain. The shape factor, $H = \frac{\delta^*}{\theta}$, is plotted on Figure 5.22(b) where δ^* and θ are the displacement and momentum thicknesses respectively. For both scalings, the shape factor is essentially constant and within 2% of each other. Figure 5.22(c) shows the friction velocity profiles. The friction velocity profile calculated using the LWS scaling is consistantly 4% higher than the profile using the alternative scaling. Both profiles have the same trend as the theorectical line (eq. 5.20) when the inflow and outflow regions are ignored. The Reynolds number based on momentum thickness is 3% higher in the case using the alternative scaling, than the LWS scaling, shown in Figure 5.22(d).

In Figures 5.23 - 5.26, the flow profiles are plotted for $Re_\theta = 1800$ and $Re_\theta = 1900$ for both scalings. Figures 5.23, 5.24 and 5.25 show the mean streamwise flow profile in the outer variable, velocity deficit normalized by the friction velocity and in the inner variable on the semi log scale, respectively. The profiles from the two simulations are essentially identical when normalized both by the free stream velocity (Fig. 5.23) and by the local friction velocity (Fig. 5.24 and 5.25). The Reynolds stresses shown in Figure 5.26 are $\frac{u_{rms}}{u_\tau}$, $\frac{w_{rms}}{u_\tau}$, $\frac{v_{rms}}{u_\tau}$ and $\frac{\overline{u'v'}}{u_\tau^2}$, from upper to lower curves respectively. The profiles of the different components of fluctuations collapse together for both simulations.

Even if the alternative scaling simulation gives small variations in the flow properties (e.g. boundary layer thickness, coefficient of friction) when comparing to those from the simulation using the LWS scaling, the mean and fluctuating flow profiles are statistically similar between the two scalings presented in this work. The transient part of the simulations in both scalings takes around same number of time steps.

5.2.3 Comparing to experimental data

In Figures 5.27 - 5.29, the solutions obtained at $Re_\theta = 1900$ for both LWS (LWS) and alternative scalings (alt) are compared to experimental data from Castillo and Johansson (CJ) [9] for turbulent boundary layer with zero pressure gradient at $Re_\theta = 1919$ and 2214, from Smits and Smith (SS) [50, 51] at $Re_\theta = 4981$ and from

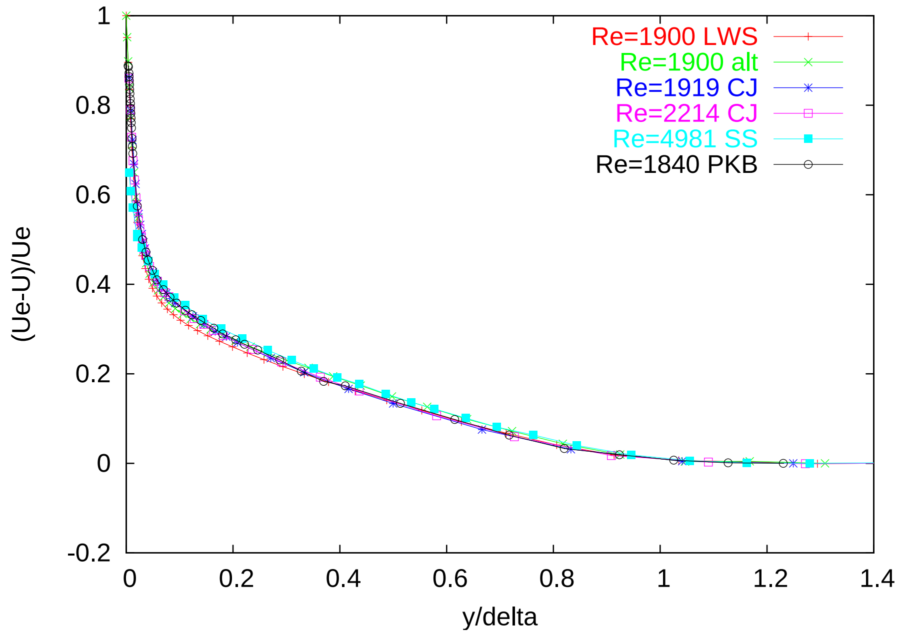

Figure 5.27: Comparing velocity profile in outer variables obtained using LWS and alternative scalings at $Re_\theta = 1900$ to experimental data by Castillo and Johansson [9] at $Re_\theta = 1919$ and 2214, of Smits and Smith [50, 51] at $Re_\theta = 4981$ and of Purtell, Klebanoff and Buckley [44] at $Re_\theta = 1840$

Purtell, Klebanoff and Buckley (PKB) [44] at $Re_\theta = 1840$. The mean streamwise velocity profiles are plotted on Figures 5.27 and 5.28. The data from PKB was not plotted on Figure 5.28 as the friction velocity was not provided. The velocity profiles obtained from the LES simulations using the rescaling recycling method collapse to the profiles obtained from all experimental data both in inner variables on semi log scale and in outer variables.

In Figure 5.29, the Reynolds stresses profiles normalized with the friction velocity are shown for LWS, alt, CJ and SS. Data from Castillo and Johansson did not have information about spanwise fluctuations, thus dark blue and pink curves for $\frac{w_{rms}}{u_\tau}$ are not present. The profiles using the rescaling recycling method are closest to the CJ data as those flows have similar Reynolds numbers based on momentum thickness. The peaks of $\frac{u_{rms}}{u_\tau}$ curves from the LES simulations coincide with peaks from CJ data. The $\frac{u_{rms}}{u_\tau}$ profiles obtained from LES are much wavier than those from experimental data. Indeed, in $0.1 < \eta < 0.4$ region the simulations

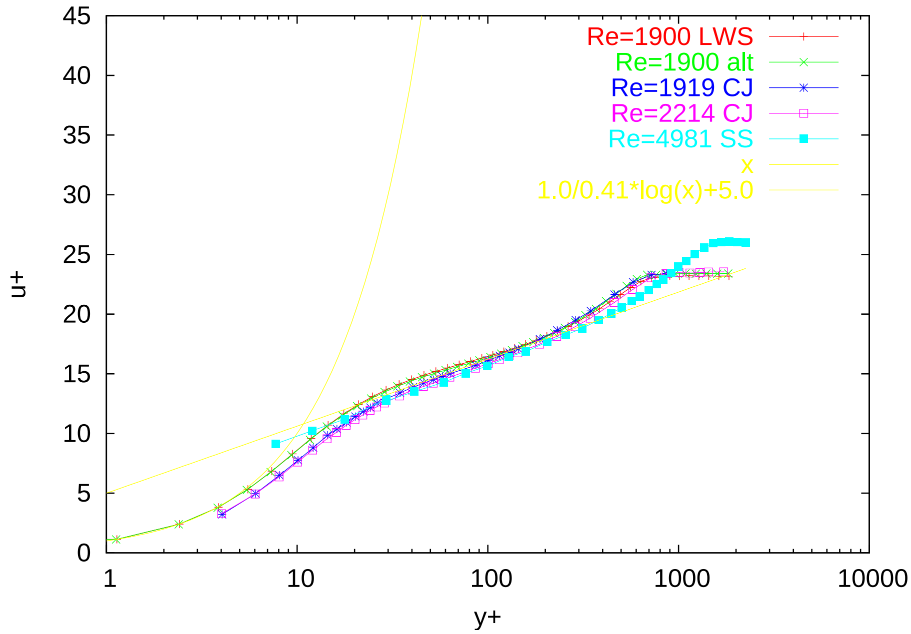

Figure 5.28: Comparing velocity profile in inner variables obtained using LWS and alternative scalings at $Re_\theta = 1900$ to experimental data by Castillo and Johansson [9] at $Re_\theta = 1919$ and 2214 and of Smits and Smith [50, 51] at $Re_\theta = 4981$

under predict u' fluctuations and over predict them in $0.4 < \eta < 1.0$ when compared to CJ data. Shear stress curves in the inner layer lay on top of each others for all data provided, but in the outer layer the LES over predict the shear stress. The largest discrepancies are in $\frac{v_{rms}}{u_\tau}$ where the profiles obtained from LES are between CJ and SS experimental data. The $\frac{w_{rms}}{u_\tau}$ curves from numerical data are slightly higher than that from SS data. The stresses obtained from SS data are much lower than those from CJ data mostly due to higher Re_θ.

Figure 5.30 presents the mean streamwise normalized velocity profile for the simulation using LWS scaling at $Re_\theta = 1900$ and the profiles obtained for Adrian and Tomkins [1, 2] DNS data of zero pressure gradient turbulent boundary layer at $Re_\theta = 1015$. The available DNS data are 50 time instances at 200 streamwise locations which were averaged in time. As 50 instances are not enough for time averaging, the scatter in the flow profiles is so high in this figure, but the general aspect of the flow profiles from this DNS data and from our LES simulation are the same.

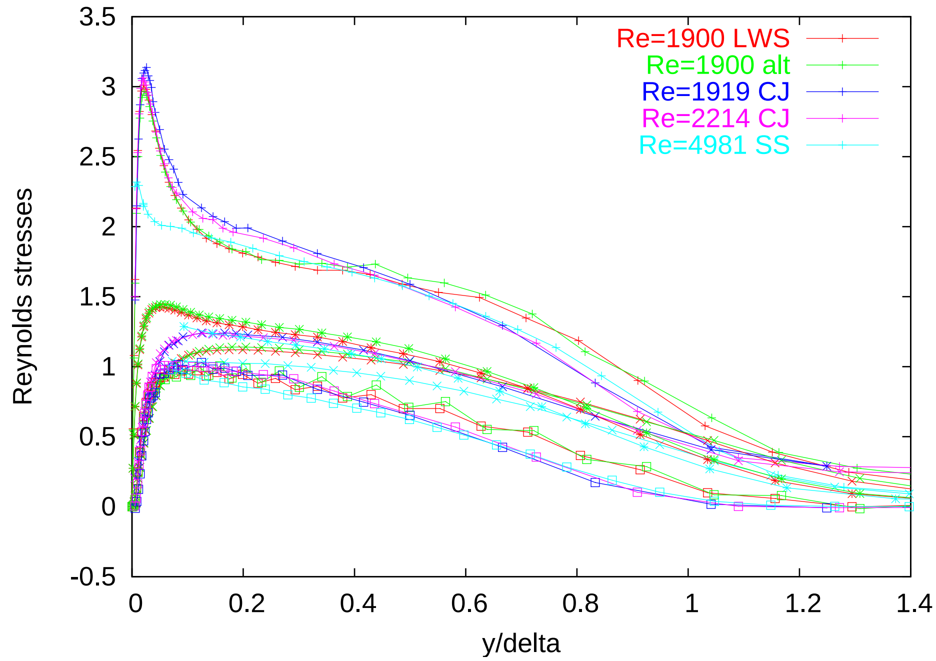

Figure 5.29: Comparing Reynolds stresses profiles obtained using LWS and alternative scalings at $Re_\theta = 1900$ to experimental data by Castillo and Johansson [9] at $Re_\theta = 1919$ and 2214 and of Smits and Smith [50, 51] at $Re_\theta = 4981$

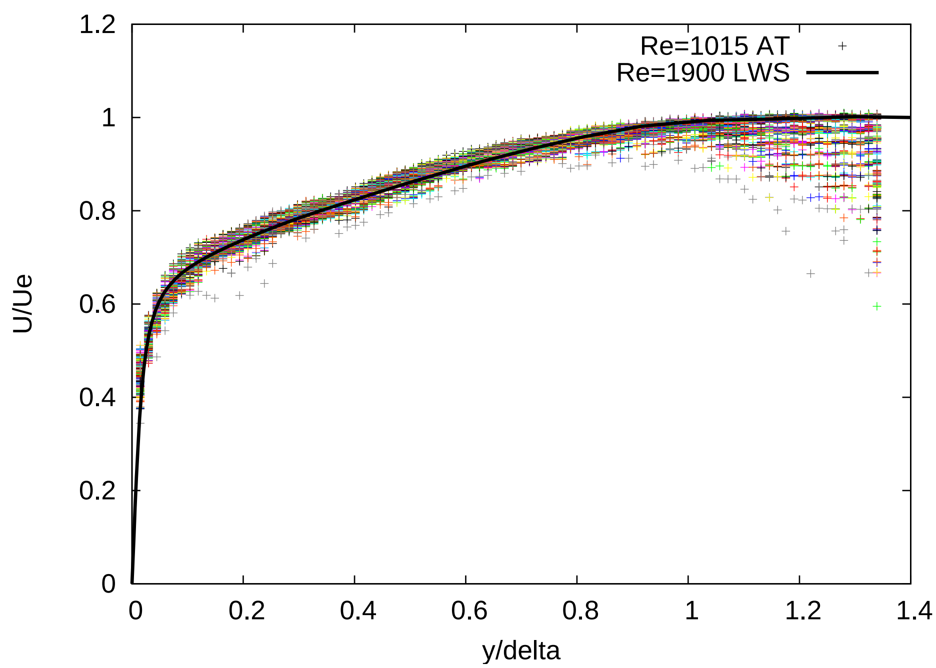

Figure 5.30: Comparing velocity profiles from LWS scaling at $Re_\theta = 1900$ and DNS data by Adrian and Tomkins [1, 2] at $Re_\theta = 1015$

In conclusion, the rescaling recycling method captures correctly the mean and fluctuating flow fields when simulating zero pressure gradient turbulent boundary layer.

CHAPTER 6
CONCLUSION

The rescaling recycling method presented in this work is based on the inflow generation technique developed by Lund, Wu and Squires (LWS) in [40]. In their work, first, an inflow generation simulation is used to develop statistically stationary zero pressure turbulent boundary layer by rescaling the solution from a downstream location and recycling it at the inlet boundary. Then, the mean and fluctuating profiles are extracted from inside the computational domain of this simulation and imposed as the boundary condition on the main simulation. Thus, two simulation are needed for this inflow generation technique. In the present research, the two simulations are merged together as the rescaling recycling method is used to vary the inlet boundary condition at each time step of the simulation of the turbulent boundary layer. In particular, the instantaneous solution from the recycle plane located inside the computational domain is averaged in time and homogeneous direction as the mean turbulent boundary layer flow is two-dimensional. Knowing the averaged field, the fluctuation field is determined. The two flow fields are then rescaled differently in the inner and outer boundary layer region using the appropriate self-similarity scales. The instantaneous flow field at the inlet boundary is then constructed from the recycled mean and fluctuating quantities obtained for the inner, viscous layer and the outer region.

The scaled plane extraction boundary condition is the implementation of the rescaling recycling method using the finite element framework to solve the turbulent boundary layer flows discretized on unstructured meshes. The Navier Stockes equations are solved for the flow variables using the Streamline Upwind Petrov Galerkin formulation. The recycle plane is virtual when the mesh is unstructured, thus the solution field needs first to be interpolated on the virtual 2D plane used for recycling.

Three scaling laws were implemented: the scaling based on Blasius equation was used for simulating flat plat laminar flow during the validation process; the scaling developed by LWS and the alternative scaling based on the turbulent boundary layer theory developed by George and Castillo [18] were both used to simulate turbulent boundary layer over a flat plate at zero pressure gradient. Both scalings give good results when compared to experimental data found in the literature.

For the alternative scaling law, the scales for the fluctuations were derived using the asymptotic invariance principle where the inner scaling was found to be the same as in the LWS scaling (i.e. the friction velocity). In the outer scaling, the only change from the LWS scaling is that the normal velocity and fluctuation scale with $U_\infty \frac{d\delta}{dx}$ instead of just the free stream velocity as the other components do. The alternative scaling incorporates the local Reynolds number dependence when calculating the ratio of the friction velocity between the recycle and inlet planes.

It was demonstrated that the rescaling recycling method gives promising results for turbulent boundary layers over flat plates. Testing needs to be expanded to axsysimmetric flows like pipes and nozzles as the SPEBC was implemented to work with curved domains. As the framework for easily implementing new scaling laws was also developed in this work, rewriting the scales into cylindrical coordinates could give better scales to use for axisymmetric domains. Extension of the scaling laws to be able to scale correctly pressure and temperature would permit the use of the rescaling recycling method for flows with favorable and adverse pressure gradients and even for compressible computational fluid dynamics.

It would be interesting to study if the upstream flow conditions incorporated in the scalings could reduce the computation time of simulating the turbulent boundary layers and improve the simulations of complex turbulent flows.

BIBLIOGRAPHY

[1] R. J. Adrian, C. D. Meinhart, and C. D. Tomkins. Vortex organization in the outer region of the turbulent boundary layer. *Journal of Fluid Mechanics*, 422:1–53, 2000.

[2] R. J. Adrian and C. D. Tomkins. Wide field of view boundary layer images and data. `http://www.princeton.edu/~gasdyn/R.W._Smith's_Flow_Data/MAC_format_data/README_mac.html`.

[3] G.K. Batchelor. Energy decay and self-preserving correlation functions in isotropic turbulence. *Quart. Appl. Math.*, 6:197, 1948.

[4] P. Batten, U. Goldberg, and S. Chakravarthy. Interfacing statistical turbulence closures with large-eddy simulation. *AIAA Journal*, 42(3):485–492, 2004.

[5] H. Blasius. Laminare stromung in kanalen wechselnder breite. *Z. Math. Physik*, 1910.

[6] A. N. Brooks and T. J. R. Hughes. Streamline upwind / Petrov-Galerkin formulations for convection dominated flows with particular emphasis on the incompressible Navier-Stokes equations. *Comp. Meth. Appl. Mech. Engng.*, 32:199–259, 1982.

[7] L. Castillo. Upstream conditions and their effect on the scaling of turbulent boundary layer. In *38th AIAA Ann. Mtg.*, Reno, NV, Jan. 2000.

[8] L. Castillo and W. K. George. Boundary layers with pressure gradient: Similarity of the velocity deficit region. In *38th AIAA Ann. Mtg.*, Reno. NV, Jan. 2000.

[9] L. Castillo and G. Johansson. The effects of upstream conditions in a low reynolds number turbulent boundary layer with zero pressure gradient. *Journal of Turbulence*, 3, 2002.

[10] L. Castillo, J. Seo, H. Hangan, and G.T. Johansson. Experimental investigation of the initial conditions in turbulent boundary layer at high reynolds number. In *40th AIAA Ann. Mtg.*, Reno, NV, Jan. 2002.

[11] D. E. Coles. The law of the wake in a turbulent boundary layer. *Journal of Fluid Mechanics*, 1:191, 1956.

[12] D.R. Dowling and P.E. Dimotakis. Similarity of the concentration field of gas-phase turbulent jets. *Journal of Fluid Mechanics*, 218:109–141, 1990.

[13] P. Druault, S. Lardeau, J.-P. Bonnet, F. Coiffet, J. Delville, E. Lamballais, J.F. Largeau, and L. Perret. Generation of three-dimensional turbulent inlet conditions for large-eddy simulation. *AIAA Journal*, 42(3):447–456, 2004.

[14] L. P. Franca and S. Frey. Stabilized finite element methods: II. The incompressible Navier-Stokes equations. *Comp. Meth. Appl. Mech. Engng.*, 99:209–233, 1992.

[15] W. K. George and L. Castillo. *Near Wall Turbulence Flows*, chapter Similarity Analysis of Turbulent Boundary Layers with Pressure Gradient: Another Look at the Equilibrium Boundary layer., pages 901–910. R.M.C. So et al. Editors, Elsevier, NY, 1993.

[16] W.K. George. The self-preservation of turbulent flows and its initial conditions and coherent structures. *Advances in Turbulence*, 1989.

[17] W.K. George. Some new ideas for similarity of turbulent shear flows. *Turbulence, Heat and Mass Transfer*, pages 39–73, 1995.

[18] W.K. George and L. Castillo. Zero-pressure gradient turbulent boundary layer. *Applied Mechanics Reviews*, 50(12), Dec. 1997. part1.

[19] W.K. George, P. Knecht, and L. Castillo. Zero-pressure gradient boundary layer revisited. In X.B. Reed, editor, *13th Symposium on Turbulence*, Rolla. MO, 1992.

[20] M. Germano, U. Piomelli, P. Moin, and W. H. Cabot. A dynamic subgrid–scale eddy viscosity model. *Physics of Fluids*, 3:1760, 1991.

[21] F.C. Gouldin, R.W. Schefer, S.C. Johnson, and W. Kollmann. Nonreacting turbulent mixing flows. *Prog. Energy Combust. Sci.*, 12:257–303, 1986.

[22] E. Gutmark and C.M. Ho. Preferred modes and the spreading rates of jets. *Physics of Fluids*, 26:2932–2938, 1983.

[23] G. Hauke. *A unified approach to compressible and incompressible flows and a new entropy-consistent formulation of the k-ϵ model*. PhD thesis, Stanford University, 1995.

[24] G. Hauke and T. J. R. Hughes. A unified approach to compressible and incompressible flows. *Comp. Meth. Appl. Mech. Engng.*, 113:389–396, 1994.

[25] G. Hauke and T. J. R. Hughes. A comparative study of different sets of variables for solving compressible and incompressible flows. *Comp. Meth. Appl. Mech. Engng.*, 153:1–44, 1998.

[26] T. J. R. Hughes. *The finite element method: Linear static and dynamic finite element analysis*. Prentice Hall, Englewood Cliffs, NJ, 1987.

[27] K. E. Jansen. A stabilized finite element method for computing turbulence. *Comp. Meth. Appl. Mech. Engng.*, 174:299–317, 1999.

[28] K. E. Jansen, C. H. Whiting, and G. M. Hulbert. A generalized-α method for integrating the filtered Navier-Stokes equations with a stabilized finite element method. *Comp. Meth. Appl. Mech. Engng.*, 190:305–319, 1999.

[29] K.E. Jansen. Large-eddy simulation using unstructured grids. In C. Liu and Z. Liu, editors, *Advances in DNS/LES*, pages 117–128, Columbus, Ohio, 1997. Greyden Press.

[30] K.E. Jansen, F. Shakib, and T.J.R. Hughes. Fast projection algorithm for unstructured meshes. In S.N. Atluri, editor, *Computational Nonlinear Mechanics in Aerospace Engineering*, number AIAA, Washington D.C., 1992.

[31] W.P. Jones and B.E. Launder. The prediction of laminarization with a two-equation model of turbulence. *International Journal of Heat and Mass Transfer*, 15:301–314, 1972.

[32] P.S. Klebanoff. Characteristics of turbulence in a boundary layer with zero pressure gradient. Technical Report 1247, NACA, 1955.

[33] H. Kong, H. Choi, and J. S. Lee. Direct numerical simulation of turbulent thermal boundary layers. *Physics of Fluids*, 12(10):2555–2568, 2000.

[34] H. Le, P. Moin, and J. Kim. Direct numerical simulation of turbulent flow over a backward-facing step. *Journal of Fluid Mechanics*, 330:349–374, 1997.

[35] S. Lee, S. K. Lele, and P. Moin. Simulation of spatially evolving turbulence and the applicability of taylor's hypothesis in compressible flow. *Physics of Fluids*, 4:1521, 1992.

[36] D. K. Lilly. A proposed modification of the Germano subgrid–scale closure. *Physics of Fluids*, 3:2746–2757, 1992.

[37] F.C. Lockwood and A. Moneib. Fluctuating temperature measurments in a heated round free jet. *Comust. Sci. Tech.*, 22:63–81, 1980.

[38] T. S. Lund. Large eddy simulation of a boundary layer with concave streamwise curvature. In *Annual Research Briefs*, page 91, NASA Ames / Stanford University, 1993. Center for Turbulence Research.

[39] T.S. Lund and P. Moin. Large eddy simulation of a concave wall boundary layer. *"Journal of Heat and Fluid Flow*, 17:290, 1996.

[40] T.S. Lund, X. Wu, and K.D. Squires. Generation of turbulent inflow data for spatially-developing boundary layer simulations. *J. Comp. Phys*, 140:233–258, 1998.

[41] J. Mi, D.S. Nobes, and G.J. Nathan. Influence of jet exit conditions on the passive scalar field of an axisymmetric free jet. *Journal of Fluid Mechanics*, 432:91–125, 2001.

[42] W.M. Pitts. Effect of global density ratio on the centerline mixing behavior of axisymmetric turbulent jets. *Exps. Fluids*, 11:125–134, 1991.

[43] L. Prandtl. *Collected Works*, volume 2, pages 620–626. Springer, 1961.

[44] L. P. Purtell, P. S. Klebanoff, and F. T. Buckley. Turbulent boundary layers at low reynolds numbers. *Phys. Fluids A*, 24:802, 1981.

[45] M. M. Rai and P. Moin. Direct numerical simulation of transition and turbulence in a spatially evolving boundary layer. *Journal of Computational Physics*, 109:169, 1993.

[46] C.D. Richards and W.M. Pitts. Global density effects on the self-preservation behaviour of turbulent free jets. *Journal of Fluid Mechanics*, 245:417–435, 1993.

[47] P. Sagaut, E. Garnier, E. Tromeur, L. Larchevêque, and E. Labourasse. Turbulent inflow conditions for large-eddy simulation of compressible wall-bounded flows. *AIAA Journal*, 42(3):469–477, 2004.

[48] F. Shakib. *Finite element analysis of the compressible Euler and Navier-Stokes equations*. PhD thesis, Stanford University, 1989.

[49] J. Smagorinsky. General circulation experiments with the primitive equations, I. The basic experiment. *Monthly Weather Review*, 91:99–152, 1963.

[50] R. W. Smith. *Effect of Reynolds Number on the Structure of Turbulent Boundary Layers*. Ph.D. Thesis, report 1984-t, Princeton University, 1994.

[51] R. W. Smith and A J Smits. Mean flow and turbulence data from the princeton university gasdynamics lab low-speed wind tunnel. `http://www.princeton.edu/~gasdyn/R.W._Smith's_Flow_Data/MAC_format_data/README_mac.html`.

[52] P. R. Spalart and S. R. Allmaras. A one-equation turbulence model for aerodynamic flows. In *AIAA Paper 92-439*, 1992.

[53] P.R. Spalart. Direct simulation of a turbulent boundary layer up to $Re_\theta = 1410$. *Journal of Fluid Mechanics*, 187:61–98, 1988.

[54] P.R. Spalart and A. Leonard. Direct numerical simulation of equilibrium turbulent boundary layers. In *Proc. 5th SYMP. ON TURBULENT SHEAR FLOWS*, Ithaca, NY, 1985.

[55] D. B. Spalding. A single formula for the law of the wall. *Journal of Applied Mechanics*, 28:455–57, 1961.

[56] S. Stolz and N.A. Adams. Large-eddy simulation of high-reynolds-number supersonic boundary layers using approximate deconvolution model and a rescaling and recycling technique. *Physics of Fluids*, 15(8):2398–2412, August 2003.

[57] M. Sussman, A. S. Almgren, J. B.Bell, L. H. Howell P. Colella, and M. L. Welcome. An adaptive level set approach for incompressible two-phase flows. *Journal of Computational Physics*, 148:81–124, 1999.

[58] C. A. Taylor, T. J. R. Hughes, and C. K. Zarins. Finite element modeling of blood flow in arteries. *Comp. Meth. Appl. Mech. Engng.*, 158:155–196, 1998.

[59] A. E. Tejada-Martinez. *Dynamic Subgrid-Scale Modeling for Large-Eddy Simulation of Turbulent Flows with a Stabilized Finite Element Method*. PhD thesis, Rensselaer Polytechnic Institute, 2002.

[60] A. E. Tejada-Martínez and K. E. Jansen. A dynamic smagorinsky model with dynamic determination of the filter width ratio. *fluids*, 16:2514–2528, 2004.

[61] A. E. Tejada-Martínez and K. E. Jansen. Spatial test filters for dynamic model large-eddy simulation with finite elements. *Commun. Numer. Meth. Engng.*, 19:205–213, 2004.

[62] H. Tennekes and J.L. Lumley. *A First Course in Turbulence*. The MIT Press, Cambridge, MA, 1972.

[63] A. A. Townsend. *The structure of turbulent shear flow*. Cambridge U. Press, 1976.

[64] F. White. *Viscous flow*. McGraw Hill, New York, 1974.

[65] C. H. Whiting and K. E. Jansen. A stabilized finite element method for the incompressible Navier-Stokes equations using a hierarchical basis. *International Journal of Numerical Methods in Fluids*, 35:93–116, 2001.

[66] David C. Wilcox. *Turbulence Modeling for CFD*. DCW Industries, La Canada, CA, 1998.

[67] I. Wygnanski, F. Champagne, and B. Marasli. On the large scale structures in two-dimensional, small-deficit, turbulent wakes. *Journal of Fluid Mechanics*, 168:31–71, 1986.